ResearchOnline@JCU

JAMES COOK UNIVERSITY AUSTRALIA

This file is part of the following work:

Humphreys, Mitchell (2020) ***Characteristics of wind-induced internal pressures in industrial buildings with wall openings.*** **PhD Thesis, James Cook University.**

Access to this file is available from:

Copyright © 2019 Mitchell Humphreys.

The author has certified to JCU that they have made a reasonable effort to gain permission and acknowledge the owners of any third party copyright material included in this document. If you believe that this is not the case, please email researchonline@jcu.edu.au

Characteristics of Wind-Induced Internal Pressures in Industrial Buildings with Wall Openings

Thesis submitted by

Mitchell Humphreys

in April 2020

For the degree of Doctor of Philosophy

in the College of Science and Engineering

James Cook University

STATEMENT ON THE CONTRIBUTION OF OTHERS

Supervision: Prof. J. D. Ginger and Dr. D. J. Henderson were the principal supervisors of this work.

Editorial Assistance: Principal editorial assistance was provided by Prof J. D. Ginger and Dr. D. J. Henderson. Additional editorial assistance was provided by Adjunct Prof. G. R. Walker.

Experimental Assistance: Assistance during air-leakage testing and wind-induced pressure testing was provided by Mr. Geeth Bodhinayake. Assistance during the experimental setup of the Industrial Building was provided by Mr Geeth Bodhinayake, Mr. Don Braddick, Mr. Denis Smith, Mr. Simon Ingham, and Dr. Korah Parackal.

Funding: Financial support from the Commonwealth of Australia through the Australian Post Graduate award, the Bushfire and Natural Hazards Cooperative Research Centre program, the Australian Research Council linkage grant (Project ID: LP150101206), and the project partners, Neil Creek and the Australasian Steel Institute Ltd, JDH Consulting, and Scott Woolcock Consulting Pty Ltd is gratefully acknowledged.

ACKNOWLEDGMENTS

I first and foremost wish to express my sincere thanks to my advisors Professor John Ginger and Dr. David Henderson; this work would not have been possible without their guidance, advice, and patience. I would especially like to acknowledge my primary advisor Professor John Ginger, his support and guidance cannot be overstated.

I would also like to thank Adjunct Professor George Walker. I am very grateful for the discussions we had and his time and effort providing feedback reviewing my thesis. Further, I would also like to thank the projects partners John Holmes, Neil Creek, and Scott Woolcock, without their support this work would not have been possible.

I also wish to acknowledge the Cyclone Testing Station for their support of this project through the use of equipment and resources, as well as their staff Simon Ingham, Denis Smith, Don Braddick, and Lucy Crowley, for their technical support and comradery during my time with the Cyclone Testing Station. I would also like to acknowledge my colleague Geeth Bodhinayake for the many hours spent assisting me with a multitude of tasks.

Finally, I will thank my family and friends for their enduring support throughout this time.

ABSTRACT

Wind-induced internal pressure fluctuations in a building are dependent on external pressure fluctuations, and parameters such as the size and location of openings in the envelope, and volume of the building. Large openings in a building's envelope have the potential to generate large internal pressures during strong winds. Large internal pressures contribute to a significant portion of the combined wind loads on a structure. Application of accurate internal pressures enables the optimal structural design of industrial type buildings. Previous internal pressure studies have shown the quasi-static method used by wind loading standards to determine design internal pressures may lead to non-optimal designs as it fails to incorporate parameters that amplify or attenuate peak internal pressures. This thesis investigates the influence of these parameters on the internal pressures in industrial type buildings.

These parameters were examined with two separate full-scale experiments that analysed natural wind-induced internal pressures in (i) a controlled Full-Scale Test Enclosure with a range of single windward wall openings (ii) a typical Industrial Building, examined nominally sealed and with large windward wall openings. Further, a series of air-leakage tests were conducted on the Industrial Building to quantify the area and distribution of background leakage and the flexibility of the envelope.

The background leakage in the nominally sealed Industrial Building equals about 1% of the total wall area, greater than most other building types and most buildings in temperate climates. These porous building openings significantly attenuate internal pressure fluctuations induced from a single large wall opening. The flexibility of the Industrial Buildings envelope further attenuates the internal pressure response and is equivalent to increasing the standard building volume by three times (i.e. $V = 4V_B$).

The full-scale internal pressure studies show the continuity equation satisfactorily estimates the mean internal pressure in a nominally sealed building, with and without large openings, when the mean external pressure and the open area distribution is accurately defined. The internal pressure fluctuations in the nominally sealed Industrial Building are small compared to external pressure fluctuations, and are attenuated above the characteristic frequency f_c of about 0.3 Hz.

The Helmholtz resonator model describes internal pressure fluctuations in a building with a single windward wall opening. Helmholtz resonance (i.e. amplification of internal pressures at Helmholtz frequency) is observed in both the controlled Full-Scale Test Enclosure and Industrial Building with large windward wall openings, which matches an inertial coefficient C_I of between 1.2 and 1.5, similar to previous model scale studies.

The controlled Full-Scale Test Enclosure shows the internal pressure response (i.e. amplification and attenuation of peak and fluctuating internal pressures) from a single windward wall opening is a function of the non-dimensional opening area to building volume parameter $S^* = (A^{3/2}/V)(a_s/\bar{U}_h)^2$. The peak and standard deviation internal pressures are amplified for $S^* \geq 1.9$, and attenuated for $S^* \leq 0.75$, between 5 to 10% relative to the quasi-static approximation, and that the quasi-static approximation is appropriate (i.e. peak internal pressures equal peak external pressure) for $S^* \cong 0.9$.

Simulation of the internal pressure response for a single windward wall opening shows that when S* is greater than 0.9, the amplitude of Helmholtz resonance is highly dependent on the viscous losses, characterised by the loss coefficient C_L. This study demonstrates that viscous losses increase (C_L increases from 10 to 20) as S* increases from 0.9 to 5.8 due to the reduction of the mean flow velocity through the opening as S* increases.

The internal pressure fluctuations induced in the Industrial Building from a large windward opening are significantly attenuated by the background leakage. It is shown that Helmholtz resonance is significantly damped and peak internal pressures response is between 3 to 12% less than the quasi-static approximation for large S* values, 390 and 24 respectively. The results show the quasi-static approximation used by wind loading standards to predict peak internal pressures in industrial buildings may be conservative if the background leakage is not considered, and is dependent on the non-dimensional opening area to building volume parameter S*.

The results and conclusions of this study are useful for developing guidelines on estimating design internal pressures in industrial buildings, and provides information for revising internal pressure provisions in wind loading standards.

CONTENTS

LIST OF FIGURES

LIST OF TABLES

NOMENCLATURE AND SYMBOLS

A	Area of single opening (m^2)
A_L	Combined leeward opening area (m^2)
A_o	Combined porous opening area (m^2)
A_P	Porous opening area (m^2)
A_T	Total surface area (m^2)
a_s	Speed of sound through air (340 m/s)
C	Empirical flow coefficient
C_I	Inertial coefficient
C_L	Loss coefficient of single opening
C_L'	Loss coefficient of porous openings
f	Frequency (Hz)
f_c	Characteristic frequency (Hz)
f_H	Helmholtz frequency (Hz)
g	Acceleration due to gravity (9.81 m/s^2)
h	Buildings mid-roof-height (m)
K_B	Bulk modulus of a building
K_A	Bulk modulus of air
k	Discharge coefficient of single opening
k_P	Discharge coefficient of porous openings
l_e	Effective length of 'air-slug' (m)
M_r	Inertia ratio or volume ratio (Al_e/V)
n	Empirical flow exponent
p	Pressure (Pa, N/m^2)
Q	Volumetric flow rate (m^3/s)
r	Model-scale to full-scale ratio
S^*	Opening area to volume parameter $(\Phi_1\Phi_2^2)$
S_u	Longitudinal wind velocity power spectral density ($m^2/(s^2 \cdot Hz)$)
S_p	Pressure power spectral density (Pa^2/Hz)
t	Time (s)
t^*	Non-dimensional time $(t\overline{U}_h/\lambda_u)$

U	Wind velocity (m/s)
U_0	Spatially averaged velocity though an opening (m/s)
U_z	Wind velocity at reference height z from the ground surface (m/s)
$\overline{U}$	Temporally averaged wind velocity (m/s)
$\overline{U}_h$	Temporally averaged wind velocity at the mid-roof-height (m/s)
V	Enclosed Volume (m^3)

GREEK LETTERS

γ	Ratio of Specific heats of air $(= 1.4)$
α	Deflected shape factor ≅ 0.6
δ	Deflection
ε	Porosity, porous opening area relative to total surface area (%) (A_P/A_T)
θ	Approach wind angle (degrees)
μ	Absolute viscosity of air (Pa· s)
ρ	Density of air (kg/m^3)
λ_u	Integral length-scale of turbulence (m)
Φ_1	Opening area to Volume ratio $\left(A^{3/2}/V\right)$
Φ_2	Inverse of Mach number $(a_s/\overline{U}_h)$
Φ_3	Reynolds number $\left(\rho\overline{U}_h\sqrt{A}/\mu\right)$
Φ_4	Turbulence intensity $(\sigma_u/\overline{U})$
Φ_5	Mean gust length relative to opening size parameter $\left(\lambda_u/\sqrt{A}\right)$
Φ_6	Background leakage area to Large opening area ratio (A_P/A)
φ_5	Non-dimensional length parameter (λ_u/l_e)
τ_H	Non-dimensional time (tf_H)

SUB-SCRIPTS AND SUPER-SCRIPTS

e	External
$full$	Full-scale variable
h	Mid-roof-height
i	Internal
L	Leeward (surface with negative external pressure)
$model$	Model-scale variable
P	Porous
r	Model-scale dimension relative to full-scale-dimension
W	Windward (external surface with positive external pressure)
z	Reference height (m)

CHAPTER 1: INTRODUCTION

Buildings are designed to resist the forces nature applies to them during their lifetime, including those induced by windstorms. The failure of an inadequately designed building may lead to economic loss and human suffering. However, a design with excessive safety margins may lead to wastage of valuable resources, and construction materials. The optimal building design for windstorms requires a sound assessment of the wind loads and probability of occurrence during the building's lifetime. The internal pressure during a windstorm can contribute to a significant portion of the total wind load on a building, thus improvement of the assessment of internal pressure for structural design application will enable the optimal design of buildings.

Net wind loads on buildings are determined from the combination of external and internal pressures across the envelope. The internal pressure fluctuations are due to airflow in or out of the building volume via openings in the envelope (i.e. flow paths). Figure 1.1 and Figure 1.2 show a temporally averaged external pressure distribution along the centre line of a low-rise building, showing the mean internal pressure in a nominally sealed building, and mean internal pressure with an opening on the windward and leeward wall respectively.

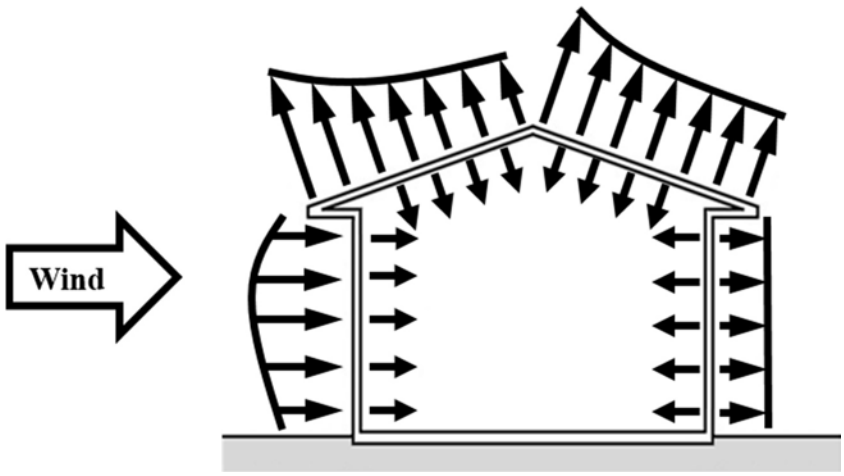

Figure 1.1. Mean external and internal pressure distribution for a nominally sealed building

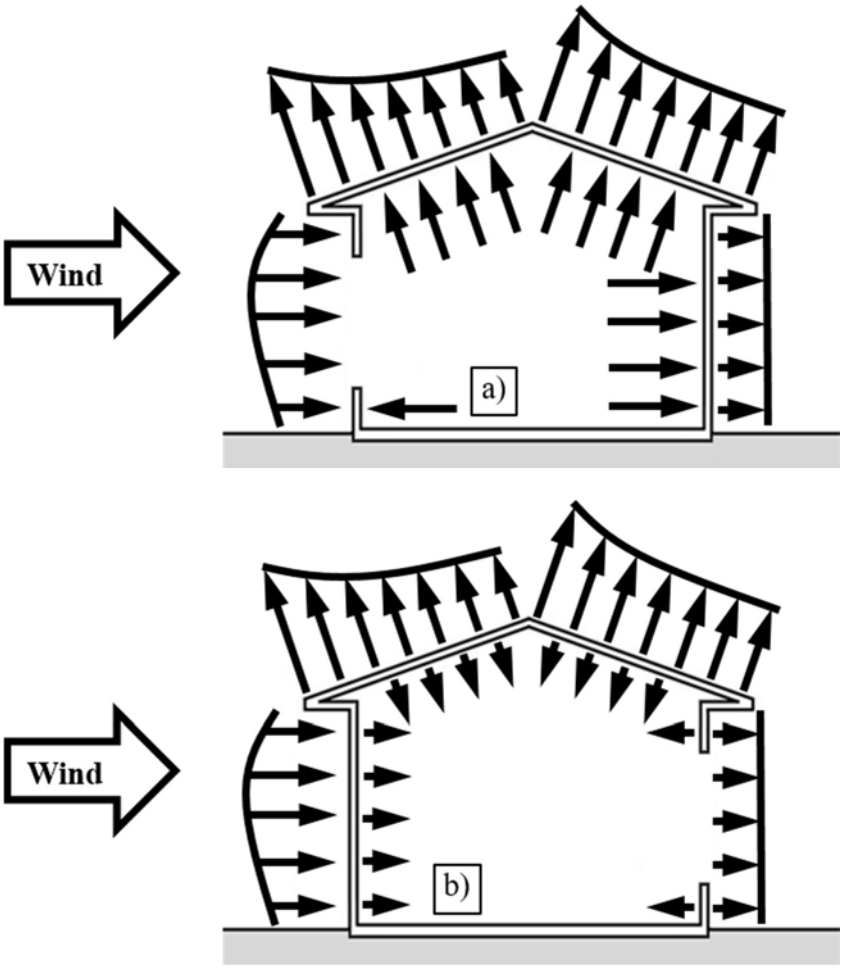

Figure 1.2. Mean external and internal pressure distribution with; a) Windward wall opening b) Leeward wall opening

Nominally sealed buildings inherently have various small openings scatted around the envelope, (e.g. gaps around fitments in walls (doors, windows), intersections in the envelope (ridgeline, roof/wall), etc.), generating small internal pressures, which contribute to a small fraction of the net pressure. Damage to a window or door in the envelope generates a much larger opening; enabling greater airflow to pass in and out of the volume, generating larger internal pressures, which contribute to a substantial portion of the net pressure across the envelope.

Damage investigations of structures after severe windstorms by Walker (1975), Sparks *et al.* (1994), Shanmugasundaram *et al.* (2000), Stehle and Henderson (2001), Boughton and Flack (2008), Morrison et al. (2014), Yang *et al.* (2018) and others, identify that the formation of a large opening promotes internal pressurization, frequently contributing to structural failure. For example, Figure 1.3 shows an industrial type building (i.e. engineered structure) with loss of cladding, buckled purlins and failure of the portal frame knee haunch following internal pressurization due to a failure of the windward roller door (held in place by a stack of pallets in Figure 1.3), documented by Stehle and Henderson (2001).

Figure 1.3. Windward roller door failure, generating large positive internal pressures contributing to structural failure - Stehle and Henderson (2001)

The derivation of peak internal and external pressures provided in structural design wind loading standards, (i.e. Australian and New Zealand – Design loads for wind action AS/NZS 1170.2 (2011), American Society of Civil Engineers – Minimum design loads for buildings and other structures ASCE 7-10 (2011)), are based on simple quasi-steady analysis. However, several factors influence internal pressures, which are not considered in the quasi-steady approach.

Most wind loading studies have focused on the external surface pressure characteristics which have been examined in detail since the 1960's, i.e. Jensen and Franck (1963). However, the pressure inside buildings has been subjected to far less scrutiny. Detailed internal pressure research conducted in the 1970's and 1980's by Liu (1975), Holmes (1979), Stathopoulos *et al*. (1979), Liu and Rhee (1986), and Vickery (1986) illustrate wind-induced internal pressure fluctuations depend on several factors:

- The time-varying external pressure distribution applied to all openings in the envelope;
- Types of envelope openings, dimensions, and locations;
- Building volume and compartmentalization within the building;
- Building envelope stiffness (i.e. buildings bulk modulus) ;
- Approach wind characteristics (i.e. velocity, turbulence) ;
- Approach wind angle relative to building openings.

Most wind-induced internal pressure studies since the 1970's have been a combination of model-scale wind tunnel experiments, theoretical analysis, and Computational Fluid Dynamic (CFD) models. A small number of full-scale studies have been conducted by Fahrtash and Liu (1990), Ginger *et al.* (1997), Kwok and Hitchcock (2009) and Guha *et al.* (2013a). Thus, validation of theoretical and computational methods is generally reliant on wind tunnel experiments and have rarely been examined with full-scale measurements. This thesis focusses on unique full-scale internal pressure experiments, where internal pressures are measured in a controlled Full-Scale Test Enclosure (FSTE) with a single opening and a full-scale industrial type building for a range of opening configurations. The full-scale data will be used as a means to validate model-scale results and theoretical methods.

Industrial type buildings are the focus of this thesis as they contribute to a significant proportion of the building stock in Australia, and have characteristics that may enable design optimisation based on the assessment of internal pressures. A steel-clad cold-form portal-frame industrial building is used as the full-scale test building. The focus of this thesis is on positive internal pressures (in a building with a large windward wall opening) and internal pressures in nominally sealed buildings.

Holmes (1979) showed that the internal pressure response in a building with a single opening is similar to that of a Helmholtz resonator where amplification of internal pressure fluctuations occurred at the Helmholtz frequency f_H in a model-scale building in an experimental wind tunnel study. Further wind tunnel and computational studies have identified a range of factors that influence the internal pressure, showing that damping due to viscous and frictional losses and amplification at Helmholtz frequency can produce significantly different design pressures than expected from the quasi-static method.

The quasi-static method used for the design internal pressures in wind loading standards, relies on the designer to define the area of openings on windward surfaces (exposed to positive external pressures) and leeward surfaces (exposed to negative external pressures, i.e. side-walls, leeward walls, roof) during a windstorm that produce the most adverse net wind loads for structural design. The designer's estimation of the windward and leeward opening areas carries a level of uncertainty that may lead to a range of internal pressures that can potentially produce conservative or unsatisfactory structural design loads. Industrial type buildings typically have numerous large access doors and a higher level of porosity compared to other building types; inevitably increasing the level of uncertainty when calculating windward and leeward opening area ratios and subsequent design internal pressures. This thesis provided information on the background leakage area in the nominally sealed full-scale building, improving the estimation of internal pressures.

The influence of background leakage (i.e. gaps around windows, doors, and discontinuities, etc.) in the presence of a larger opening have been examined in previous model-scale wind-tunnel studies. However, as model-scale studies are typically carried out at length-scales $L_r \cong 1/100$ and velocity-scales $U_r \cong 1/3$; this generally produces Reynolds numbers Re, that are $\times 10^2$ times less than full-scale. At model-scale, the *Re* of flow through porous openings inevitably produces inaccuracies in the internal pressure fluctuations. Many model-scale studies suggest that internal pressure fluctuations are greater than the quasi-static assessment, and low levels of envelope porosity have a negligible influence on these fluctuations (i.e. Stathopoulos *et al.* (1979), Vickery and Bloxham (1992), Womble *et al.* (1995), Pearce and Sykes (1999), Oh *et al.* (2007)). The internal pressure characteristics from the typical industrial type building

experiment provides data for assessing of the effect that envelope porosity (and flexibility) has on internal pressure fluctuations.

Recent model-scale studies have shown that ill-defined parameters (loss and inertial coefficients C_L and C_I) used in the theoretical analysis of internal pressures have a large variation depending on the model building conditions (Holmes and Ginger (2012), Xu et al. (2017)) . Application of the range of values to theoretical analysis produces significant variation in the derived internal pressure response.

1.1. Objectives:

Need for this research? The quasi-static method used to define internal pressures fails to incorporate parameters that amplify or attenuate internal pressure fluctuations. Investigation of these parameters is needed in a full-scale environment to compare with findings from model-scale studies and the consequence of this on the analytical and numerical methods used for the assessment of internal pressures. Further, uncertainties regarding the distribution of background leakage in buildings increases inaccuracies in internal pressure design, investigation of porous building openings is needed to clarify these distributions.

Accomplished by? 1) Examining the influence of parameters on internal pressure fluctuations from a unique Full-Scale Test Enclosure (FSTE). 2) Measuring internal and external pressures from a full-scale industrial building, to provide experimental data for assessment of analytical and numerical methods and comparison with model-scale wind-tunnel results. 3) Conducting air-leakage tests on a full-scale industrial building to quantify the area and distribution of background leakage.

Contributes to? Improved numerical methods that describe internal pressure fluctuations in full-scale buildings. Validated internal pressure data for design of all buildings, and improved calculation of the opening area distributions. Results will be particularly applicable to industrial type buildings.

The objectives of this study are to:

1. Measure internal pressures in an idealized Full-Scale Test Enclosure (FSTE) generated by from atmospheric wind-induced external pressures on a single windward wall opening. Analyse the response of the internal pressure fluctuations considering a range of parameters for comparison with model-scale and theoretical methods.

2. Define the background leakage in the envelope of a full-scale industrial building (JCU-ASIS) (i.e. gaps around windows, roller door, flashings, etc.). Characterise the flexibility of the JCU-ASIS envelope.

3. Measure wind-induced internal and external pressures on a full-scale Industrial Building (JCU-ASIS) from atmospheric wind-flow. Assess the influence of building envelope porosity, flexibility and other parameters on the internal pressures for comparison with other previous model-sale studies and full-scale studies.

It is hypothesised that the peak and fluctuating internal pressures induced in an industrial building from a large windward opening are significantly attenuated relative to the quasi-static approximation due to the damping from the background leakage in the envelope. It is also postulated that the for a single opening in a building, the viscous losses associated with the flow through the opening (i.e. loss coefficient) is a function of the area of the opening, volume of the building, and the approach wind speed, and that this relationship is implicitly a function of the Reynolds number *Re* of the flow through the opening and has a meaningful influence on internal pressure fluctuations.

1.2. Overview

Chapter 1 presents a broad overview of the importance of internal pressures to wind-induced net-pressures and structural design loads on buildings, the limitations in previous research, and research objectives for this thesis. Chapter 2 presents a detailed review of previous research regarding wind-induced internal pressures. It details the parameters that influence internal

pressure fluctuations, and the critical parameters that will be examined in this study. Chapter 2 also details numerical methods that will be utilised to assess the variables that influence internal pressure fluctuations.

Chapter 3 presents an internal pressure study on a Full-Scale Test Enclosure (FSTE) with a range of single windward wall openings subjected to atmospheric wind flow. The experimental setup, results, and analysis of the unique full-scale experiment is given. The analysis details ill-defined parameters that influence internal pressure fluctuations that have primarily been defined from model-scale wind-tunnel studies. The analysis also describes the response of the internal to external pressure concerning the area of the single opening in the envelope, the volume of the enclosure, and the approach wind speed, without influence of envelope porosity or flexibility.

Chapter 4 presents an internal pressure study conducted on a typical full-scale industrial type building (JCU-ASIS) subjected to atmospheric wind flow. Chapter 4 details the methodology and experimental setup for the wind-induced internal pressure study, and the study to determine the area of background leakage in the nominally sealed envelope, and the envelope flexibility, that are critical for analysing internal pressures. This is followed by detailing the wind-induced internal and external pressures for the building when nominally sealed, and with a range of large openings in the envelope. The influence of the envelope porosity and flexibility is determined and the assessment of internal pressures relative to these parameters are assessed and compared to theoretical analysis, and other previous model-scale and full-scale studies.

Chapter 5 presents the Conclusions and Recommendations of this thesis, providing suggestions for further work in this field.

CHAPTER 2: LITERATURE REVIEW

Irminger and Nokkentved (1936) were one of the first to analyse internal pressure measurements from a wind tunnel experiment in 1930. Irminger and Nokkentved (1936) derived equations to account for air passing in and out of multiple building openings. Consideration of internal pressure for structural wind loading was studied in the 1970's, by Liu (1975), Holmes (1979), and Stathopoulos *et al*. (1979), who showed that the internal pressure inside a building is dependent on several key parameters.

Vickery (1986), Liu and Rhee (1986), Vickery and Karakatsanis (1987), Harris (1990), Vickery and Bloxham (1992), Yeatts (1994), Womble et al. (1995), Sharma (1996), and others, conducted wind tunnel experiments and developed numerical methods to describe the internal pressure response relative to external pressure fluctuations. Limited full-scale experiments were also conducted in the 1990's by Fahrtash and Liu (1990) and Ginger *et al.* (1997), which validated some of these models. This Chapter details the current knowledge on wind-induced internal pressure fluctuations based on studies carried out at model-scale and full-scale, and other experimental studies. It also details the analytical and theoretical methods derived, and identifies critical research gaps that are addressed in this thesis.

2.1. Wind Loads on Buildings

The approach wind velocity $U(t)$ generates spatio-temporal varying external pressures on building surfaces $p_e(t)$, where pressures acting towards a surface are considered positive. Airflow through openings in the envelope induces pressure fluctuations inside the building $p_i(t)$. The spatio-temporal pressure difference across the envelope is defined as the net pressure $p_{net}(t) = p_e(t) - p_i(t)$. As the pressure fluctuations are induced by the wind velocity $U(t)$, the pressures are described as a coefficient relative to the mean dynamic pressure of the wind flow at a reference height, defined as a pressure coefficient $C_p(t) = p(t)/(½\rho\overline{U}_h)$. Here $\overline{U}_h$ is the temporally averaged wind speed (over about 10-minutes) taken at the mid-roof-height of the building h, and ρ is the density of air ($\cong$ 1.2 kg/m^3).

The wind velocity approaching the building at the mid-roof-height $U_h(t)$ is described as having mean and fluctuating components, $U_h(t) = \overline{U}_h + U'_h(t)$ respectively. The intensity of the velocity fluctuations with respect to the height z, is described by the turbulence intensity $I_{u,z} = \sigma_{u,z}/\overline{U}_z$, where $\sigma_{u,z}$ and $\overline{U}_z$ are the standard deviation of the velocity fluctuations and the time averaged longitudinal velocity at a height, z, above the ground surface, respectively. The energy of the velocity fluctuations is described in the frequency domain by the longitudinal wind velocity power spectral density (i.e. spectra) $S_u(f)$, where f is frequency (Hz).

Figure 2.1 illustrates a temporally averaged pressure distribution along the centre-line of a pitched roof low-rise building. Positive pressures are applied to windward surfaces and suction pressures are experienced in flow separation regions behind discontinuities in the envelope (i.e at windward roof/wall edges and ridgelines) and the wake of the building (i.e. leeward wall). A detailed summary of the fluid dynamics and external surface pressures is presented by Holmes (2007). The temporally varying pressures can also be described in the frequency domain by the pressure spectra $S_p(f)$. Area averaged pressures are temporal varying pressures averaged over bounded areas of interest.

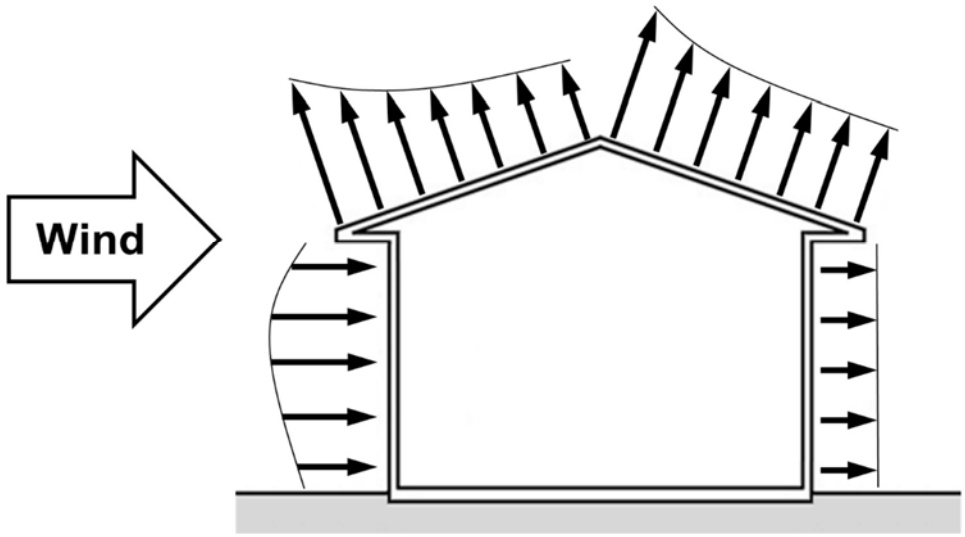

Figure 2.1. Generalized temporally averaged external pressure distribution along the centre of a pitched roof low-rise building

Changes to internal pressure are developed by airflow in and out of the building through openings in the envelope (i.e. flow paths). The porosity ε, of a nominally sealed building envelope, enables a small amount of air-flow through the envelope that results in small internal pressure fluctuations. Porosity is also defined as the permeability or inherent background leakage of the envelope of a structure. The magnitude of porosity $\varepsilon = A_P/A_T$, is the ratio of the sum of the area of porous opens A_P, to the total surface area A_T. Failure of a door or window in the envelope creates a much larger opening; enabling greater airflow to pass in and out of the building volume, generating larger internal pressure fluctuations. Envelope porosity reduces the influence of the larger openings on the internal pressure fluctuations. An opening is considered dominant when the internal pressure is similar to the external pressure applied to the opening; typically when an openings area A, is more than twice the sum of open areas on other surfaces, Cook (1986) (i. e. $A \geq 2A_P$). However, the air-flow in and out of building openings is complex, and has a significant influence on internal pressures fluctuations.

2.2. Flow Through an Opening

Temporally varying (unsteady), incompressible flow through an opening is described by Equation 2.1, known as the unsteady discharge equation. It reads left to right as the pressure loss across the opening $\Delta p(t)$, followed by the inertial and damping terms respectively. Here $U_0(t)$ is the spatially averaged velocity through the opening area A (i.e.$U_0(t) = Q(t)/A$), and $\partial U_0/\partial t$ is the acceleration through the opening. Here, C_I and C_L are inertial and loss coefficients respectively. Equation 2.1 is applicable for incompressible isentropic flow, however, it is considered acceptable for compressible flow for velocities less than $0.3a_s$, where a_s is the speed of sound ($a_s \approx 340\ m/s$) (White (2003)).

$$\Delta p(t) = \rho C_I \sqrt{A} \frac{\partial U_0}{\partial t} + \frac{C_L \rho \left(U_0(t)\right)^2}{2} \qquad 2.1$$

The loss and inertial coefficients C_L and C_I are important parameters which characterise the damping and inertia of the flow through the opening. Vickery (1991) showed that for limited situations C_L and C_I can be determined analytically. Where air flows through a sharp-edged circular orifice connecting two large volumes, potential flow theory gives a discharge coefficient $k = \pi/(\pi + 2) = 0.611$. The discharge coefficient k, is the ratio of actual flow to ideal flow and is equivalent to $1/\sqrt{C_L}$, therefore $C_L = 2.68$. The inertial coefficient C_I can also be derived for the same conditions using potential flow theory; $C_I = \sqrt{(\pi/4)} = 0.886$. These C_I and C_L values derived from potential flow theory may not apply to unsteady flow passing in and out of buildings, as discussed by Vickery (1991). Further details regarding C_L and C_I are provided in Section 2.9.2 and Section 2.9.3.

2.3. Temporally Averaged Flow Through Openings

Substitution of $\partial U_0/\partial t = 0$ and $\overline{U}_o = \bar{Q}/A_o$ into Equation 2.1 defines the temporal average flow rate through an opening in terms of a pressure coefficient $C_p = p/\left(\frac{1}{2}\rho\overline{U}_h{}^2\right)$, is given in Equation 2.2.

$$\bar{Q} = kA_o\sqrt{\frac{2\Delta\bar{p}}{\rho}} = kA_o\overline{U}_h\sqrt{\Delta\bar{C}_p} \qquad 2.2$$

Liu (1975) showed that Equation 2.2 can be combined with the continuity of air in and out of a building to describe the mean internal pressure by accounting for the envelope opening areas, discharge coefficients, and mean external pressure coefficients at all openings in the envelope. The mass continuity equation, given in Equation 2.3, describes the change of mass in a volume

$(V \cdot \partial\rho_i/\partial t)$, relative to the mass flow rate through N openings in the envelope, where ρ_i is the internal air density.

$$\sum_{j=1}^{N} Q_j \rho_i = V \frac{\partial \rho_i}{\partial t} \tag{2.3}$$

Substituting Equation 2.2 into Equation 2.3 for steady-state conditions, where $\partial\rho_i/\partial t = 0$, the flow-rate into a building equals the flow rate out, gives the mean internal pressure coefficient $\bar{C}_{p_i}$ in Equation 2.4 as a function of k_j, A_j, $\bar{C}_{p_e,j}$, which are the discharge coefficient, area and mean external pressure coefficient at opening *j*, respectively.

$$\sum_{j=1}^{N} \left(k_j A_j \sqrt{\left|\bar{C}_{p_e,j} - \bar{C}_{p_i}\right|} \cdot sign\left(\bar{C}_{p_e,j} - \bar{C}_{p_i}\right) \right) = 0 \tag{2.4}$$

Liu (1975) simplified Equation 2.4 by considering a uniformly porous building envelope where all discharge coefficients are equal and separated all openings into two groups, windward if subjected to positive external pressures and leeward if subjected to negative external pressures. The spatio-temporal average pressures across the two groups are defined as the mean windward ($\bar{C}_{p_eW}$) and mean leeward ($\bar{C}_{p_eL}$) pressure coefficients, and the sum of the openings on the windward and leeward surfaces are A_W and A_L respectively. Substituted $\bar{C}_{p_eW}$, $\bar{C}_{p_eL}$, A_W and A_L into Equation 2.4 defines a mean internal pressure Equation 2.5. Where $\bar{C}_{p_eW} \geq \bar{C}_{p_i} \geq \bar{C}_{p_eL}$ as a function of A_W/A_L and illustrated in Figure 2.2. Equation 2.5 is the basis for the quasi-steady internal pressure coefficients provided in wind loading codes and standards, such as

AS/NZS1170.2 (2011), where internal pressure coefficients are a function of A_W/A_L. Further details on the quasi-steady theory are in Section 2.9.4.

$$\bar{C}_{p_i} = \frac{\bar{C}_{p_eW}}{1+\left(\frac{A_L}{A_W}\right)^2} + \frac{\bar{C}_{p_eL}}{1+\left(\frac{A_W}{A_L}\right)^2} \qquad 2.5$$

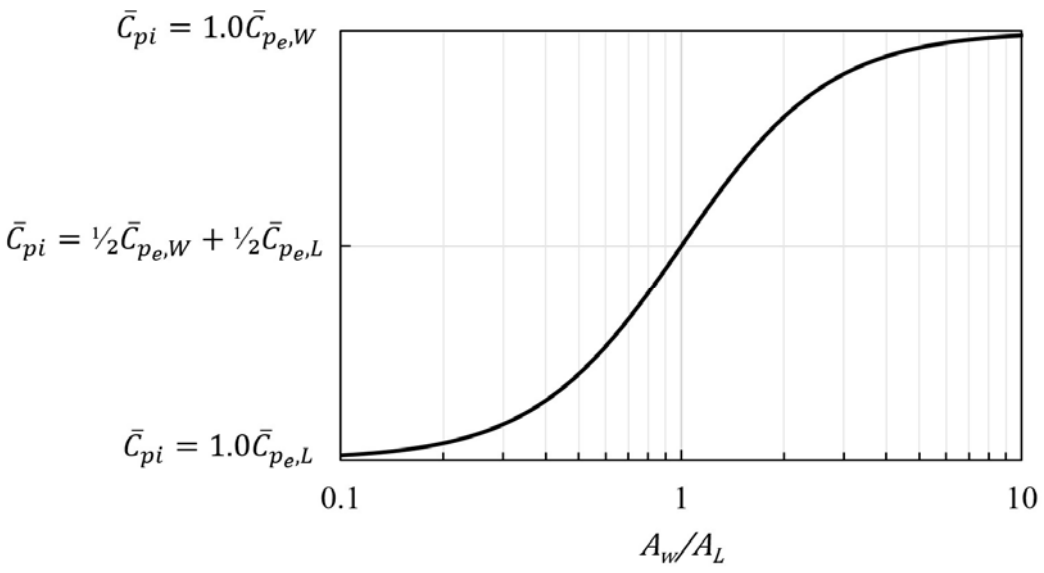

Figure 2.2. Mean internal pressure coefficient as a function of A_W/A_L – Equation 2.5

2.3.1. Temporally Averaged Flow Through Porous Openings

Temporally averaged flow through porous openings in a nominally sealed building envelope has been examined experimentally by Tamura and Shaw (1976) and others by pumping air into nominally sealed buildings which flows out through the porous openings in the envelope. This experiment typically uses a large fan and is known as an Air-Leakage test. The steady-state volumetric flow-rate pumped into the building $\bar{Q}$, and the uniform steady-state pressure induced

across the envelope $\Delta\bar{p}$ are measured at different intervals to characterize the flow through the envelope as a function of $\bar{Q}$ and $\Delta\bar{p}$. Tamura and Shaw (1976) showed that the relationship between $\bar{Q}$ and $\Delta\bar{p}$ is well defined by the Power-law given in Equation 2.6 where C is an empirical flow coefficient ($m^3/s/Pa^n$) that encompasses multiple parameters including the area of the flow paths, and miscellaneous losses; and n is an empirical flow-exponent (dimensionless) that characterises the relationship between flow and pressure. The Power-law model assumes that flow conditions through openings are similar to a pipe, where the flow-exponent ranges between Bernoulli's limits of ½ and 1 for turbulent to laminar pipe flow respectively.

$$\bar{Q} = C(\Delta\bar{p})^n \qquad 2.6$$

As both the Power-law (Equation 2.6) and unsteady discharge equation (Equation 2.2) describe the temporally averaged flow through openings, it can be shown that the flow coefficient C is equivalent to $C = kA_P(2/\rho)^n$ producing Equation 2.7. Here, A_P is the sum of all porous opening areas on the envelope. Equation 2.7 is used to define the area of porous openings from the empirical flow coefficients considering a steady discharge coefficient through the openings (k = 0.61).

$$\bar{Q} = kA_P\left(\frac{2}{\rho}\right)^n |\Delta\bar{p}|^n \qquad 2.7$$

Figure 2.3 shows a summary of the air-leakage tests on several supermarkets, schools, and high-rise buildings conducted by Shaw (1981), and Davenport and Surry (1984). They found the flow-exponent n fluctuated around 0.65. However, Urquhart and Richman (2015) detail that many air-leakage studies have shown that this value has significant variability depending on the

type of flow paths and can produce unrealistic values (n < 0.5) from contraction or expansion of small flow paths during testing.

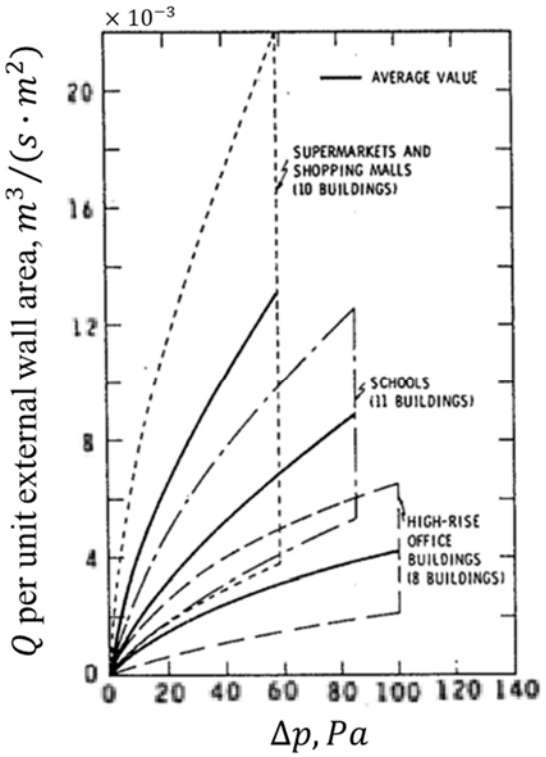

Figure 2.3. Comparison of air-leakage results from various building types - Shaw (1981)

Vickery (1986) defined an effective porous opening area A_P of buildings using air leakage data from Davenport and Surry (1984) by assigning an averaged value of C_L = 2.5 ($k \approx 0.6$) into Equation 2.2. Vickery (1986) then defined the porosity of buildings per unit wall area given in Table 2.1 and ranges from about 0.05% to 0.3%.

Table 2.1. Wall porosity of buildings from Vickery (1986) and Davenport and Surry (1984)

Building Type	Effective wall porosity ε (= A_P/A_T)
Super markets	0.0028 ± .0019
Schools	0.0015 ± .0006
High-rise building	0.0006 ± .0003

2.4. Sealed Building with a Single (Dominant) Opening

Holmes (1979) conducted an experimental model-scale wind tunnel study of internal pressures in a low-rise building with a single windward opening. He found that the flow into a building and the internal pressure response behaves similar to a damped Helmholtz resonator, a well-known acoustic model. The Helmholtz resonator model, given by Equation 2.8, describes the motion of air in and out of a volume due to external pressure fluctuations at a single opening; illustrated in Figure 2.4. The model describes the air moving as a single body (i.e. 'air-slug'), with a displacement $x(t)$, where $\dot{x}$ and $\ddot{x}$ are the velocity and acceleration of the air-slug respectively. Equation 2.8 reads left to right as the inertial, damping, resistance, and driving terms, where A_o, V, a_s and $p_e(t)$ are the opening area, building volume, speed of sound ≈ 340m/s, and spatially-averaged external pressure applied to the opening, respectively. The effective length of the air-slug, $l_e = l_0 + C_I\sqrt{A_o}$, where l_0 is the opening thickness (often neglected for thin openings), where $\rho A_o l_e$ defines the mass of the air-slug.

$$\rho A_o l_e \ddot{x} + \frac{\rho A_o}{2k^2}\dot{x}|\dot{x}| + \frac{a_s^2 \rho A_o^2}{V}x(t) = A_o p_e(t) \qquad 2.8$$

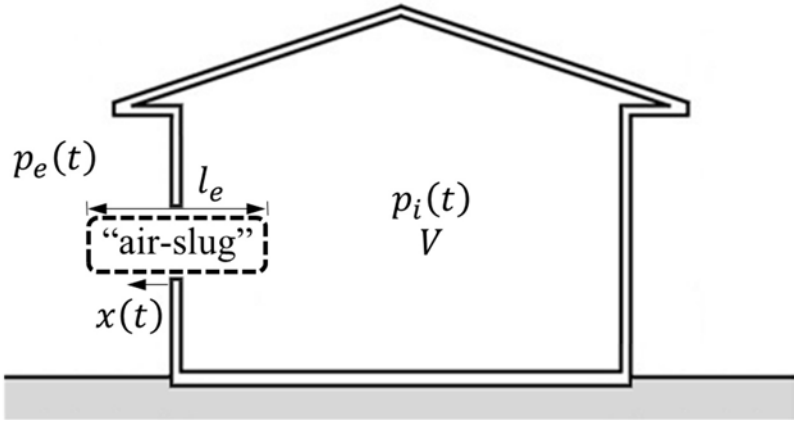

Figure 2.4. Single building envelope opening – Helmholtz Resonator model

Holmes (1979) showed Equation 2.8 could also be presented in terms of pressure coefficients, given in Equation 2.9 by introducing mass continuity and considering an isentropic process; where the relationship between pressure and density, and pressure and volume is constant (here, $pV^{-\gamma}$ is equivilant to $p\rho^{-\gamma}$ and γ is the ratio of specific heats of air (1.4)). Where $\dot{C}_{p_i}$ and $\ddot{C}_{p_i}$ are the first and second time derivatives of $C_{pi}(t)$. This form of the Helmholtz resonator model is referred to as the governing internal pressure equation for a single opening.

$$\frac{C_I V}{a_s^2\sqrt{A_o}}\ddot{C}_{p_i} + C_L\left[\frac{V\bar{U}_h}{2a_s^2 A_o}\right]^2 \dot{C}_{p_i}|\dot{C}_{p_i}| + C_{p_i}(t) = C_{p_e}(t) \qquad 2.9$$

Liu and Saathoff (1981) derived a similar Equation to that of Holmes (1979) with an additional parameter in the inertial term. Vickery (1991) derives the same equation as Holmes (1979) from Bernoulli's equation and shows that Liu and Saathoff's (1981) derivation is similar, but not equivalent. The undamped resonant frequency of Equation 2.8 and Equation 2.9 is Helmholtz

frequency, f_H given in Equation 2.10. If f_H is within the high energy-containing region of the external pressure fluctuations and the inertial forces dominate damping forces, then amplification of internal pressures fluctuations will occur around f_H relative to the external pressure fluctuations.

$$f_H = \frac{1}{2\pi}\sqrt{\frac{\gamma p_0 A}{V \rho_a l_e}} = \frac{a_s}{2\pi}\sqrt{\frac{\sqrt{A}}{C_I V}} \qquad 2.10$$

The Helmholtz resonator model describes the unsteady motion of air through an opening with small dimensions relative to the driving wavelengths, such that the air moves as a whole body through the opening. This consideration is acceptable for more spatially correlated external pressures on openings, like that of windward walls, wake regions, and small openings (i.e. window or door), where the average eddy size is large compared to the opening dimensions. However, air flow across openings (i.e. shear/grazing flow) induces different eddy formation across the opening, requiring additional considerations when analysing the external pressure excitation signal (Sharma and Richards (2003)). This thesis is focused on windward openings, and the effect of grazing flow is not examined.

2.4.1. Single Opening Internal Pressure Simulation

The time-varying internal pressure is theoretically derived by applying a specified external pressure signal $C_{p_e}(t)$ to Equation 2.9, with constant input parameters A_o, V, $\overline{U}_h$, C_I and C_L to define a simulated internal pressure signal $C_{p_i,sim}(t)$, where a finite difference method is used to describe the first and second time-derivatives $\dot{C}_{p_i}$ and $\ddot{C}_{p_i}$ (details on the numerical simulation is detailed in Appendix A). The influence of C_I and C_L on the internal pressure fluctuations is shown in Figure 2.5 a) and b), where simulated internal pressure spectra, $S_{p_i,sim}(f)$, calculated

with the same external pressure signal, with different C_I and C_L values to illustrate their influence on the internal pressure response.

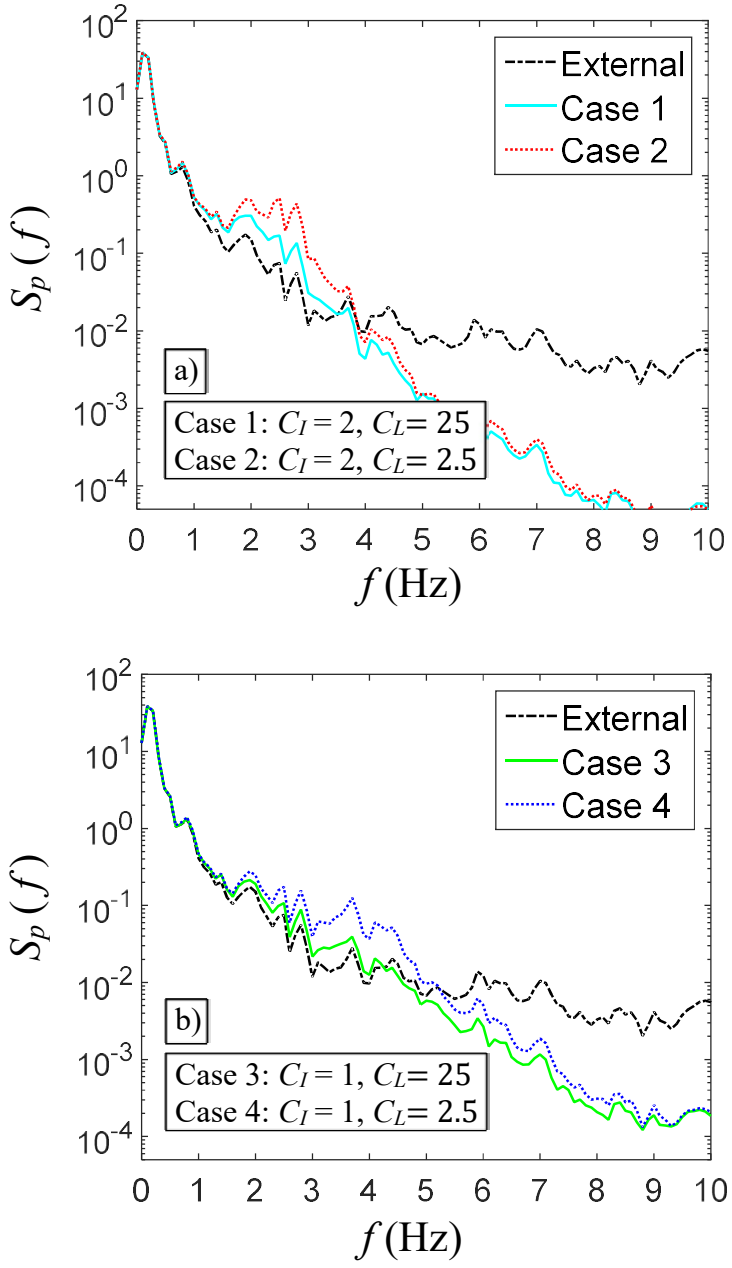

Figure 2.5. a) and b) Simulated internal pressure spectra with a range of C_I and C_L values

Here, Figure 2.5 a) have C_I values greater than Figure 2.5 b). The greater C_I decreases the Helmholtz resonant frequency, shifting it into the higher energy-containing range of the external pressure fluctuations. Figure 2.5 a) and b) also show that greater C_L values damp internal pressure fluctuations, which significantly influences the magnitude of resonance. As C_I and C_L values are ill-defined in literature, simulated internal pressure signals are not reliable for accurate prediction of internal pressures.

Inertial and loss coefficients can be estimated by matching the simulated internal pressure spectra $S_{pi,sim}(f)$ to a measured internal pressure spectra $S_{pi}(f)$ from an experimental internal pressure study. Where the C_I and C_L values are defined in an iterative process by matching the magnitude and frequency of Helmholtz resonance in $S_{pi,sim}(f)$ with $S_{pi}(f)$. Several internal pressure studies have employed this method to define C_I and C_L values, where it is temporally averaged C_I and C_L values are used for the whole time series, however, this may not accurately represent the actual flow conditions through the opening. Further details on C_I and C_L are discussed in Section 2.9.2 and Section 2.9.3.

It is noted that to correctly simulate the internal pressure (i.e. $p_{i,sim}(t)$) requires the same input parameters A_o, V, $\overline{U}_h$, and $p_e(t)$ that characterised $p_i(t)$. Here the specified $p_e(t)$ has to be equivalent to the external pressure signal applied to the opening, often estimated in wind-tunnel model studies by sealing the opening and measuring the spatially averaged external pressure across the opening for the same approach wind conditions.

2.5. Porous Building with a Single (Dominant) Opening

An opening is considered dominant if the external pressure on the opening significantly influences the internal pressure. Cook (1986) suggests that once an opening contributes to about 80% of the mean internal pressure, it should be considered dominant. From Equation 2.5, a large opening on the windward wall requires $A_W/A_L = 2$ to satisfy the 80% threshold, where $\bar{C}_{p_i} = 0.8\bar{C}_{p_eW} + 0.2\bar{C}_{p_eL}$, this is also the same condition for a large opening in AS/NZS 1170.2 (2011), where the internal pressure coefficient $C_{pi} = 0.7C_{p_eW}$ for $A_W/A_L = 2$.

Fahrtash and Liu (1990) conducted full-scale internal pressure measurements in three separate buildings with large openings present and did not observe Helmholtz resonance. They proposed this was due to damping from large building porosity and flexibility. However, they were able to show that large openings do significantly increase the internal pressure fluctuations as suggested by the theory.

Vickery and Bloxham (1992) studied internal pressure in a porous building with a dominant windward opening experimentally in a wind tunnel. Vickery and Bloxham (1992) show that porosity has a minor influence on the internal pressure fluctuations for $A_W/A_L > 10$. They also show that once $A_W/A_L < 3$, internal pressures are significantly reduced relative to the external pressures on the windward opening.

Woods and Blackmore (1995) studied internal pressures in a model-scale building with a range of single large openings and conducted tests with a sealed envelope ($A_L = 0$) and a porous leeward (opposite) wall. Woods and Blackmore (1995) suggested that once $A_W > A_L$, the porosity has a negligible influence on the mean internal pressure, suggesting the steady-state theory (Equation 2.4) gave poor agreement with measurements. However, their measurements are questionable as there is a large variation in the mean and peak internal pressure coefficients. For example, while the windward opening area was 25% of the windward wall, the introduction of the porous opening area of 1.5% of the leeward wall (A_W/A_L = 16.7), resulted in an increase in $\bar{C}_{p_i}$ of 5.5% and a decrease of $\hat{C}_{p_i}$ by 21%, opposite to typical conventions, with similar conclusions for other opening area ratios and wind directions.

More recently, Yu *et al.* (2008) studied internal pressures in porous buildings with a dominant windward wall opening and found that mean and fluctuating internal pressure coefficients decrease relative to the windward wall pressures as the porous opening area A_P increases. To account for the damping influence of A_P, Yu *et al.* (2008) applied an additional damping term to Equation 2.9, producing Equation (2.11. Where A_P, A_o, and k_P are the sum of the leeward porous opening areas, the single large windward wall opening area, and the discharge coefficient of the porous openings respectively.

$$\frac{l_e V}{a_s^2 A_o}\ddot{C}_{p_i} + \frac{A_P k_P l_e}{A_o \bar{U}_h \sqrt{(C_{p_i} - \bar{C}_{p_e,L})}}\dot{C}_{p_i} + \left[\frac{V\bar{U}_h}{2k a_s^2 A_o}\right]^2 \cdot \left(\dot{C}_{p_i} + \frac{2A_P k_P a_s^2}{V\bar{U}_h} \cdot \sqrt{(C_{p_i} - \bar{C}_{p_e,L})}\right) \cdot \left|\dot{C}_{p_i} + \frac{2A_P k_P a_s^2}{V\bar{U}_h} \cdot \sqrt{(C_{p_i} - \bar{C}_{p_e,L})}\right| + C_{p_i} = C_{p_e,W} \quad (2.11)$$

Yu *et al.* (2008) derived Equation (2.11 by assuming that the inertial effects of flow through the porous openings is negligible, and the internal pressure fluctuations induced from the negative external pressure applied to A_P is insignificant compared to the internal pressure fluctuations induced from the external pressures applied to the large windward opening. Thus, a single spatially and temporally averaged leeward wall pressure coefficient is applied to the leeward wall openings. It should be noted that as the porous opening area A_P approaches 0, Equation (2.11 becomes Equation 2.9.

Yu *et al.* (2008) and Kim and Ginger (2013) conducted porous model-scale wind-tunnel experiments and deduced that the attenuation of internal pressure fluctuations from the envelope porosity can be satisfactorily estimated by Equation (2.11 by deriving *k* and k_p by matching the internal pressure coefficient spectra $S_{C_{pi}sim}(f)$ from Equation (2.11, with the experimental $S_{C_{pi}}(f)$.

Oh (2004) and Oh *et al.* (2007) show that flow through very long and slender openings (like that of small porous openings) is similar to a pipe, and conclude that frictional shear stresses should be considered for such openings. This consideration was adopted for the flow through the porous openings in a model-scale wind tunnel building assessed by Guha *et al*. (2011a).

Guha *et al*. (2011a) studied internal pressures in a porous model-scale building in a wind tunnel with a dominant windward opening, both numerically and experimentally. Guha *et al*. (2011a) modified Equation (2.11 to incorporate the linearization of the discharge equation through lumped leakage areas, described by Vickery and Bloxham (1992), and applied additional frictional shear stresses to the flow through the porous openings by substituting a representative

porous opening loss coefficient into the equation that incorporated the shear stress losses. Guha *et al*. (2011a) also showed that the damping effect of building porosity could be satisfactorily estimated in the model-scale building using this theoretical method with respect to the experimental data.

Oh et al. (2007) also studied internal pressure in a porous model-scale building in a wind tunnel with a dominant windward opening, establishing a Multiple-Discharge-Equation (MDE) approach to simulate internal pressures, similar to an MDE model by Vickery (1986). The MDE approach incorporates the empirical pipe like flow through the porous openings, described by Shaw (1981), while also incorporating frictional shear stresses. Oh *et al.* (2007) showed this method provided an adequate prediction of the mean and fluctuating internal pressures when k_p = 0.38 (C_L = 6.9) while using a fixed value of k = 0.63 (C_L = 2.5).

2.6. Nominally Sealed Buildings

Buildings inherently have small openings around the envelope, described as background leakage, (e.g. gaps around fitments in walls, under and around window and door seals, etc.). When all windows and doors are closed, nominally sealed buildings are considered porous. The magnitude of porosity $\varepsilon = A_P/A_T$, is the ratio of the sum of porous opening areas A_P, relative to the total surface area A_T. The magnitude of building porosity (i.e. background leakage) significantly varies depending on the purpose and construction of the building or surface (e.g. fire-resistant walls are considered impermeable, whereas glazed or lightweight metal clad walls are considered leaky).

Vickery (1986) and Harris (1990) analysed flow through small openings, such as those in porous building envelopes. Vickery (1986) and Harris (1990) concluded that the flow is laminar (and unsteady) through small porous openings as the flow paths are in the order of centimetres long and a few millimetres wide. They were able to show that inertial effects of the flow through the porous openings is negligible compared to the frictional losses. Vickery (1986) and Harris (1990) derived a function to describe the unsteady flow into a uniformly porous building by applying this reasoning to a Multiple-Discharge -Equation (MDE) for porous opening areas that

are separated into windward and leeward openings, which experience positive and negative external pressure respectively. From this, Vickery (1986) was able to calculate the range of external pressure fluctuations transferred through the envelope, defined as the characteristic frequency f_c of the building, given in Equation 2.12.

$$f_c = \frac{1}{2\pi}\left(\frac{k_P a_s^2 (A_W^2 + A_L^2)^{3/2}}{V\bar{U}_h A_W A_L \sqrt{(\bar{C}_{p_e,W} - \bar{C}_{p_e,L})}}\right) \quad 2.12$$

Here $\bar{C}_{p_e,W}$ and $\bar{C}_{p_e,L}$ are the spatially and temporally averaged pressure coefficients across the windward and leeward walls, and A_W and A_L are the sum of the porous opening areas across the windward and leeward walls. The interpretation of f_c by Vickery (1986) is that external pressures with frequencies above f_c are attenuated and not passed effectively through the leakage paths into the building. Conversely, fluctuations below f_c are transferred through the envelope, inducing internal pressure fluctuations. Equation 2.12 shows that as building porosity increases, the range of internal pressure fluctuations also increases, but decreases as the building volume and wind speed increases.

2.7. Non-Dimensional Characterization

Holmes (1979) showed that Equation 2.9 which expresses $C_{p_i}(t) = f\left(C_{p_e}(t), \bar{U}_h, A_o, V, C_I, C_L\right)$, could be expressed non-dimensionally as Equation 2.13, such that $C_{p_i}(t^*) = f(\Phi_1, \Phi_2, \Phi_3, \Phi_4, \Phi_5, C_I, C_L)$. The non-dimensional parameters are:

$$\Phi_1 = \frac{A_o^{3/2}}{V};\ \Phi_2 = \frac{\mathrm{a_s}}{\bar{U}_h};\ \Phi_3 = \frac{\rho \bar{U}_h \sqrt{A_o}}{\mu};\ \Phi_4 = \frac{\sigma_\mathrm{u}}{\bar{U}_h};\ \Phi_5 = \frac{\lambda_u}{\sqrt{A_o}};\ t^* = \frac{t\bar{U}_h}{\lambda_u}$$

$$C_I \frac{1}{\Phi_1 \Phi_2^2 \Phi_5^2} \frac{d^2 C_{p_i}}{dt^{*2}} + \left(\frac{C_L}{4}\right)\left(\frac{1}{\Phi_1 \Phi_2^2 \Phi_5}\right)^2 \frac{dC_{p_i}}{dt^*}\left|\frac{dC_{p_i}}{dt^*}\right| + C_{p_i}(t^*) = C_{p_e}(t^*) \qquad 2.13$$

Here Φ_1 is the area to volume parameter, Φ_2 is the inverse of Mach number, Φ_3 is Reynolds number where μ is the absolute viscosity of air, Φ_4 is the approach turbulence intensity, and Φ_5 is the integral length-scale of turbulence λ_u (i.e. dominant wind gust (i.e eddy) length) relative to the size of the opening. The non-dimensional time t^* is time t, relative to the dominant wind gust duration $t^* = t\bar{U}_h/\lambda_u$.

Ginger *et al.* (2008, 2010) show that $\Phi_1\Phi_2^2$ can be combined to characterise an opening area to building volume parameter $S^* = \left(A^{3/2}/V\right)(a_s/\bar{U}_h)^2$. Yu et al. (2006) derived a similar equivalent parameter $S = \left(a_s^2/\bar{C}_{pW}\bar{U}_h^2\right)^{2/3}\left(A/V^{2/3}\right)$, and Vickery and Bloxham (1992) also described a similar opening size parameter $S = (a_s/\bar{U}_h)\left(A^{3/4}/V^{1/2}\right)$.

Sharma (2013) describes a non-dimensional equation similar to Equation 2.13, given in Equation 2.14. Sharma (2013) concluded the internal pressure dynamics and external pressure characteristics can be treated separately, deriving a separate non-dimensional time t_H relative to the Helmholtz frequency, $t_H = tf_H$. This definition produces a similar parameter to S^*, by defining a non-dimensional inertial ratio M_r, which is the volume ratio between the 'air-slug' and the building, and a non-dimensional length parameter φ_5, which is the length ratio between the approach integral turbulence length scale and the 'air-slug' length. The definition of M_r and φ_5 are shown below. The terms are also represented in non-dimensional parameters defined by Holmes (1979) and Ginger *et al.* (2008).

$$M_r = \frac{Al_e}{V} = C_I\Phi_1; \quad \varphi_5 = \frac{\lambda_u}{l_e} = \frac{\Phi_5}{C_I};$$

$$S^{**} = M_r \left(\frac{a_s}{\overline{U}_h}\right)^2 = C_I \Phi_1 \Phi_2^2 = C_I S^*$$

$$\frac{d^2 C_{p_i}}{dt_H^2} + \left(\frac{C_L}{4S^{**}}\right)\frac{dC_{p_i}}{dt_H}\left|\frac{dC_{p_i}}{dt_H}\right| + (2\pi)^2 C_{p_i}(t_H) = (2\pi)^2 C_{p_e}(t_H) \qquad 2.14$$

Vickery and Bloxham (1992), Yu et al. (2006) and Ginger *et al.* (2008) and others have shown that internal pressure fluctuations are a function of S^* and Φ_5, where a decrease in S^* and Φ_5 increases the non-linear damping and inertial terms in Equation 2.13. While increasing damping, it also decreases Helmholtz frequency, shifting it towards greater energy-containing frequencies within the external pressure fluctuations; thus the influence on the internal pressure response cannot be clearly determined without experimental testing.

The governing equation that incorporates damping from envelope porosity, given in Equation (2.11, was non-dimensionalized by Kim and Ginger (2013), in terms of the non-dimensional parameters defined by Holmes (1979) and Ginger *et al.* (2008), given in Equation 2.15. Here the ratio of the area of porous openings to the dominant opening area is defined as $\Phi_6 = A_P/A_o$. It can be shown that as Φ_6 approaches zero, Equation 2.15 becomes Equation 2.13. Here k $\left(= 1/\sqrt{C_L}\right)$ and k_P are the discharge coefficients of the single large opening and the porous openings respectively, and $\bar{C}_{p_e,L}$ is the spatially and temporally averaged leeward wall pressure coefficient.

$$\frac{C_I}{S^*\Phi_5}\frac{d^2 C_{p_i}}{dt^{*2}} + k_P\frac{\Phi_6}{\Phi_5}\frac{C_I}{\sqrt{\left(C_{p_i} - \bar{C}_{p_e,L}\right)}}\frac{dC_{p_i}}{dt^*} + \frac{k_P^2}{k^2}\Phi_6^2\left(C_{p_i} - \bar{C}_{p_e,L}\right)$$
$$+ \frac{k_P}{k^2}\frac{\Phi_6}{S^*\Phi_5}\sqrt{\left(C_{p_i} - \bar{C}_{p_e,L}\right)}\frac{dC_{p_i}}{dt^*} + \left(\frac{1}{4k^2}\right)\left(\frac{1}{S^*\Phi_5}\right)^2\frac{dC_{p_i}}{dt^*}\left|\frac{dC_{p_i}}{dt^*}\right| + C_{p_i} = C_{p_e,W} \qquad 2.15$$

2.7.1. Volume Scaling

Holmes (1979) applied dimensional analysis to the internal pressure response and showed that the internal volume of model-scale buildings must be distorted in order to correctly simulate full-scale internal pressure fluctuations. Holmes (1979) shows that the model-scale to full-scale building volume ratio $V_r = [V_{model}/V_{full}]$ is equal to the length-scale cubed $[L_r^3]$, divided by the wind velocity ratio squared $[U_r^2]$; $[V_r] = [L_r^3]/[U_r^2]$. This is typically achieved in wind-tunnel tests by extending the vertical depth of the model below the wind tunnel floor to achieve the desired building volume.

The same volume-scaling requirement is also obtained using alternative non-dimensional parameters based on matching Helmholtz frequency f_H and the characteristic frequency f_c with the frequencies in the approach wind flow. The same relationship can also be described by matching the non-dimensional opening area to building volume parameter S* between model-scale and full-scale. Further discussion of the volume scaling is detailed by Holmes and Ginger (2012), Guha *et al.* (2011a) and others.

Internal pressure response in nominally sealed buildings and buildings with openings in the envelope can be presented in terms of S*, thus accounts for variations that result from differing approach wind velocity and volume of a building.

2.8. Internal to External Pressure Response

Vickery and Bloxham (1992), Irwin and Dunn (1994), Sharma and Richards (1997, 2003), Yu et al. (2006), Ginger *et al.* (2008), and others have quantified the internal pressure fluctuations relative to the external pressure fluctuations applied to the dominant opening in terms of the standard deviation pressure ratio $C_{\sigma p_i}/C_{\sigma p_e}$, peak pressure ratio $\hat{C}_{p_i}/\hat{C}_{p_e}$ and admittance function (i.e. transfer function) $\left|X_{i/e}(f)\right|^2 = S_{C_{p_i}}(f)/S_{C_{p_e}}(f)$, where $\left|X_{i/e}(f)\right|^2$ is the frequency response of the internal pressure fluctuations.

Holmes and Ginger (2012) presented a review of the internal pressure response from several experimental wind tunnel studies and theoretical methods. They produced empirical formulas (given in Equation 2.16 and 2.17), to describe the internal to external standard deviation pressure ratio $C_{\sigma p_i}/C_{\sigma p_e}$ with respect to S^* and Φ_5, presented in Figure 2.6.

For $S^* \geq 1.0$:
$$\frac{C_{\sigma_{p_i}}}{C_{\sigma_{p_e}}} = 1.1 \qquad 2.16$$

For $S^* \leq 1.0$:
$$\frac{C_{\sigma_{p_i}}}{C_{\sigma_{p_e}}} = 1.1 + \left(\frac{4}{\Phi_5}\right)\log_{10}(S^*) \qquad 2.17$$

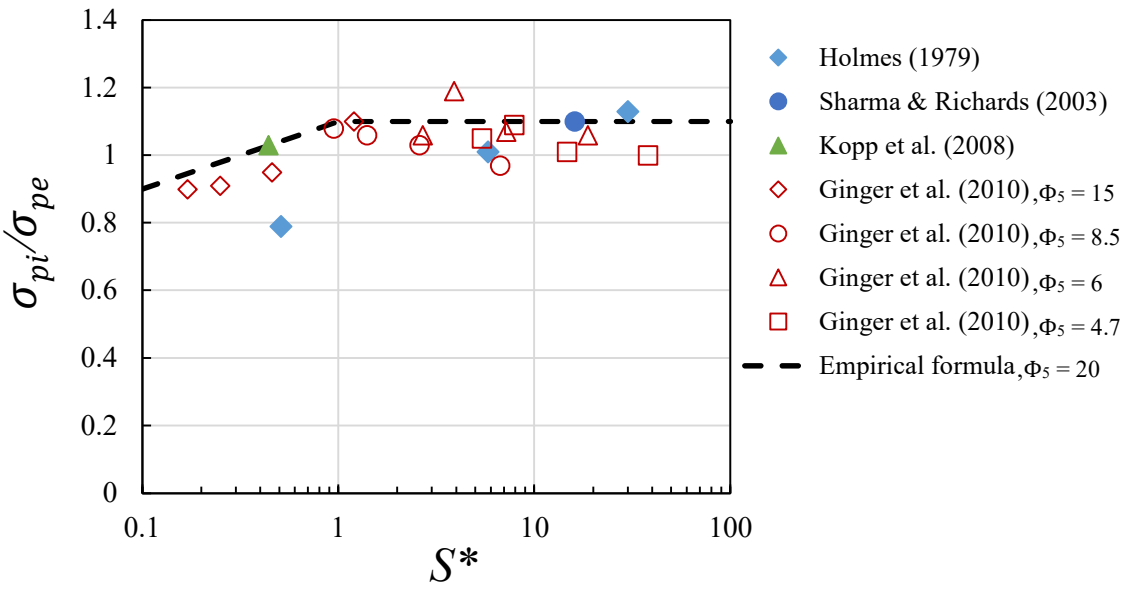

Figure 2.6. Internal to external standard deviation pressures ratio versus S* – Holmes and Ginger (2012)

Holmes and Ginger (2012) consider the ratio of peak internal pressures to peak external pressures applied to the opening (critical for design pressure estimates), as Equation 2.18. Here g is a peak pressure factor (described in detail by Holmes et al. (2014)), typically within 3.5 to 4, and I_u is the approach turbulence intensity ($I_u = \Phi_4$).

$$\frac{\hat{C}_{p_i}}{\hat{C}_{p_e}} = \frac{1 + 2gI_u\left(\frac{C_{\sigma_{p_i}}}{C_{\sigma_{p_e}}}\right)}{1 + 2gI_u} \qquad 2.18$$

2.9. Other Factors Influencing Internal Pressures

2.9.1. Envelope Flexibility

The Helmholtz resonator model is applied to a fixed volume (i.e. a building with a rigid envelope). However, the envelope of a building (especially sheet metal cladding) deforms relative to net (external and internal) pressures, distorting the internal volume. The volume distortion alters the internal air density and pressure fluctuations. Consideration of the effect of volume distortion on the internal air density/pressure can be analysed with the conservation of mass in the enclosure.

Vickery (1986) showed the continuity of the mass-flow rate into a flexible building is defined by Equation 2.19, which requires an additional volume distortion term $\partial V/\partial t$. The additional term reduces the rate of change of the air density (and pressure) relative to the flow into or from the volume.

$$\sum_{j=1}^{N} Q_j \rho_i = V \frac{\partial \rho_i}{\partial t} + \rho_i \frac{\partial V}{\partial t} \qquad 2.19$$

Vickery (1986) showed that the influence of volumetric change on the internal pressure fluctuations could be characterized in the theoretical analysis by adopting a larger building volume that accounts for the additional volume distortion.

Vickery (1986) showed that the volumetric strain of the building, i.e. bulk modulus of the building K_B, can describe the volume distortion relative to the internal pressure. The Bulk modulus of the building is defined as the change in the net pressure across the envelope Δp per unit volumetric strain $\Delta V/V$, where $K_B = \Delta p/(\Delta V/V)$.

The building volume is increased by the ratio of the bulk modulus of the building K_B, relative to the bulk modulus of air K_A, given in Equation 2.20. Here, V_B is the standard building volume; V is the effective building volume, $K_A = \gamma p_o$, and p_o is atmospheric pressure, where K_A = 1.419 × 10^5 Pa. Vickery (1986) showed that for a considerably stiff or flexible building K_A/K_B may range between 0.2 and 5 respectively.

$$V = V_B(1 + K_A/K_B) \qquad 2.20$$

The effective building volume V replaces the building volume term in all internal pressure equations. This method was adopted for the internal pressure analysis of the WERFL full-scale low-rise test building at Texas Tech University (TTU) by Ginger *et al.* (1997), where the effective building volume was found to be 1.5 times greater than the standard building volume

($V = 2.5V_B$). They found this was a reasonable method to incorporate the influence of envelope flexibility into numerical methods to describe internal pressures fluctuations.

It should be noted that Vickery (1986) and Harris (1990) showed that for lightweight, large span buildings, the deformation of the envelope from net pressure fluctuations, can influence a dynamic building response, and should be assessed for large span lightweight industrial buildings and super light air-supported structures. However, only typical industrial type buildings are assessed in this thesis.

2.9.2. Loss Coefficient

The loss coefficient C_L ($= 1/k^2$, where k is a discharge coefficient) represents energy losses through an opening from a combination of viscous, shear stresses, expansion, contraction, and miscellaneous losses. The loss coefficient of steady flow through orifices, under isochoric conditions, has been studied extensively and is often described as $C_L = 2\Delta p / \rho U_0^2$, where Δp is the pressure loss through the opening and U_0 is the spatially averaged velocity through the orifice. As early as 1929, Johansen (1930) showed that the discharge coefficient k is a function of the Reynolds number Re through the orifice and the orifice diameter ratio (orifice diameter relative to pipe diameter, d/D). Where Re of the flow describes the ratio of inertial forces relative to the viscous forces, given by $Re = uL/\nu$, where L is the characteristic length (i.e. opening diameter d) and ν is the kinematic viscosity of the fluid.

Figure 2.7 presents the experimental results by Johansen (1930) which show the discharge coefficient (C_D in Figure 2.7) with $\sqrt{Re}$ for a range of d/D ratios, for $0.4 \leq Re \leq 25000$ (where $\sqrt{25000} \cong 160$). Here the discharge coefficient increases from $k = 0.05$ ($C_L = 400$) at $Re = 0.4$ to their maximum between Re of 150 to 600 (depending on the d/D ratio) and gradually decreases to a constant value of $k = 0.615$ ($C_L = 2.64$) as the flow becomes turbulent at Re > 2000. Johansen (1930) concluded that the discharge coefficient increases linearly for $0.4 \leq Re \leq 9$, where $C_L \cong 40/Re$ for the four orifice diameter ratios examined (0.209, 0.401, 0.595, and 0.794).

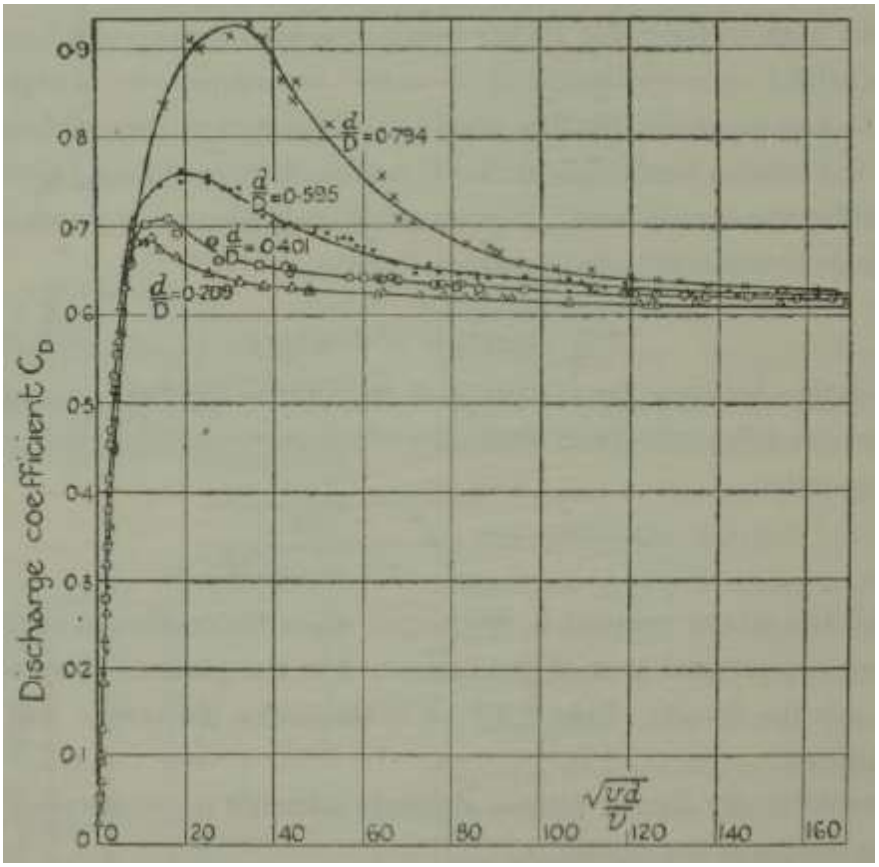

Figure 2.7. Discharge coefficient versus $\sqrt{Re}$ for flow through an orifice plate – Johansen (1930)

Low *Re* hydrodynamics has also been examined by Bond (1920), Happel and Brenner (1965), Hasegawa *et al.* (1997) and others. Kusmanto *et al.* (2004) explained that Bond (1920) conducted experiments on viscous flow through short tubes and shows that C_L is also related to the orifice thickness l to diameter ratio (l/d), where $C_L = (36.7 + 64l/d)/Re$. Dagan *et al.* (1982) later solved the Navier-Stokes problem for viscous flow through an orifice with a finite thickness, where $C_L = (12\pi + 64l/d)/Re$. Here $12\pi = 37.7$ which is very similar to the experimental results from Bond (1920) and Johansen (1930).

Grose (1983) suggests that the orifice discharge coefficient k is a product of three coefficients each accounting for a factor in the pressure loss; a viscosity effect coefficient C_v, contraction coefficient C_c, and velocity profile coefficient C_u, where $k = C_v \times C_c \times C_u$. Grose showed that for Re < 16, C_c and C_u are unity, and the viscosity effect coefficient C_v has excellent agreement with experimentally determined discharge coefficients. Figure 2.8 illustrates the contraction coefficient C_c (ε in Figure 2.8), combination of the velocity and viscosity coefficients ($\varphi = C_v \times C_u$ in Figure 2.8), and discharge coefficient (μ in Figure 2.8), as a function of Re from Idel'Chik (1960) handbook on hydraulic resistance.

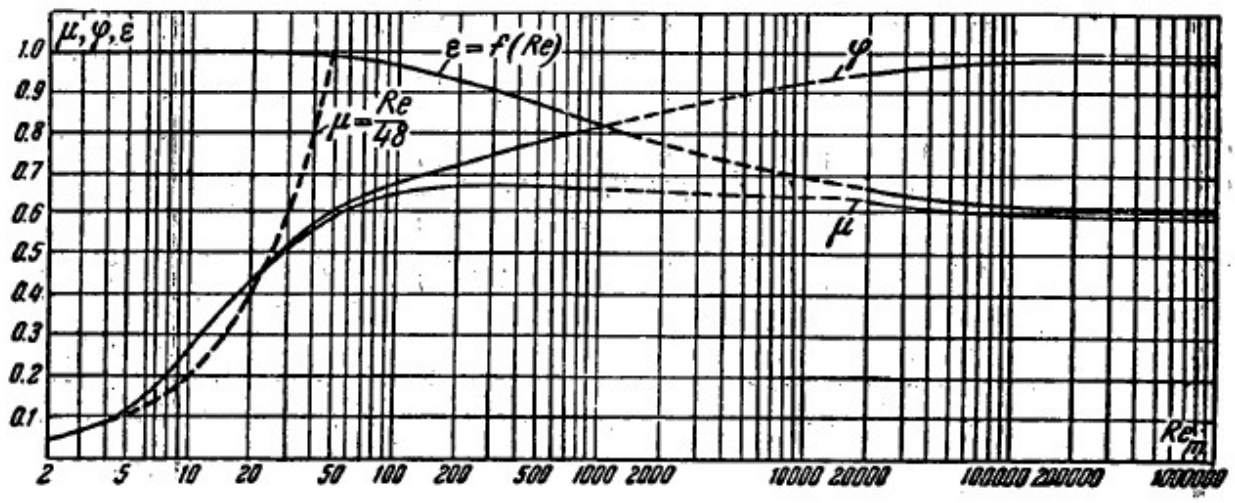

Figure 2.8. Curves of the contraction coefficient ε, velocity-viscous coefficient φ, and the discharge coefficient μ, for a sharp-edged orifice, as a function of Re – Idel'Chik (1960)

Bohra (2004) conducted a wide range of orifice flow experiments for $0.09 \leq Re \leq 9677$, $0.3 <$ l/d < 5.72 and $0.02 <$ d/D < 0.137 ratios, detailing the loss coefficient relative to Re shown in Figure 2.9, where the loss coefficient is equivalent to the Euler number Eu. Bohra shows that the slope of the loss coefficient is steeper than the predicted $(64/Re)(l/d)$ for Re < 6, and developed a numerical solution for the loss coefficient as a function of *Re, l/d, d/D*, and the dynamic viscosity for the ratios examined.

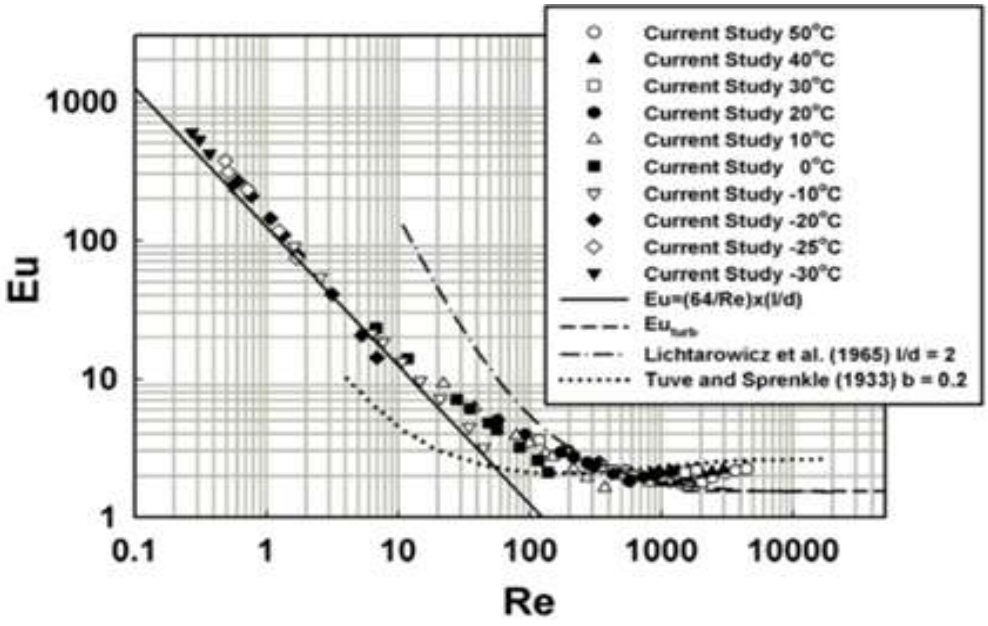

Figure 2.9. Loss coefficient (Euler number) versus *Re* (for l/d = 2, and d/D = 0.023) – Bohra (2004)

The range of orifice flow studies has been extensive, however, detailed studies of the discharge/ loss coefficient for unsteady flow fluctuating back and forth through an orifice or irregular opening are very limited.

Heiselberg *et al.* (2001) conducted full-scale ventilation tests of steady flow through hinged windows. They showed that the loss coefficient varies at lower pressure differentials across the opening and becomes constant for larger pressures as the velocity increases and suggested a Reynolds number dependence at low pressure differentials.

Karava *et al.* (2004), Holmes and Ginger (2012), and Sharma (2013) presented reviews of internal pressure studies which examined the loss coefficient for fluctuating flow in model-scale, full-scale, and CFD studies. They show that the derived loss coefficient C_L ranges between 0.75 (k = 1.15) from Chaplin *et al.* (2000) to 400 (k = 0.05) from Kim and Ginger (2013) showing a lack of consistency between studies.

2.9.2.1. Loss Coefficients from unsteady flow

Vickery and Karakatsanis (1987) derived C_L values for unidirectional flow through a range of porous opening configurations from low turbulence intensity model-scale wind tunnel experiments. They deduced that C_L of the porous openings was highly dependent on the Reynolds number through the openings, where $C_L \cong 4.0 \pm 0.2$ ($k \cong 0.5 \pm 0.02$) for Re >1200, and C_L increased as *Re* decreased. In this study, the Re through the openings was deduced from measuring the flow through the openings via a calibrated flow meter incorporated in the model.

Chaplin *et al.* (2000) applied sinusoidal excitation pressures to a range of small openings in a model and showed that the loss and inertial coefficients vary as the flow velocity fluctuates through the openings. Chaplin showed that for $100 \leq Re \leq 5800$, the C_L ranges from $1.2 \leq C_L \leq 2.2$ ($0.91 \leq k \leq 0.67$) with a mean C_L of 1.67 ($k = 0.77$), and by decreasing the area, velocity (i.e. *Re)* through the opening increases, which decreased the C_L values.

The derivation of loss coefficients from internal pressure studies in wind tunnels is detailed in Section 2.4.1, where C_L is derived in an iterative process by matching the magnitude of damping in the simulated internal pressure spectra with the measured internal spectra. Several internal pressure studies have employed this method to define C_L values; this method defines a temporally averaged C_L value for the whole time series.

Ginger et al. (2010), Kim and Ginger (2013), Guha et al. (2013b) and Xu et al. (2017) conducted wind tunnel studies and showed that the temporally averaged C_L is a function of the opening area to volume parameter S*. Figure 2.10 and Figure 2.11 show the results by Kim and Ginger (2013) and Xu et al. (2017) where the temporally averaged C_L and k are derived from spectral matching are plotted concerning the S* parameter of the model. Here both studies show that C_L increases (k decreases) as a result of S* increasing.

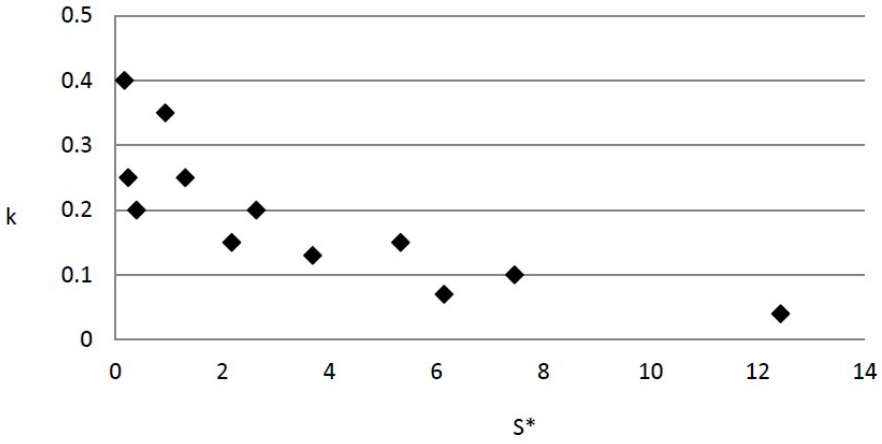

Figure 2.10. Discharge coefficient *k* versus the opening area to volume parameter S* – Kim and Ginger (2013)

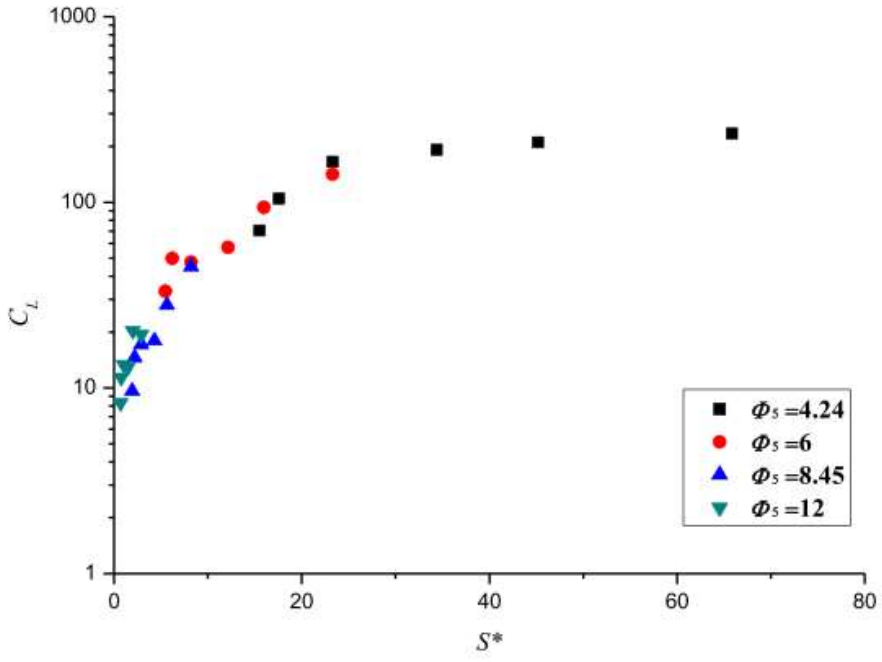

Figure 2.11. Loss coefficient C_L versus the opening area to volume parameter S* – Xu et al. (2017)

Sharma (2013) conducted an internal pressure wind tunnel study incorporating a variable loss coefficient as a function of *Re* using the numerical solution for $C_L = f(Re, l/d, d/D)$ developed by Bohra (2004). Sharma (2013) showed that the range of large temporally averaged loss coefficients from the literature may be explained by the variable *Re* conditions of the flow through the opening and approach wind conditions.

2.9.3. Inertial Coefficient and Effective Length

The product of effective-length l_e, opening area A, and air density ρ describes an equivalent mass of air that has momentum as it passes through an opening, and is described in detail by Vickery (1986). The effective-length l_e is described as $l_e = l + C_I\sqrt{A}$, where l is the thickness of the opening and C_I an inertial coefficient. For a sharp-edged circular orifice connecting two large regions, potential flow theory describe $C_I = \sqrt{(\pi/4)} = 0.886$. For very thin-walled structures, where $\sqrt{A} \gg l$, the opening thickness is neglected (i.e. $l_e = C_I\sqrt{A}$).

The Helmholtz resonator model, discussed in Section 2.4, describes the motion of an air jet ('air-slug') that oscillates backwards and forwards through a single opening to a volume, where the effective length ($l_e = C_I\sqrt{A}$) describes an equivalent air-slug length.

The inertial coefficient C_I is readily calculated from the measured Helmholtz frequency f_H defined in Equation 2.10. Model-scale and full-scale studies have shown the value to range between 0.8 (Xu *et al.* (2014)) to 2.0 (Kim and Ginger (2013)). Some internal pressure studies have adjusted parameters in the governing internal pressure Equation 2.9 to keep C_I constant = 0.89.

Holmes (1979) conducted a model-scale internal pressure study for a single opening in the centre of a windward wall, utilizing C_I = 0.89 and adopting a polytropic exponent 1.2, instead of the ratio of specific heats (1.4). After re-defining the polytropic exponent as 1.4, details C_I = 1.04.

Sharma and Richards (1997) detailed a model-scale wind-tunnel study where C_I varies with the opening location on the windward wall and the ratio of the opening length l to effective radius

$r_{eff} = \sqrt{A/\pi}$. For long openings, $l/r_{eff} > 1.0$, $C_I = 0.98$, and for thin openings $l/r_{eff} < 1.0$, C_I varies with the opening location with $C_I = 1.3$ for an opening in the centre of the wall, $C_I = 1.10$ to 1.21 for an opening adjacent to a floor, and $C_I = 1.5$ for an opening adjacent to the floor and near a sidewall. Sharma and Richards (1997) introduced a contraction coefficient that effectively reduced C_I to between 0.66 to 0.91.

Xu *et al.* (2014) conducted model-scale internal pressure studies for a range of opening area ratios, opening locations, turbulence intensities, wind speeds and different model material. Xu *et al.* (2014) showed that the wind speed, turbulence intensity, wind direction, and opening location (centre, adjacent to floor and adjacent to sidewall) have a small effect on the C_I value. Xu *et al.* (2014) defined a constant $C_I = 0.8$ and shows that if the building model flexibility is not included in the analysis, it will effectively increase C_I due to the incorrect effective model volume, suggesting the influence of flexibility should be corrected before analysis.

2.9.4. Quasi-Steady Theory

Wind loading codes and standards (i.e. Australian and New Zealand design loads for wind action AS/NZS 1170.2 (2011), and American Society of Civil Engineers ASCE 7 (ASCE (2011)), apply a quasi-steady approximation which implies that all pressure fluctuations are due to gusts within the approach boundary layer. This method estimates peak (i.e. design) pressures, $\hat{p}$ and $\check{p}$ from a design gust wind speed at the mid-roof-height of the building (a 0.2-second gust from a 10-minute signal for AS/NZS1170.2), $\widehat{U}_h$, and a quasi-steady pressure coefficient $\tilde{C}_p$. The quasi-steady pressure coefficient $\tilde{C}_p$ is similar to the temporally averaged pressure coefficient $\bar{C}_p = \bar{p}/[½\rho\overline{U}_h^2]$ (where $\tilde{C}_p = C_{fig}$ from AS/NZS 1170.2 (2011)). Thus, the quasi-steady method to define peak (i.e. design) surface pressures $\hat{p}$ (or $\check{p}$) = $\tilde{C}_p ½\rho\widehat{U}_h^2$. Here, the quasi-steady method estimates the peak pressure factor G_p (i.e. ratio between the mean and peak pressure, $\hat{p} = G_p \times \bar{p}$) is equal to the velocity gust factor (i.e. peak to mean velocity ratio) squared $\left(\widehat{U}_h/\overline{U}_h\right)^2$.

External quasi-steady pressure coefficients $\tilde{C}_{p,e}$ are similar to the mean pressure coefficients, however, local pressure and area reduction factors are conditionally applied to account for

greater peak pressures in smaller areas behind discontinuities and uncorrelated pressures across greater areas across select surfaces, respectively. Internal quasi-steady pressure coefficients $\tilde{C}_{p,i}$ are also similar to the mean pressure coefficient $\bar{C}_{p,i}$, that is a function of the windward to leeward opening area ratio in Equation 2.5. The internal pressure is also considered to act in a quasi-steady manner, thus ignores inertial and damping effects, and does not adopt external local pressure and area reduction factors.

For a single opening in a building envelope, the quasi-static approximation specifies that the internal pressure fluctuations equal the external pressure fluctuations on the opening, where $\bar{C}_{p,i}/\bar{C}_{p,e} = \hat{C}_{p,i}/\hat{C}_{p,e} = \tilde{C}_{p,i}/\tilde{C}_{p,e} = 1$ and for a building with multiple openings (i.e. a windward and leeward opening), the peak internal pressure $\hat{p}_i(or\ \check{p}_i) = \tilde{C}_{pi}{}^{1}\!/_{2}\rho\tilde{U}_h^2$, where $\tilde{C}_{p,i}$ is defined from Equation 2.5. This method fails to incorporate damping or amplification of internal pressure fluctuations observed in internal pressure studies, where $\hat{C}_{p,i}/\hat{C}_{p,e}$ and $\tilde{C}_{p,i}/\tilde{C}_{p,e}$ fluctuate depending on attenuation and amplification of the internal pressure response, which has shown to be a function of S* from model-scale wind tunnel tests. This dissertation will characterise the conditions when this method may not be appropriate for internal pressure design.

2.10. Chapter Summary

Internal pressure fluctuations inside a nominally sealed building are described by the transfer of external pressure fluctuations through porous surfaces (i.e. background leakage); attenuating pressure fluctuations, and typically contributes to a small fraction of the net design pressures.

The Helmholtz resonator model describes internal pressure fluctuations inside a building with a single (dominant) windward opening; where $C_{pi}(t) = f\left(S^*, \Phi_5, C_I, C_L, C_{pe}(t)\right)$. Numerical methods and model-scale studies have shown the internal pressure response (i.e. amplification or attenuation) is primarily dependent on the opening area to building volume parameter S*. The loss coefficient C_L is also an important parameter that describes the magnitude of damping from viscous losses through an opening. An accurate method to define C_L for a full-scale building opening has not been achieved in previous studies. Further, the inertial coefficient C_I

influences the frequency at which f_H occurs, which has shown small variation from model-scale and limited full-scale studies.

The influence of background leakage has been studied numerically and validated with model-scale studies, however, model-scale studies cannot satisfactorily simulate the flow though full-scale porous building openings due to Re mismatch, producing an inaccurate full-scale internal pressure response.

Study of the influence of background leakage on full-scale nominally sealed buildings and buildings with a large opening and background leakage has not been achieved previously and the overall influence of background leakage on the peak (i.e. design) internal pressures in both Cases is unclear. Full-scale studies presented in this thesis can address these issues, providing internal pressure data for validation numerical methods to improve the prediction of peak (i.e. design) internal pressures, and optimise the structural design of buildings.

In this thesis, unique full-scale experiments characterise the loss coefficient C_L of flow through full-scale openings, and the amplification and attenuation of full-scale internal pressure fluctuations are characterised in terms of S*, improving the theoretical internal pressure analysis from a large windward opening. Internal pressures were also measured in a typical full-scale Industrial Building while nominally sealed and with large windward wall openings. The influence of background leakage on the internal pressure response for both Cases are presented with S*, and accounts for the envelopes flexibility. The results are also analysed with respect to the quasi-static approach to the internal pressure response to characterise the influence on design internal pressures in typical industrial buildings.

CHAPTER 3: CONTROLLED FULL-SCALE TEST ENCLOSURE

This Chapter presents a unique experimental setup and a series of tests along with the results and discussion of internal and external pressure measurements from a range of single windward openings in a controlled Full-Scale Test Enclosure (FSTE). The tests were designed to examine the influence of the opening size and applied pressure fluctuations in a controlled full-scale environment, without the influence of building envelope porosity. The methodology enables the analysis of the loss coefficients in a full-scale environment and characterisation of the internal to external pressure response with respect to S* and other parameters.

3.1. Full-Scale Test Enclosure (FSTE)

The FSTE was designed to measure full-scale, naturally wind-induced external and internal pressures in an air-tight box-shaped structure with a single windward opening in the envelope. The only input variables are the opening dimensions and the external pressure fluctuations on the opening which are a function of the natural approach wind conditions.

The FSTE was a 6 m long, 2.4 m wide and 2.5 m high "20-foot shipping container" with an internal volume of 36 m^3. A rigid timber wall with a single 200 × 200 mm square opening was installed across the 2.4 × 2.5 m doorway of the FSTE, as shown in Figure 3.1, which is completely empty. Wind blowing towards the opening was defined as a wind angle $\theta = 0^o$. A combination of polyurethane sealer, foam tape, expanding foam and adhesive tape was used to ensure all air vents, floorboard joints, and gaps around the timber wall were sealed, and that all surfaces of the FSTE were effectively airtight before testing. Quit

Pressures acting towards a surface are considered positive, and the net pressure across a surface or opening $p_{net}(t)$ is equal to the difference between the external pressure $p_e(t)$ and internal pressure $p_i(t)$, where $p_{net}(t) = p_e(t) - p_i(t)$. Pressures are also described as coefficients relative to the mean approach wind speed, where the pressure coefficient $C_p(t) = p(t)/(½\rho\overline{U}_h)$. Here $\overline{U}_h$ is the temporally averaged wind speed at a 3 m reference height h and

ρ is the density of air (approximately 1.2 kg/m^3). Mean, standard deviation, minimum and maximum pressures over an observed time period, $\bar{p}$, σ_p, $\check{p}$, and $\hat{p}$ respectively, describe the statistical properties of the time-series and the energy in the pressure fluctuations is described in the frequency domain by the power spectral density function, $S_p(f)$ (i.e. spectra).

Figure 3.1. FSTE with 200 × 200 mm opening in the windward wall

3.1.1. Site Exposure

The FSTE was located on the fringe of James Cook University's (JCU) campus at the Cyclone Testing Station facility, shown in an aerial image of approximately 250 m around the site in Figure 3.2. Figure 3.2 also shows the wind angle sign-convention, where $\theta = 0°$ is about 20° from South. Figure 3.3 is an image taken from in front of the timber wall of the upwind surroundings (facing θ = 0°), which is open terrain for an initial 50 m, followed by natural bushland. Figure 3.3 also shows the anemometer and the reference pressure pit location that are discussed in the following sections.

Figure 3.2. Arial photograph of the FSTE site, wind approach angle θ = 0°.

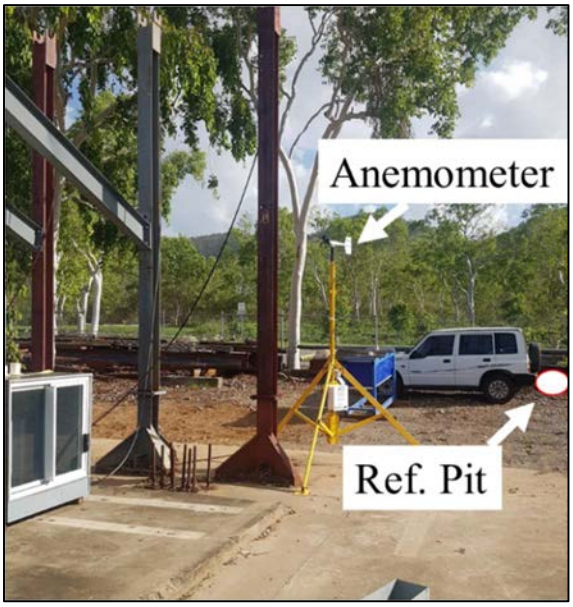

Figure 3.3. Upwind surroundings of the FSTE, facing $\theta = 0°$

3.1.2. Pressure Measurement

Four pressure taps were installed in a 250 mm square pattern centred around the 200 mm square opening, each approximately 35 mm from the corners of the opening, as shown in Figure 3.4. An additional two pressure taps inside the FSTE were used to measure the internal pressure, 1.5 m below the opening, 0.5 m apart from one another, as shown in Figure 3.5. Honeywell TruStability® ±500 Pa differential pressure transducers were connected to the pressure taps via a 200 mm length of 4 mm inner diameter vinyl tubing and solenoid valve, secured in protective casements, shown in Figure 3.6. All pressure transducers were referenced to atmospheric pressure captured from a reference pressure pit (20 L vessel below ground), 15 m South of the FSTE. The lid to the reference pit was flat and flush with the ground surface, with small holes to allow the gradual atmospheric pressure variations.

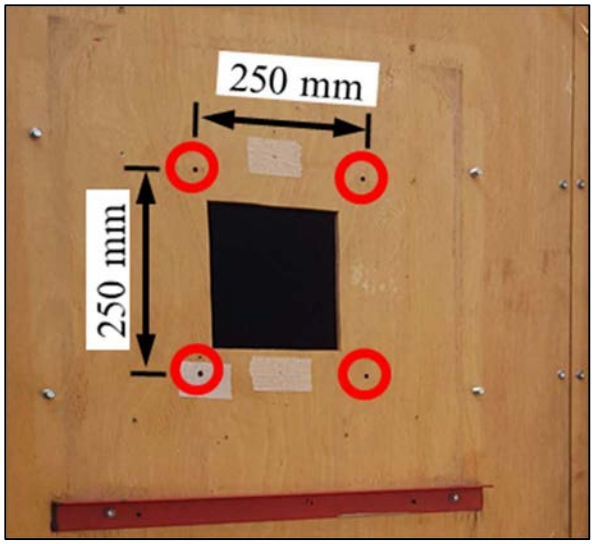

Figure 3.4. FSTE 200 × 200 mm wall opening and external pressure tap locations

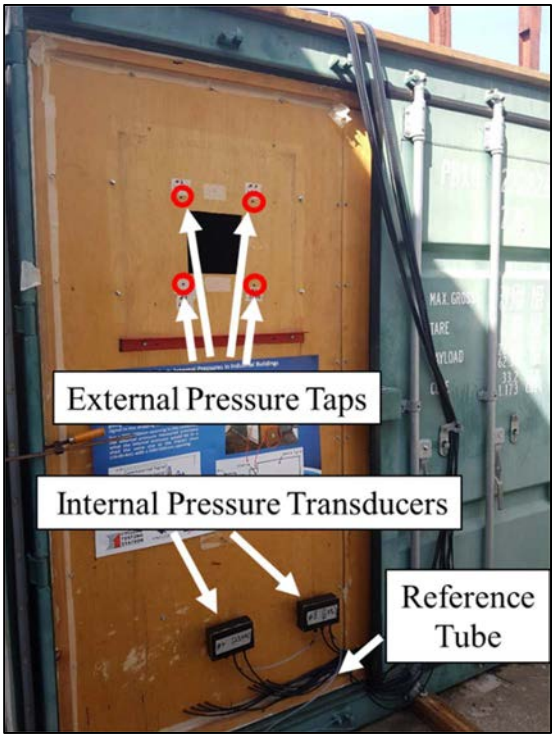

Figure 3.5. FSTE 200 × 200 mm wall opening, indicating external pressure and internal pressure tap locations

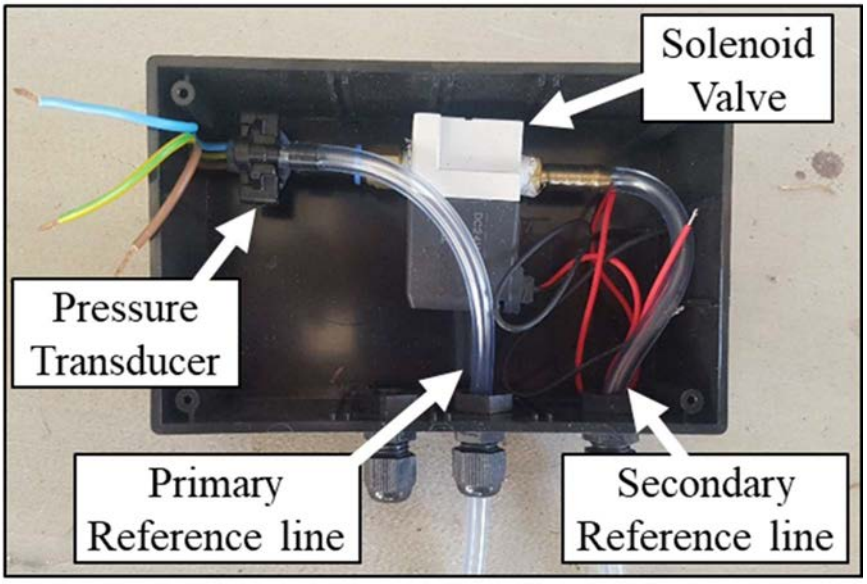

Figure 3.6. Pressure transducer and Solenoid valve in protective housing

Each test captured data at 60 Hz for 10-minutes, which was post-processed to 15 Hz with a moving average filter. The pressure transducers were zeroed for the initial 5 seconds of each test by activating the solenoid valve connected to each pressure transducer that diverts the reference pressure to the active port of the transducer, as described in the line diagram layout, shown in Figure 3.7. Here “PT Active” and “PT Reference” are the pressure transducer active and reference pressure ports.

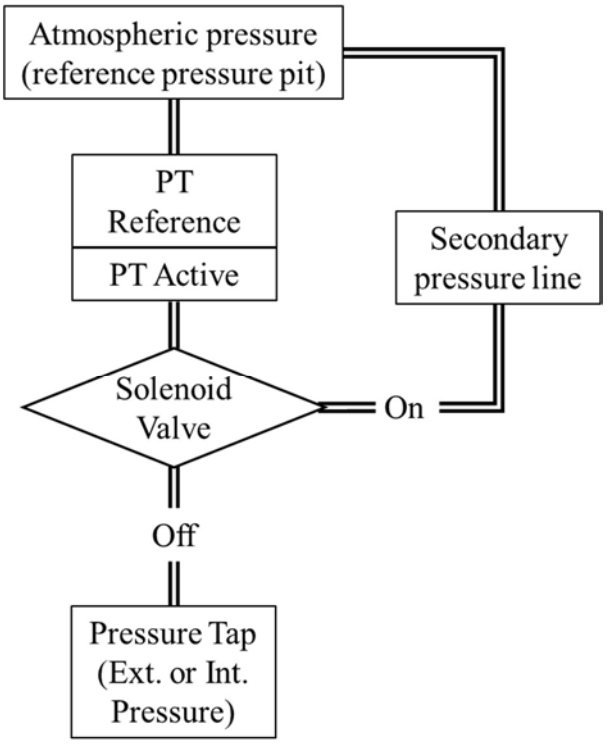

Figure 3.7. Line diagram of pressures transferred to Pressure Transducers (PT) through Solenoid valves

3.1.3. Anemometer

A marine rated R.M. Young propeller anemometer (Model 05106), shown in Figure 3.8, was used to measure the approach wind speed and angle at a height of 3 m from the top of a tripod at a distance of 6 m in front of the FSTE, as shown in Figure 3.3. The wind speed and angle were collected at 10 Hz and post-processed with a 3-second moving average filter.

The integral-time scale of turbulence is defined as the duration of positive correlation of velocity fluctuations obtained by the integration of the auto-correlation function. The integral length-scale of turbulence λ_u is considered equivalent to the integral-time scale of turbulence

multiplied by the mean wind speed. This produced λ_u within the range of 50 m to 150 m (≅ 100 m) during testing.

Figure 3.8. R.M Young Propeller Anemometer (Model 05106)

3.1.4. Data Acquisition

A National Instruments data-acquisition system (NI cDAQ-9174) was used to record the pressure transducer data and actuate the solenoid valves. Further details on the data acquisition user interface and physical system are given in Appendix B. The anemometer had a standalone data-acquisition system that recorded the data on an internal memory card enabling synchronisation between the pressure transducers and anemometer data-acquisition systems when starting each test.

3.1.5. Test Configurations

Table 3.1 gives details of the eight opening Cases studied. The first Case is the 200 × 200 mm square opening in the wall of the FSTE. Figure 3.9 shows the seven other opening attachments cut from 6 mm thick 250 × 250 mm Perspex and plywood sheets that were attached to the 200 × 200 mm opening with fasteners and adhesive tape.

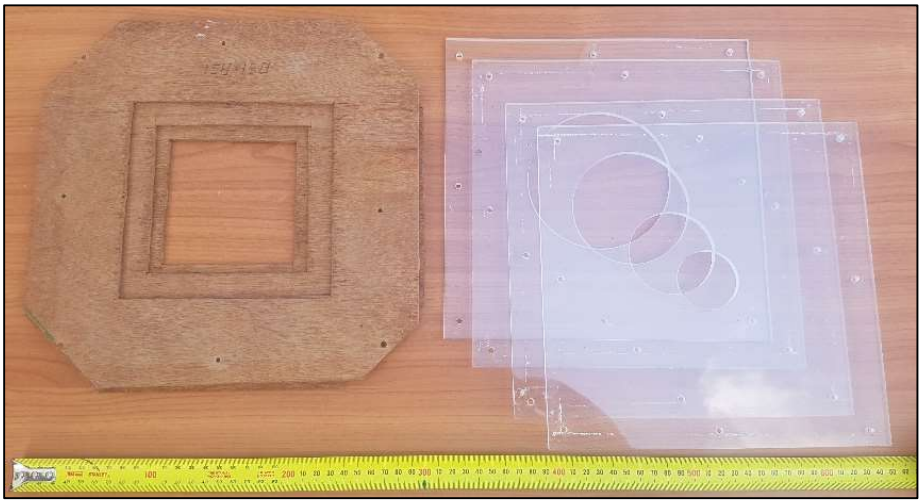

Figure 3.9. Opening attachments – Cases 2 to 8

The influence of the small opening areas relative to the size of the eddies in the approach wind flow is described by $\phi_5 = \lambda_u/\sqrt{A}$. ϕ_5 values for a full-scale low-rise building would typically range between 20 and 80 for an open door or window but can be very large for a small opening in a building. The ϕ_5 values examined in these test Cases were large thus produced well correlated external pressures across the opening. Smaller ϕ_5 values result in less correlated external pressures across the opening.

The ratio of the opening area to the building volume is described by $\phi_1 = A^{3/2}/V$. The ϕ_1 values examined on the FSTE were between 1.8×10^{-6} and 2.22×10^{-4}. These are within the range of typical low-rise building ϕ_1 values which range from 2.0×10^{-6} to 0.8. For very large buildings with single large openings, ϕ_1 may be less than 2.0×10^{-6} if the volume is well sealed.

Table 3.1. FSTE Opening Configuration details

Case #	Opening Dimensions	Opening Area ($\times 10^{-3}\ m^2$)	$\phi_1 = A^{3/2}/V$ ($\times 10^{-6}$)	$\phi_5 = \lambda_u/\sqrt{A}$
1	200×200 mm	40	222	500
2	158×158 mm	20	110	633
3	120×120 mm	14.4	48	833
4	100×100 mm	10	28	1000
5	113 mm dia.	10	28	1000
6	90 mm dia.	6.36	14	1250
7	65 mm dia.	3.32	5.3	1740
8	45 mm dia.	1.59	1.8	2510

Statistical stationarity of wind speed and angle was achieved by employing the "Run test" and "Trend test" methods. These methods were used in full-scale testing of the TTU WERFL building by Levitan and Mehta (1992). The Run and Trend test was applied to the mean and mean-square values of the sequence of ten 1-minute intervals for each 10-minute signal. Thus, four tests were performed for each time-history signal. If any of the four tests yielded a trend greater than a 0.05 confidence level, then the record was deemed non-stationary. In addition, 1-minute stationary signals were extracted from the 10-minutes signals through visual inspection to obtain a greater quantity of reliable test data.

Only wind angles approaching from $\theta = 0° \pm 30°$ (i.e. while openings are windward) with a mean wind speed greater than 1.5 m/s were considered for analysis. Due to the variation of the mean wind angle between each run, the mean and peak pressures have significant variations. Thus, the wind-induced pressures have not been assessed in terms of the mean approach wind speed, (i.e. pressure coefficients), as the range of values produced may be miss-construed due to the range of mean wind angles within $\bar{\theta} = 0° \pm 30°$. Internal pressures are analysed with respect to the external pressures applied to the openings.

Further, pressures were recorded at relatively low wind speeds compared to severe windstorms, it is acknowledged this increases uncertainties in results, however, meaningful internal to external pressure relationships are still derived, presented, and discussed in the following section.

3.2. Results and Discussion

The investigation was focused on stationary winds approaching towards the FSTE opening, generating positive external pressure on the windward opening. Data blocks that achieved mean external pressure greater than 2.5 Pa and a maximum external pressure greater than 10 Pa were selected for analysis to enable reliable data. This produced 643 1-minute data blocks. The range of mean wind speeds and the number of data blocks that satisfy these conditions for each Case is listed in Table 3.2. Each Case was divided into their own mean S* group considering the variability of the wind conditions and the range of wind speeds captured for each Case.

Table 3.2. Opening Configuration wind speed and S* details

Case #	Mean wind speed, m/s			S*	Number of one-minute blocks
	Minimum	Mean	Maximum		
1	2.20	2.37	4.08	4.6	38
2	1.52	1.55	3.15	5.8	56
3	1.60	1.7	2.55	1.9	35
4	1.50	1.57	3.78	1.3	158
5	1.74	1.91	2.53	0.88	17
6	1.50	1.51	2.10	0.75	22
7	1.51	1.80	3.44	0.19	22
8	1.51	1.84	3.60	0.06	295

Figures 3.10 to 3.13 shows 10 seconds of typical $p_e(t)$, $p_i(t)$, and $p_{net}(t)$ time-series measured for Cases 1, 3, 6, and 8. Figures 3.10 to 3.13 shows the internal pressure follows the external pressure fluctuations for all four Cases, with the mean net pressure across the opening fluctuating about 0 Pa. Cases 1 and 3 show the maximum internal pressure $\hat{p}_i$ exceeded the maximum external pressures $\hat{p}_e$, whilst for Cases 6 and 8, $p_i(t)$ lagged $p_e(t)$ due to restricted flow through the smaller openings.

Sharma and Richards (2004) noted that the true driving force for the internal pressure is the spatially-averaged external pressure at the opening cannot be measured with the opening present. However, the external pressure acting at the opening can be estimated by averaging the pressure acting at the four taps around the opening. This spatially averaged pressure is an acceptable representation of the pressure on the opening, especially for the size of the openings tested here related to the size of eddies in the approach flow ($\lambda_u \cong 100$ m).

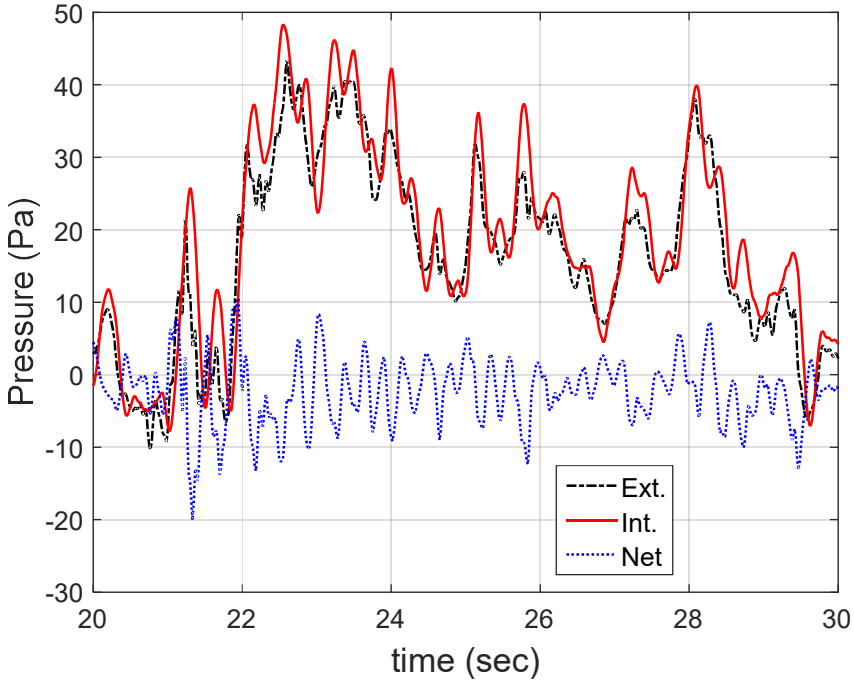

Figure 3.10. Typical external, internal, and net pressure time series: Case 1

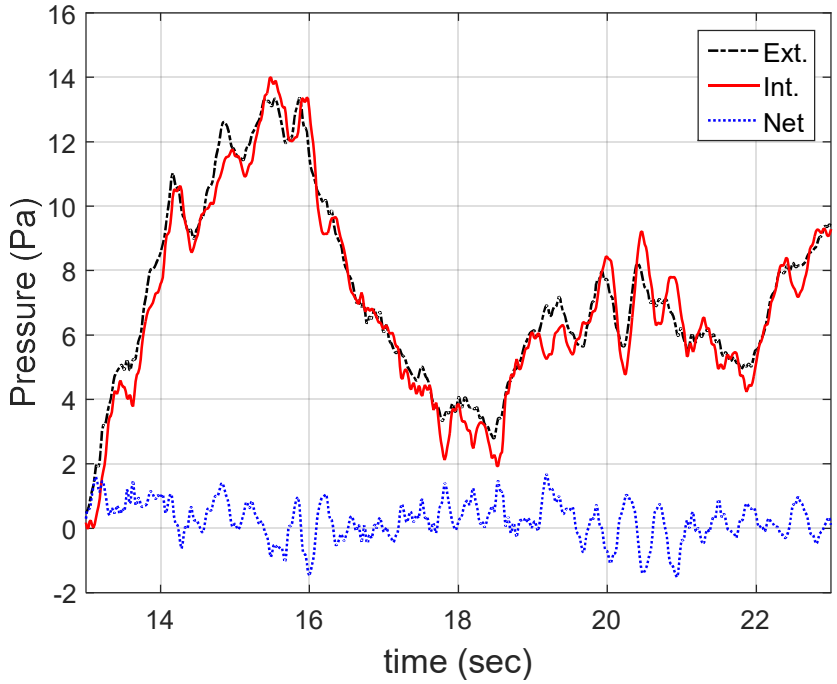

Figure 3.11. Typical external, internal, and net pressure time series: Case 3

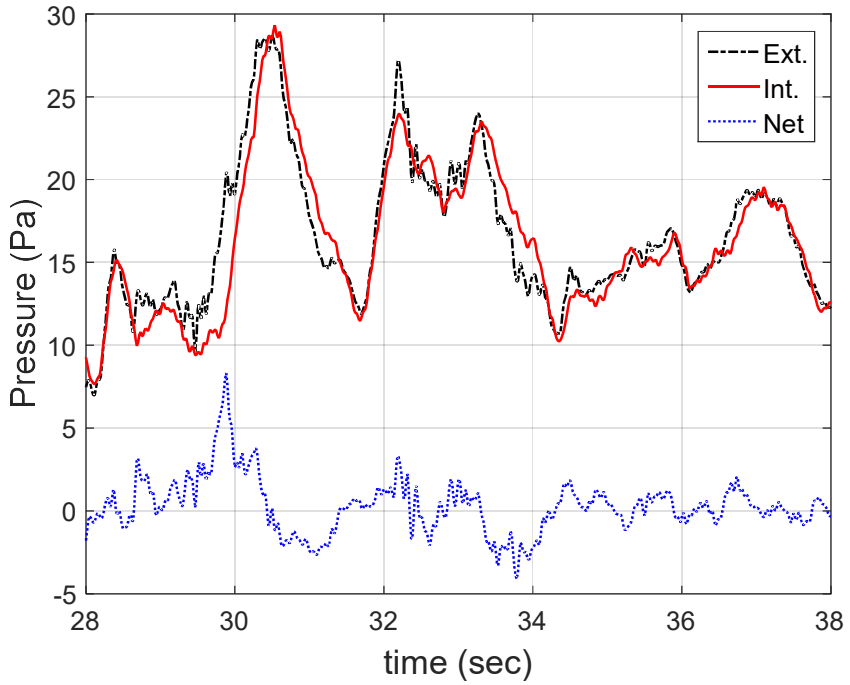

Figure 3.12. Typical external, internal, and net pressure time series: Case 6

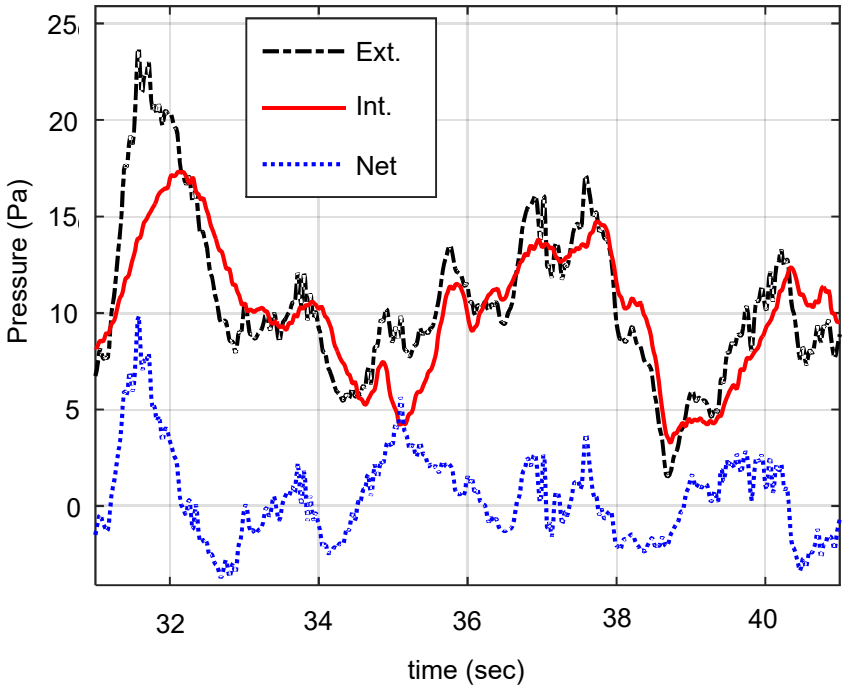

Figure 3.13. Typical external, internal, and net pressure time series: Case 8

3.2.1. Simulated Internal Pressure

The fluctuating windward wall external pressure time-series $p_{e,w}(t)$ from each test was used to generate a simulated internal pressure signal, $p_{i,sim}(t)$, using the method described in Section 2.4.1 where the input parameters $p_{e,w}(t)$, A, V, C_I, and C_L are used in Equation 2.9. The first and second time derivatives of $p_{i,sim}(t)$ in Equation 2.9 were solved using the backwards finite-difference-method using the raw 60 Hz data with an increased frequency to 600Hz via interpolation. The backwards difference method with an increased frequency provided faster analysis than the central difference and forwards difference method with the same level of accuracy. Further details on the numerical methods are detailed in Appendix A.

Each Case was simulated independently using static loss and inertial coefficients C_L and C_I, to provide the best match with the measured internal pressure spectra. Figure 3.14 shows the mean

non-dimensional pressure spectra of the 1-minute measured external and internal fluctuations $fS_{Cpw}(f)$ and $fS_{Cpi}(f)$, and the non-dimensional spectra of the simulated internal pressure fluctuations $fS_{Cpi,sim}(f)$ for the Cases which experienced Helmholtz resonance (Cases 1 to 5). Table 3.3 gives the C_L and C_I values that generate the best matching simulated internal pressure spectra with the measured internal pressure spectra.

Table 3.3. Helmholtz frequency, loss and inertial coefficients that match the measured internal pressure spectra

Case #	S^*	f_H (Hz)	C_I	C_L
1	4.6	3.3	1.5	20
2	5.8	3.0	1.45	15.5
3	1.9	2.6	1.4	10.5
4	1.3	2.2	1.45	10.5
5	0.88	2.3	1.3	9.5

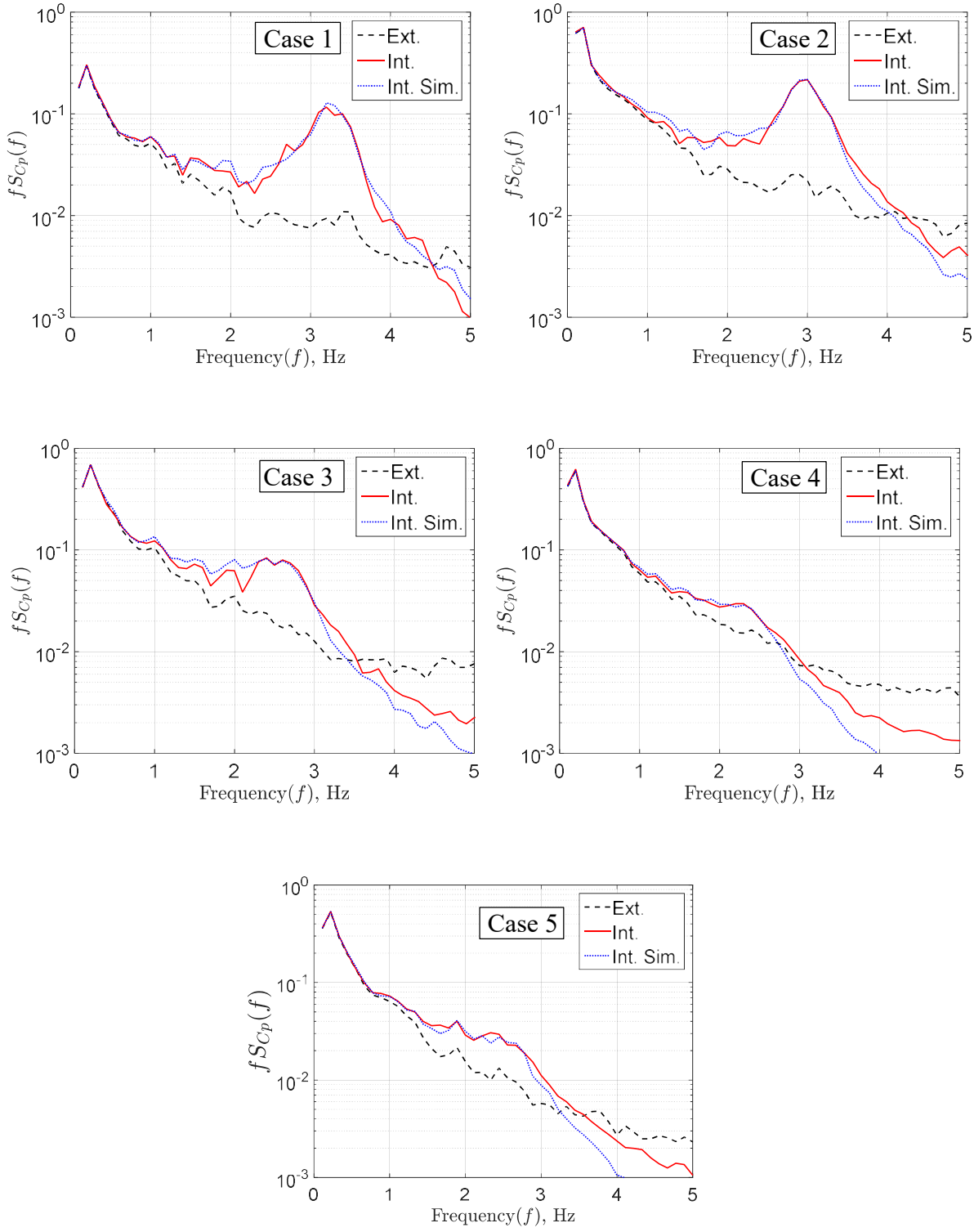

Figure 3.14. Non-dimensional measured external, internal, and simulated internal pressure spectra of Cases 1, 2, 3, 4, and 5

Table 3.3 shows that the inertial coefficient, C_I is between 1.3 to 1.5, which is within the range of C_I values derived from previous model-scale experiments, (i.e. Vickery and Bloxham (1992), Kim and Ginger (2013), and others). Table 3.3 also shows the loss coefficient increases with S* and is significantly larger than 2.78 which is used in classical potential flow analysis through an orifice. The increasing loss coefficient of between 10 to 20 with increasing $S^* = \left(A^{3/2}/V\right) \times (a_s/\overline{U}_h)^2$, is similar to model-scale findings by Holmes (1979), Ginger et al. (2010), Kim and Ginger (2013), Guha et al. (2013) and Xu et al. (2016, 2017). The results also show the opening shape has little influence on the loss coefficient as illustrated by Cases 4 and 5.

Comparison of C_L values derived from model-scale studies show the full-scale C_L values are smaller for the same S* range, $0.9 < S^* < 6$. Kim and Ginger (2013) showed C_L ranges between 8 to about 150, and Xu et al. (2016, 2017) showed C_L ranges between 8 to about 50, compared to 10 to 20 from the FSTE. This increase in loss coefficients for smaller-model scales was discussed by Sharma (2013) who assessed loss coefficients relative to *Re* for a range of length-scales from a simulated internal pressures analyse. Sharma suggested that the loss coefficient from model-scale studies are typically higher than full-scale as *Re* is smaller at model-scale, which correlates to an increase in the C_L values, detailed in Section 2.9.2.

Figure 3.15 a) and b) show the measured internal to external pressure admittance functions (i.e. transfer function) $\left|X_{i/e}(f)\right|^2 = S_{C_{pi}}(f)/S_{C_{pe}}(f)$ for Cases 1-5 and Cases 6-8 respectively. Figure 3.15 a) shows $\left|X_{i/e}(f)\right|^2$ for Cases 1 to 5 increases from unity to their maximums at f_H before attenuation at higher frequencies. Both f_H and magnitude of amplification $\left|X_{i/e}(f_H)\right|^2$ increase (i.e. tendency for resonance increases) as the opening area increases (S* increases). Figure 3.15 b) shows $\left|X_{i/e}(f)\right|^2$ for Cases 6 to 8 decreases from unity as frequency increases, indicating the decreasing the open area (decreasing S*) increases damping, inhibiting resonance for $S^* < 0.75$.

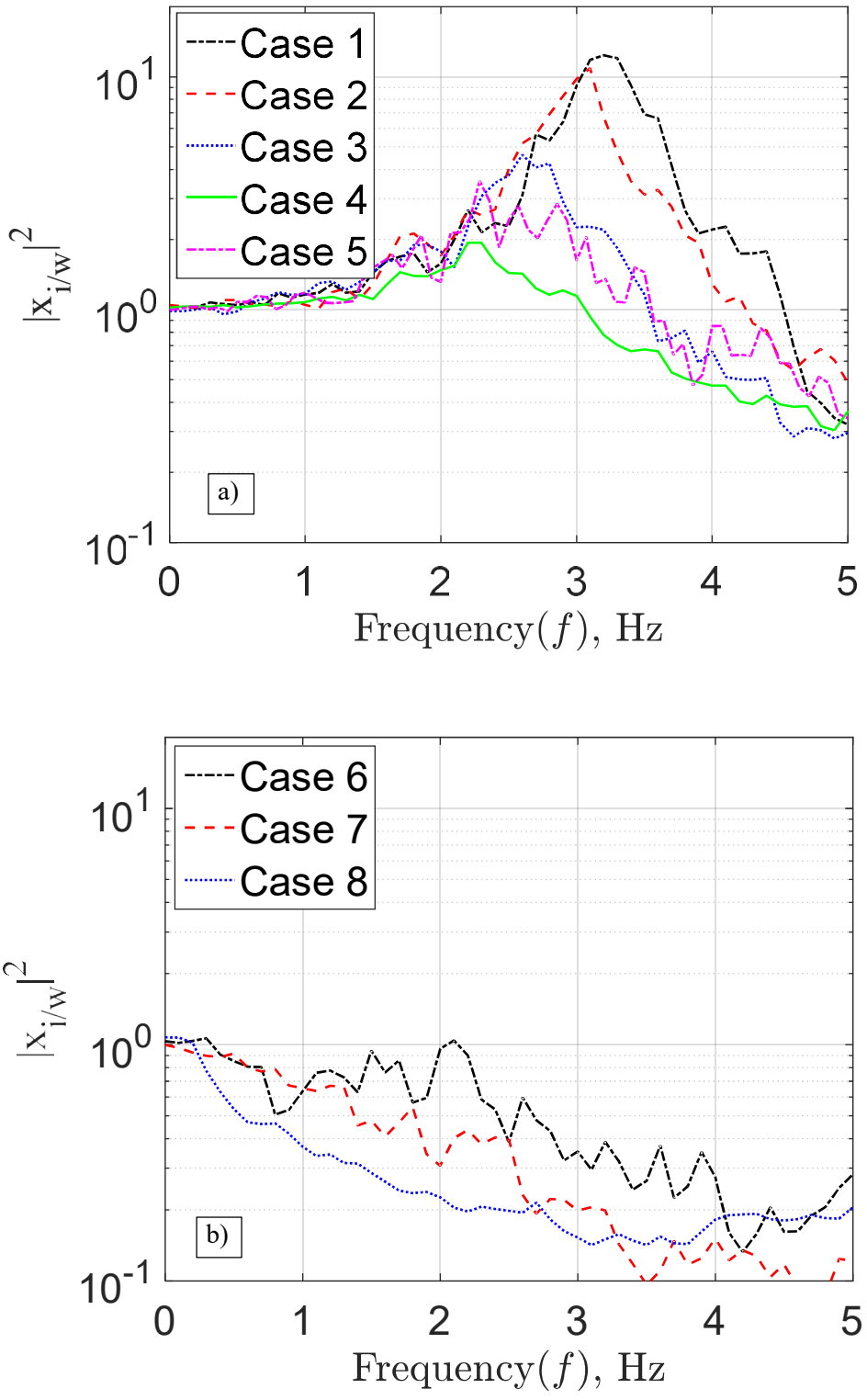

Figure 3.15. Admittance functions – a) Cases 1-5 and b) Cases 6-8

3.2.2. Ratio of Internal to External Pressures

The influence of resonance and attenuation of internal pressure fluctuations is assessed with respect to the ratio between internal and external pressures (mean, standard deviation, and peak pressures) and S*. Table 3.4 shows the mean, standard deviation, and maximum pressure ratios ($\bar{p}_i/\bar{p}_{e,w}$, $\sigma_{pi}/\sigma_{pe,w}$, and $\hat{p}_i/\hat{p}_{e,w}$) averaged across the total number of runs for each Case with S*. Table 3.4 shows that $\bar{p}_i/\bar{p}_{e,w}$ is approximately 1.0 for all Cases, which satisfies the continuity equation when there is a single opening in the envelope. Table 3.4 also shows that $\sigma_{pi}/\sigma_{pe,w}$, and $\hat{p}_i/\hat{p}_{e,w}$ are not equal to $\bar{p}_i/\bar{p}_{e,w}$, indicating that the quasi-static approximation may not be an satisfactory method to predict internal pressure fluctuations for a single opening in a building.

Table 3.4. Internal to external pressure ratios

Case #	S*	$\bar{p}_i/\bar{p}_{e,w}$	$\sigma_{pi}/\sigma_{pe,w}$	$\hat{p}_i/\hat{p}_{e,w}$
1	4.6	0.98	1.03	1.05
2	5.8	1.00	1.01	1.04
3	1.9	0.96	1.00	1.04
4	1.3	0.95	1.00	0.99
5	0.88	1.00	1.01	1.01
6	0.75	0.97	0.99	0.96
7	0.19	0.93	0.98	0.90
8	0.06	0.97	1.00	0.92

Figures 3.16 and 3.17 show the maximum and standard deviation internal to external pressure ratios versus S* respectively. Figures 3.16 and 3.17 show a trend that internal pressure fluctuations are "equal to" or exceed external pressure fluctuations for S* ≥ 0.88 (Case 1 to Case 5) and that $\hat{p}_i/\hat{p}_{e,w}$ and $\sigma_{pi}/\sigma_{pe,w}$ increase with S*. This correlates with the results from Figure 3.14 that shows $\left|X_{i/e}(f_H)\right|^2$ increases with S* (for Case 1 to Case 5), indicating that amplification at Helmholtz frequency produces $\hat{p}_i/\hat{p}_{e,w}$ and $\sigma_{pi}/\sigma_{pe,w} \geq 1$.

Figures 3.16 and 3.17 also shows that for S* ≤ 0.75 (Case 6 to Case 8) the $\hat{p}_i/\hat{p}_{e,w}$ and $\sigma_{pi}/\sigma_{pe,w} < 1$. This also correlates with the admittance functions in Figure 3.14, where the internal pressure response is significantly damped, attenuating internal pressure fluctuations, resulting in $\hat{p}_i/\hat{p}_{e,w}$ and $\sigma_{pi}/\sigma_{pe,w} < 1$. Figure 3.17 shows $\sigma_{pi}/\sigma_{pe,w}$ is about 1 for all Cases but has a positive trend that shows $\sigma_{pi}/\sigma_{pe,w} < 1$ for S* < 0.9 and $\sigma_{pi}/\sigma_{pe,w} > 1$ for S* > 0.9.

Figures 3.16 shows that between S* = 0.75 and 1.9, $\hat{p}_i/\hat{p}_{e,w} \approx 1$ satisfying the quasi-static approximation for a single opening. Thus S* = 0.9 may be taken as the limiting condition for a dominant opening without envelope porosity when the internal pressure fluctuations approach the external pressure fluctuations in a sealed building with a single opening and large Φ_5 values.

These results show that as S* increases, the damping decreases, which increases the tendency for resonance once S* ≥ 0.9. However, it is also shown from Table 3.3 and previous model-scale studies that the loss coefficient C_L (which incorporates viscous losses) increases with S*, which successively limits the amplification of the resonant effects.

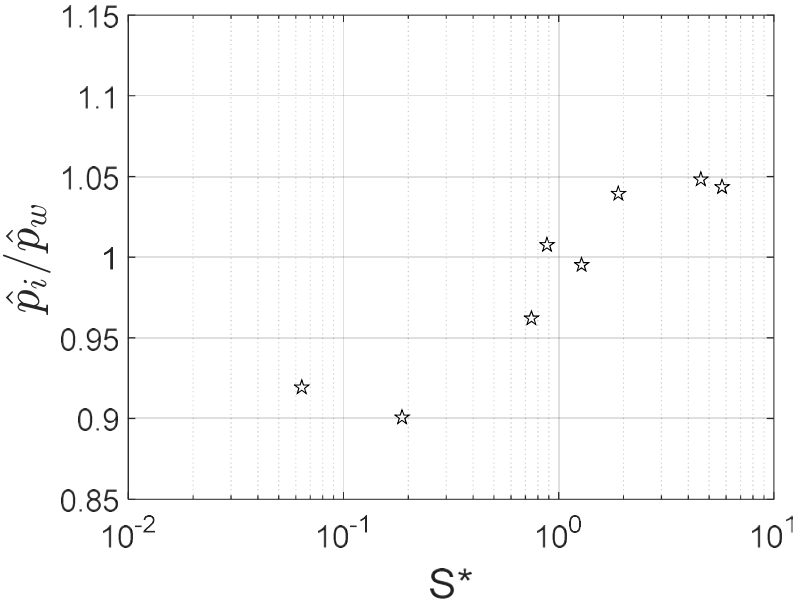

Figure 3.16. FSTE $\hat{p}_i/\hat{p}_{e,w}$ versus S*

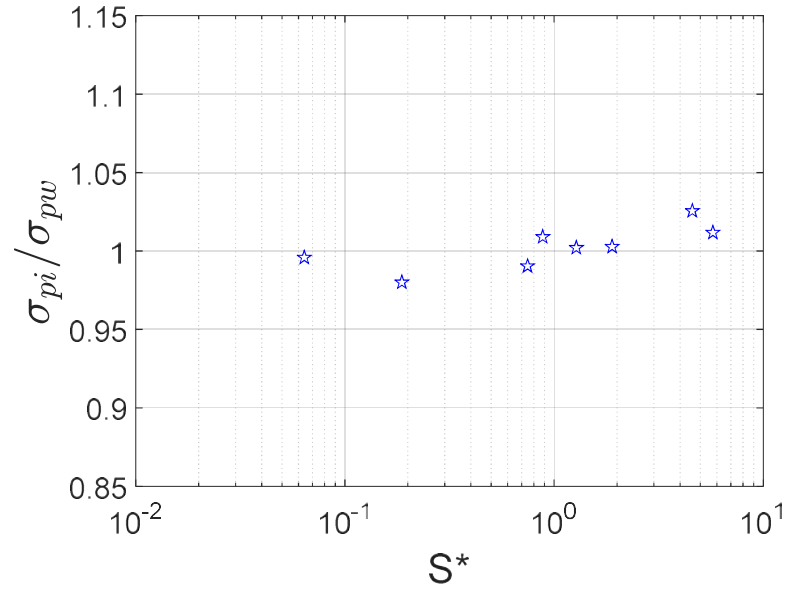

Figure 3.17. FSTE $\sigma_{pi}/\sigma_{pe,w}$ versus S*

Wind tunnel studies have shown that the ratio of the standard deviation of the internal to external pressure fluctuations $\sigma_{pi}/\sigma_{pe,w}$ is limited to about 1.1 under typical turbulence intensities and S* values. Figure 3.18 shows the FSTE $\sigma_{pi}/\sigma_{pe,w}$ results with a summary of model-scale results detailed by Holmes and Ginger (2012). Figure 3.18 shows the empirical formula derived by Holmes and Ginger (2012) for a typical Φ_5 value of 20 and a larger Φ_5 value of 80. Figure 3.18 shows the $\sigma_{pi}/\sigma_{pe,w}$ values from model-scale tests and the FSTE results as a function of S*. Figure 3.18 shows that $\sigma_{pi}/\sigma_{pe,w}$ is about 1 around S* = 0.9 for both model-scale and full-scale. However, the internal pressure fluctuations from the model-scale studies show a greater increase in internal pressure fluctuations with S* compared to the FSTE results. Figure 3.18 also shows that the empirical formula from Holmes and Ginger (2010) overestimated $\sigma_{pi}/\sigma_{pe,w}$ for large Φ_5 values, indicating the Φ_5 is not as critical as the S* value for calculation of internal pressure fluctuations.

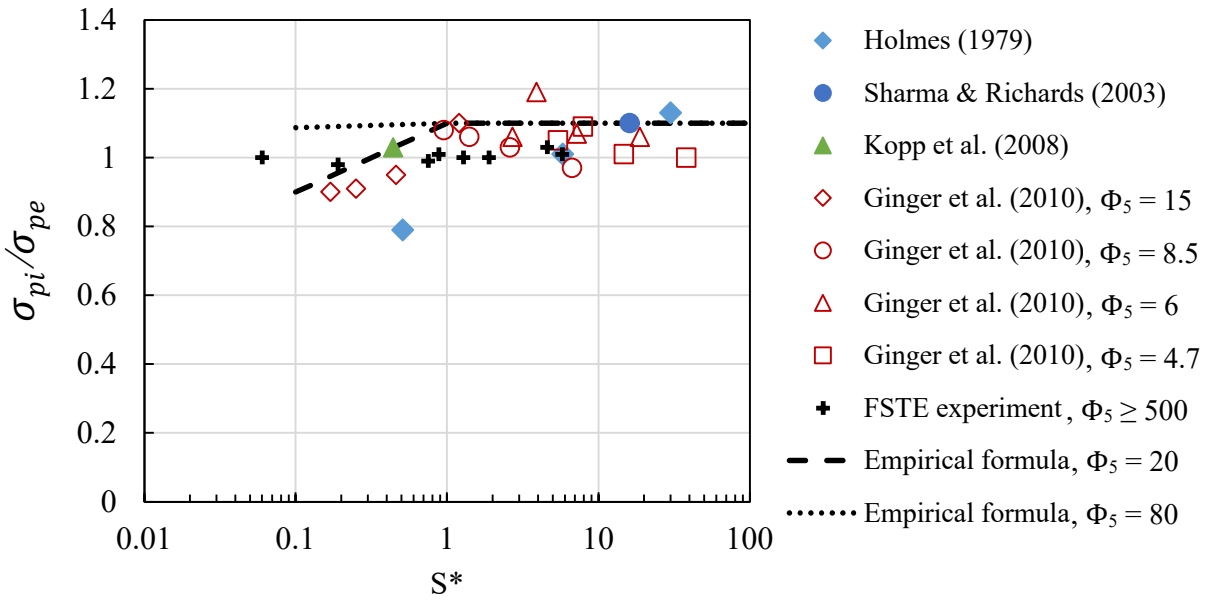

Figure 3.18. Internal to External standard deviation pressure versus S* with FSTE results – Holmes and Ginger (2010)

3.3. Summary and Conclusions

A controlled full-scale study was carried out to determine the internal pressure fluctuations in a sealed, Full-Scale Test Enclosure (FSTE) with a range of "single" windward wall opening configurations (Cases 1-8) when subjected to atmospheric wind flow. This unique full-scale study provides full-scale data to enable the assessment of previous analytical and model-scale studies.

This study defines loss and inertial coefficients from a full-scale environment for flow through a single building opening, where it is shown that as S* increases, damping decreases producing favourable conditions for Helmholtz resonance to occur and peak internal pressures to exceed peak external pressures. However, it is also shown that increasing S* reduced the differential pressure across the opening, decreasing the mean flow velocity and Re through the opening, and increases the viscous losses, described by an increasing value of C_L, greater than 2.78 from steady flow.

The results also show the threshold condition for the size of the building opening, volume, and approach wind speed (i.e. S* value) for peak internal pressures to approach the peak external pressure at the opening. This is an important result that confirms some preliminary findings from model-scale studies by Holmes (1979), Ginger et al. (2008), Kim and Ginger (2013), Guha et al. (2013), Xu et al. (2016,2017) and full-scale Ginger et al. (1997, 2000).

The study showed that:

1. The internal pressure follows the external pressure at the opening in all cases with the net pressure fluctuating about 0 Pa, where the mean internal pressure is close to the mean external pressure.
2. The fluctuating internal pressures are influenced by the opening area to volume parameter, S*. Helmholtz resonance is observed at Helmholtz frequency f_H when S* $\geq$ 0.9. Increasing the opening area (increasing S*) decreases damping, thus increasing the tendency for Helmholtz resonance. Increasing the opening area also increases the

effective length of the air-slug (i.e. $l_e = C_I\sqrt{A}$) increases the Helmholtz frequency as S* increases.

3. The loss coefficient C_L is also shown to be a function of S*. Values of C_L ranged from 10 to 20 for, S* between 0.88 and 5.8 respectively. These C_L values are much larger than 2.78 from the potential flow theory, similar to model-scale studies.
4. Inertial coefficients C_I between 1.3 and 1.5 are similar to values derived by previous model scale studies.
5. The peak and standard deviation internal pressures are amplified by about 5% for S* > 1.9 and attenuated by 5 to 10% for S* < 0.75. Internal pressure quasi-static approximation is satisfactory for S* ≅ 0.9 without background leakage.

Chapter 4 presents the second full-scale experimental test setup conducted on a typical industrial type building. Chapter 4 details unique air-leakage tests conducted to define the area of background leakage and envelope flexibility. The Chapter also analysis the internal pressures with respect to external pressure fluctuations around the envelope and compares results with other previous model-scale and full-scale tests.

CHAPTER 4: JAMES COOK UNIVERSITY – AUSTRALIAN STEEL INSTITUTE SHED

This Chapter presents the experimental setup, methodology, results, and discussion from testing a full-scale Industrial Building (i.e. Shed) with a range of opening configurations in the envelope under natural atmospheric wind flow. Measurement of porous open area around wall fitments and discontinuities in the envelope are also presented in addition to the measurement of envelope flexibility.

The full-scale test building is a steel-clad, cold-form, portal-framed shed, a common type of industrial building in Australia. A typical structural system of these types of buildings is shown in Figure 4.1. Wind loads (i.e. external and internal pressures) applied to the roof and wall cladding of the building is transferred to the foundations via the structural system; cladding is fastened to roof purlins and wall girts that span between rafters and columns, respectively. Moment resisting connections join the columns and rafters forming the "portal frame", allowing for open plan spaces devoid of internal columns or bracing. The columns and rafters are often either cold-formed or hot-rolled steel sections. Cold-formed sections are suited for smaller and lighter buildings, with rafter spans less than about 24 m and columns shorter than about 6 m, whereas hot-rolled sections are used for larger buildings that experience larger design loads.

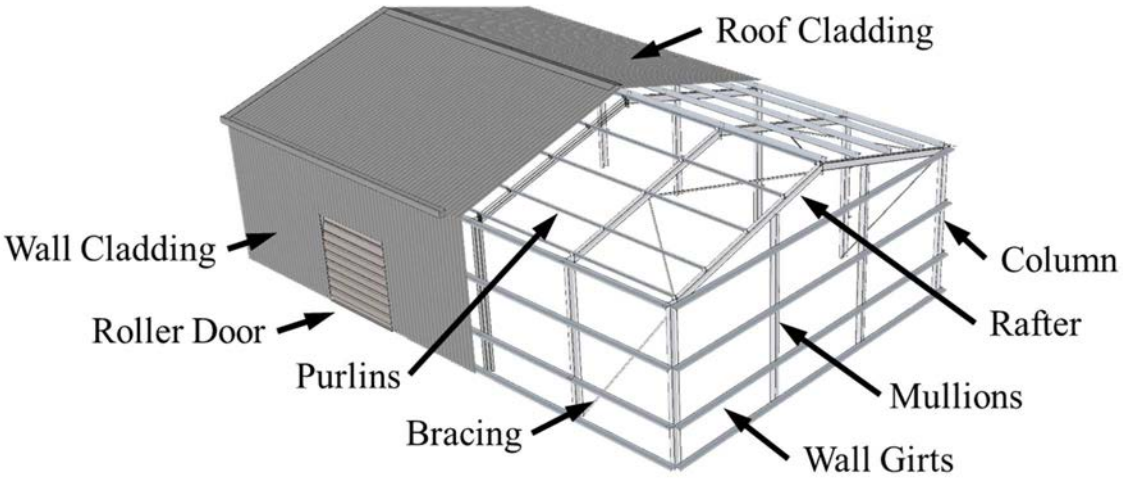

Figure 4.1. Schematic of a Steel-Clad, Portal-Frame, Industrial Building

Industrial type buildings usually have large access doors (e.g. roller shutter or curtain door) that span across wall columns or mullions. Post windstorm damage investigations have shown that large access doors are often unable to resist wind loads and debris impact during windstorms, creating large openings in the wall envelope, Henderson *et al.* (2006). Typical warehousing and manufacturing industrial type buildings are not well insulated, especially in tropical and temperate climates, thus envelope construction tolerances are not critical for climate control and consist of background leakage/porous openings at discontinuities in the envelope, e.g. around wall fitments (i.e. windows and doors) and under flashings. The American Society of Heating, Refrigerating, and Air-Conditioning Handbook, ASHRAE (2005), Chapter 26 on Ventilation and Infiltration notes that the porosity ε, (porous opening area relative to the total surface area ($\varepsilon = A_P/A_T$)), of a nominally sealed steel-clad wall is about 0.5%. However, the actual porosity can vary significantly, and can be much higher in tropical and temperate climates compared to cold climates, and is also dependent on the number of fitments, tolerances, and construction practice. In comparison, residential and office buildings may typically have a wall porosity between 0.01% and 0.2%, ASHRAE (2005).

4.1. Test Building Specifications

The Australian Steel Institute (ASI) donated a 6 × 6 × 3 m cold-form steel-clad shed with an 11° roof pitch to carry out the series of tests for this project. This test building is referred to as the James Cook University – Australian Steel Institute Shed (JCU-ASIS) and is shown in Figure 4.2. The JCU-ASIS is a small to moderate size cold-form portal-framed industrial building with typical construction details and tolerances with an internal volume of 119 m^3. The outcomes from this study apply to smaller sheds (i.e. smaller than the JCU-ASIS) to larger industrial buildings, with dimensions ranging to about 20 × 40 × 6 m, that have similar construction details, as results are presented in a non-dimensional form.

The JCU-ASIS is constructed on a 6 × 6 m concrete slab with three portal-frames spaced 3 m apart, fabricated from C15019 cold-form "Cee" sections (152 mm deep, 1.9 BMT) and bolted gusset plates. 0.42 BMT Trimdek® cladding is fixed to Z10015 cold-form "Zed" purlins and wall girts (102 mm × 1.5 BMT). Sheets of air-cell insulation were laid across the roof purlins before the Trimdek roof cladding was installed. Additional details regarding the JCU-ASIS construction and materials are given in Appendix C.

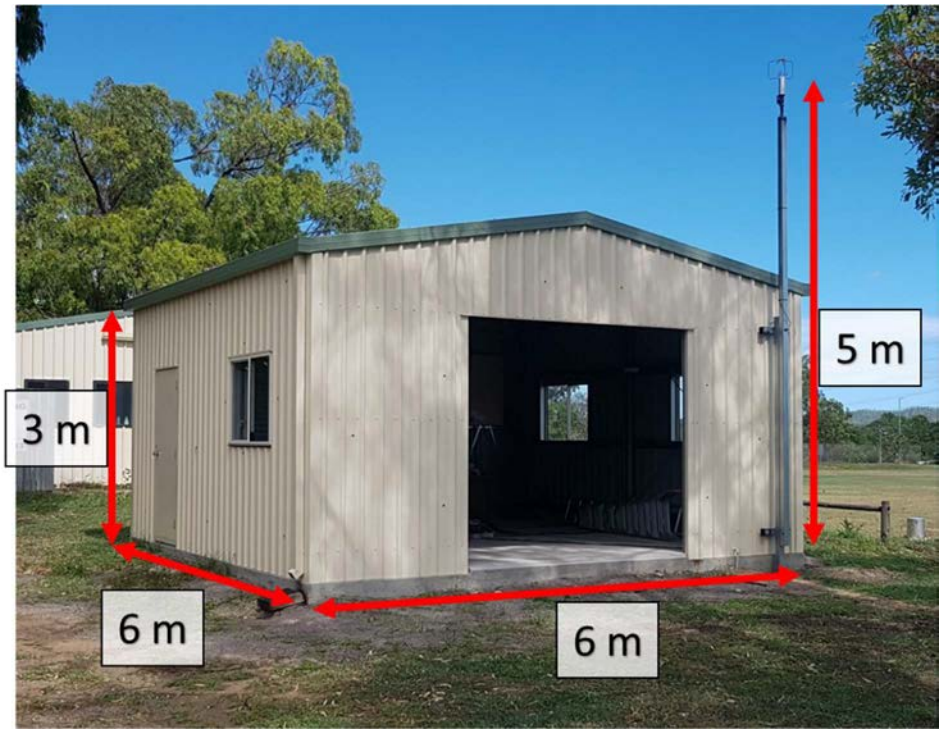

Figure 4.2. James Cook University – Australian Steel Institute Shed (JCU-ASIS) with roller door open on Eastern Wall. Sonic anemometer attached to 5 m mast at NE edge

4.2. Experimental Details

The JCU-ASIS is located between two adjoining sports fields at James Cook University, about 10.5 km from the coast in Townsville, Australia. Figure 4.3 is an aerial image of approximately 400 m around the site, showing the orientation of the shed relative to the wind approach angle, θ where θ = 0° and 90° are winds blowing towards the North and East walls of the Shed respectively. The photograph in Figure 4.2 was taken from θ ≅ 120°. Figure 4.3 also shows the reference pressure pit located 20 m to the East of the JCU-ASIS and open terrain to the Northwest through to the East and South-Southeast to South-Southwest. An adjoining shed situated 10 m to the West, shown behind the JCU-ASIS in Figure 4.2, disturbs the wind flow

from the West, thus winds from the West (θ = 220° – 320°) are not considered in this study. Strong winds are typically experienced from the Northeast to East and Southerly directions.

Figure 4.3. Arial image of JCU-ASIS and surroundings, North ≈ θ = 0°

4.2.1. Wall Fitments

Figure 4.4 shows the schematic layout of the JCU-ASIS, its fitments and pressure tap layout. The fitments include two roller doors, three sliding windows, and a personnel access door. These fitments installed in the envelope allow a range of opening configurations to be set up for testing. The doors and windows are opened and closed to enable a range of wall openings to be studied. Table 4.1 specifies the window and door opening dimensions and areas and their

proportion to the wall area. The inclusion of a wall fitment will tend to increase porosity in the envelope, influencing the internal pressure.

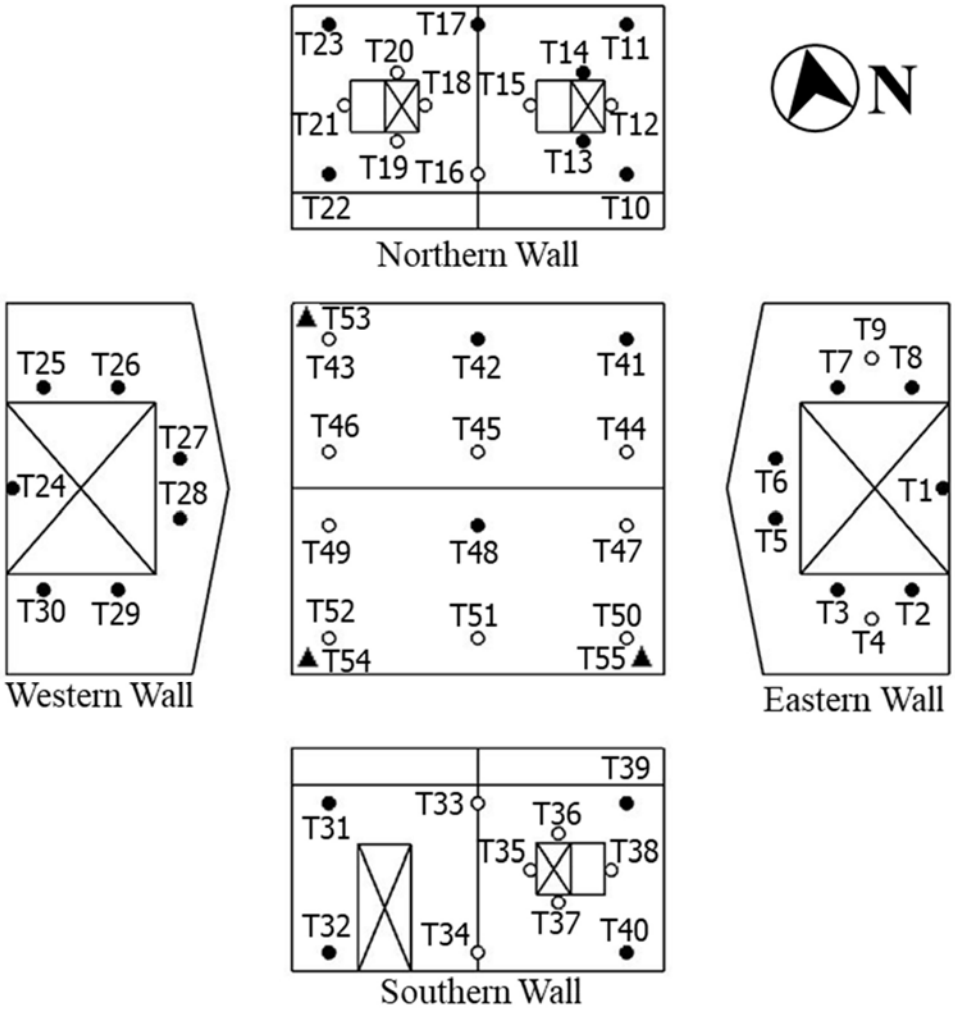

Figure 4.4. Schematic of JCU-ASIS wall fitments and pressure tap layout; Circles – external taps; Triangles – internal taps; Solid – instrumented; Hollow – not instrumented

Table 4.1. JCU-ASIS Wall Fitment Details

Opening	Dimensions	Open Area	Percentage of Wall
Roller Doors	2.4 m × 2.76 m	6.62 m2	33.5%
Personnel Access Door	2.04 m × 0.85 m	1.73 m2	9.61%
Sliding Window	0.55 m × 0.83 m	0.457 m2	2.54%

4.2.2. Porous Openings

The level of porosity in the envelope of a building is difficult to quantify as the gaps around fitments and construction tolerances depend on installation and construction practice, and cannot be easily measured. Porosity can be determined in an overall sense by conducting air-leakage tests (ASTM (2003), ASHRAE (2005)) as detailed in Section 4.3. The level of porosity may have a significant influence on the internal pressure fluctuations, hence must be satisfactorily estimated to optimise the design of these types of buildings.

4.2.3. Pressure Tap Locations

Fifty-two external surface pressure taps were installed on the JCU-ASIS; twenty-eight of these were connected to pressure transducers, and three additional pressure transducers measured the internal pressure. The location of the pressure taps are shown in Figure 4.4, where the solid circles are instrumented external pressure taps, hollow circles are un-instrumented external pressure taps, and solid triangles are the instrumented internal pressure taps. Figure 4.5 details the locations of the external pressure taps from edges and wall fitments, where roof taps are 600 mm from the eaves and/or ridgeline.

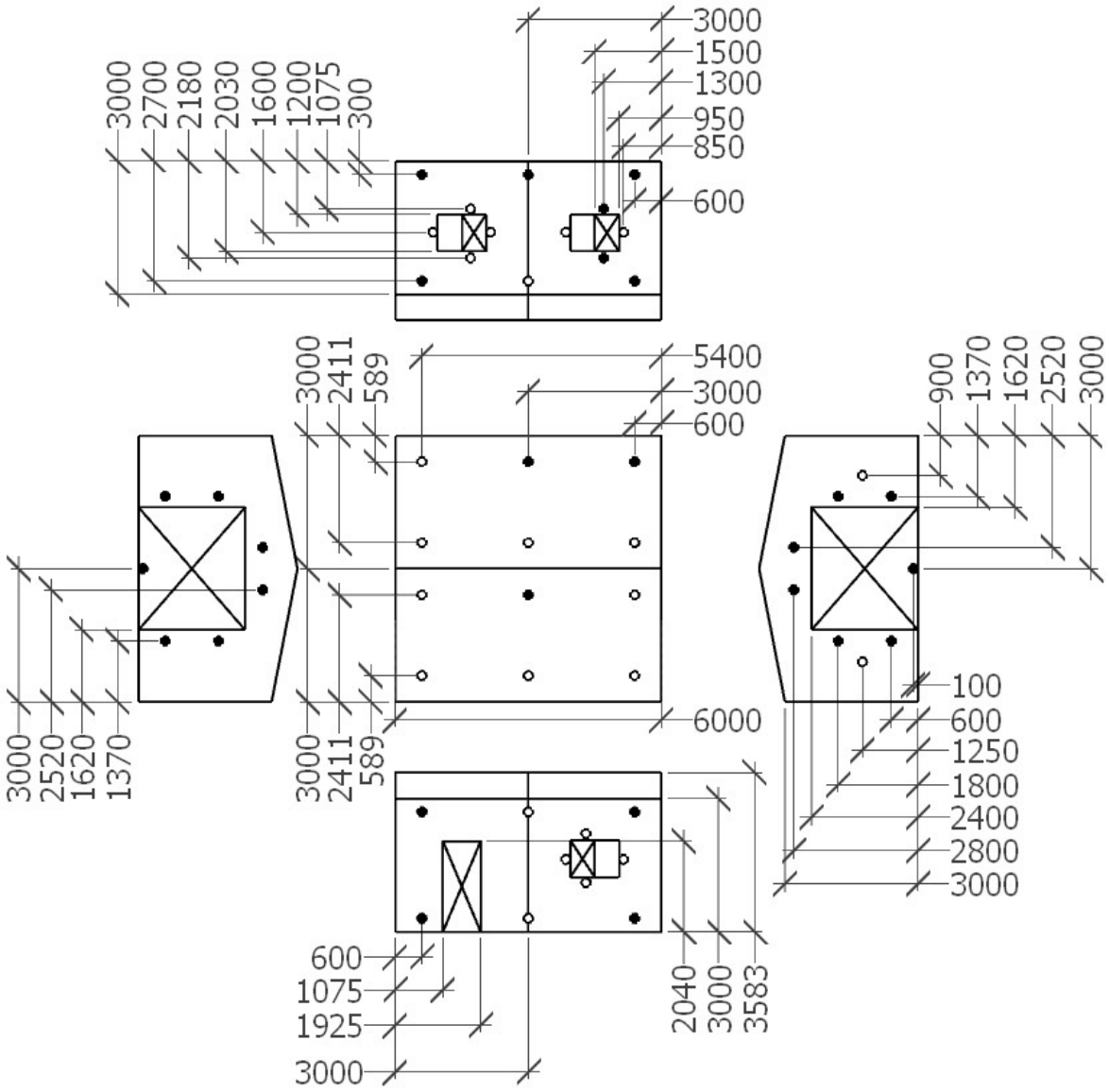

Figure 4.5. JCU-ASIS external pressure tap schematic (all dimensions in mm)

4.2.4. Pressure Transducers

The thirty-one pressure transducers and data acquisition system used for the JCU-ASIS were the same as those used for the FSTE tests, as described in Chapter 3. Each test captured data at 60 Hz for 10-minutes, which was post-processed to 15 Hz with a moving average filter. The reference pressure for the pressure measurements was obtained from an underground reference pressure pit (0.6 m long × 0.4 m wide × 0.6 m deep), located 20 m to the East of the JCU-ASIS and connected by a length of 4 mm inner diameter tubing that damps short pressure fluctuations. Similar to the FSTE tests, the pressure transducer casements were connected to the pressure taps via a 200 mm length of 10 mm inner diameter tubing. The pressure transducers were zeroed for the initial 5 seconds of each test by activating the solenoid valve in the casement. Figure 4.6 shows a pressure transducer and solenoid housing for a wall and roof pressure tap.

Figure 4.6. Pressure transducers connected to wall tap T7 (left) and roof tap T42 (Right)

As these pressure taps were on the external surface, they were exposed rain and other blockages such as insect nests; they were inspected and cleaned regularly. Single-ended ½ inch barbed brass hose fittings were used as pressure taps to minimise rainwater ingress. The fittings were installed on the rib of the roof cladding and pan of the wall cladding, as shown in Figure 4.7. The taps protrude 5 mm from the surface minimising rainwater runoff into the taps, and the ½-inch size prevents the water from blocking the tap or tubing. A T-intersection with a short length of tubing was added between the roof pressure taps and transducer housings on the inside of the building to collect any water that entered the tap to prevent it from blocking the tubing, as shown in Figure 4.6. In addition, assessment of the time history data from each pressure tap was conducted as a quality assurance measure of the signals, which also identifies faulty or blocked pressure taps. Visual assessment of pressure time-history signals was also carried out.

Figure 4.7. Un-instrumented pressure tap from building exterior (left) and interior (right)

4.2.5. Anemometer

An ultrasonic anemometer (R.M. Young Model 81005A) was installed atop a 5 m tall steel mast at the Northern edge of the Eastern wall of the JCU-ASIS, as shown in Figure 4.8 (also in Figure 4.2). The ultrasonic anemometer captured wind speed and wind approach angle time history

data simultaneously, with the measurements at 20 Hz, which is then post-processed to 5 Hz with a moving average filter.

The integral-time scale of turbulence of the approach flow is defined as the duration of positive correlation of velocity fluctuations obtained by the integration of the auto-correlation function. The integral length-scale of turbulence λ_u is considered equivalent to the integral-time scale of turbulence multiplied by the mean wind speed. This produced λ_u within the range of 20 m to 120 m, with a mean value of about 35 m during the range of tests from the East-North-East (θ = 60°-90°) with a turbulence intensity at the measurement height of approximately 30%. The normalised wind velocity power spectral density $(fS_u(f)/\lambda_u)$ is shown in

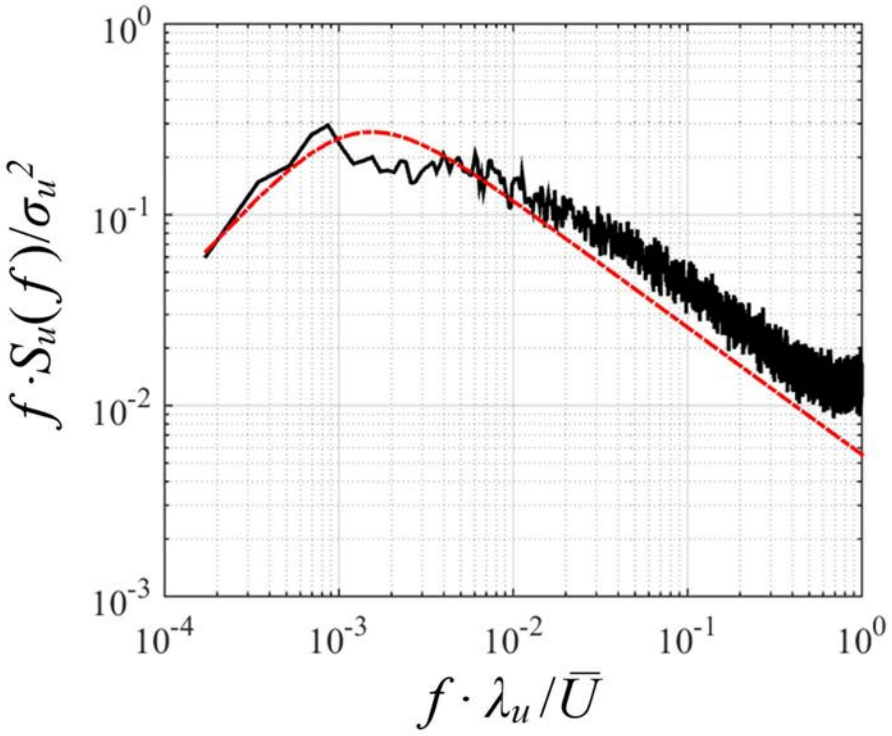

Figure 4.9, which shows a close match with the normalised von Karman model. An adjustment factor of 0.85 was applied to the velocity measurements to adjust the wind speeds to a 3m roof height. The 0.85 reduction factor was derived from the atmospheric boundary layer logarithmic law-model for Iuu = 30%. Appendix B provides further information on the ultrasonic anemometer details.

Figure 4.8. R.M. Young Ultrasonic anemometer on 5 m tall mast

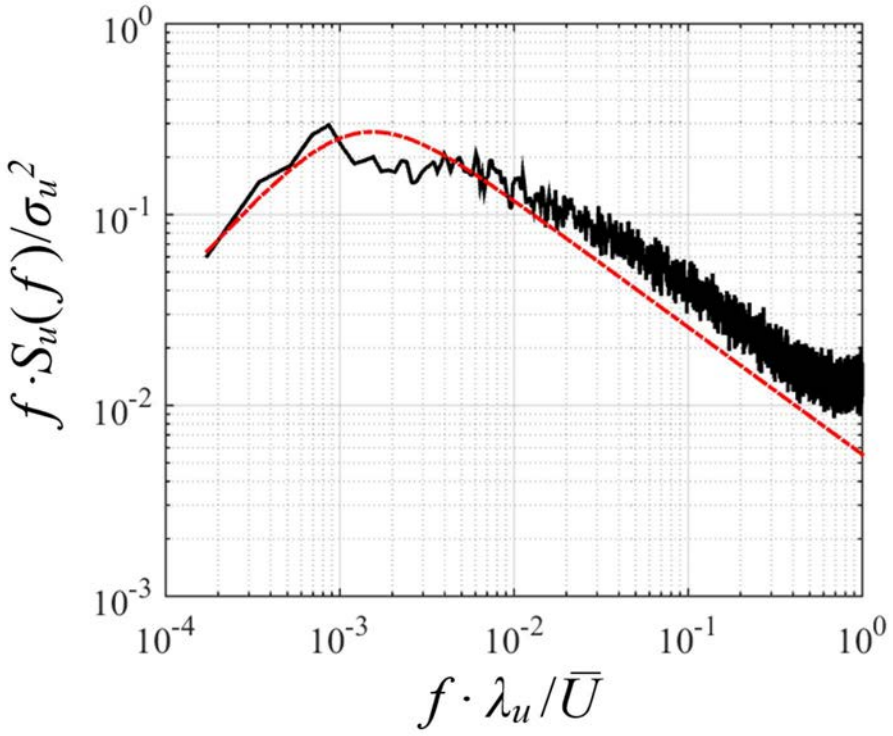

Figure 4.9. Normalized spectrum of the wind velocity – Solid line: Measured at 5 m elevation; Dashed line: von-Karman model

4.3. Air-Leakage Testing

Air-leakage testing was undertaken on the JCU-ASIS to quantify the area of background leakage (i.e. porous openings) in the envelope, that were otherwise difficult to accurately define. These tests were done by inducing a steady differential pressure across the envelope, $\Delta\bar{p}$, by pumping air into the building and recording the steady-state flow-rate, $\bar{Q}$ required to maintain $\Delta\bar{p}$ across the building envelope. Testing was carried out over a range of flow-rates and pressures to characterise the flow through the envelope.

Section 2.3.1 details the power law that is used to describe the relationship between the air-leakage flow rate $\bar{Q}$ and differential pressure $\Delta\bar{p}$. The power-law is given in Equation 2.6, as $\bar{Q} = C(\Delta\bar{p})^n$, where C and n are an empirical flow coefficient and flow-exponent respectively. The British Standard for the testing of the air permeability of buildings, BN/EN 13829 (2001) recommends an unweighted log-linearized linear regression technique to calculate the flow-exponent *n* and flow coefficient *C* from the $\bar{Q}$ and $\Delta\bar{p}$ measurements and is detailed in Appendix D.

The aim of the air-leakage testing on the JCU-ASIS was to identify the types of porosity and determine the area of these openings in the nominally sealed envelope. Typical openings in a nominally sealed industrial type building include the gaps between the floor slab and the wall cladding, between the wall cladding and roof cladding junctions, beneath the ridgeline capping, external wall junctions, around the perimeter of window and door fitments, through porous doors (i.e. roller shutters), roller door tracks, laps in cladding, etc.

A series of air-leakage tests were conducted to quantify the magnitude of the open area of each of the elements that contribute to background leakage of the nominally sealed JCU-ASIS envelope. A "baseline" air-leakage test was carried out by sealing gaps (porous openings) as much as practicable with caulking silicon, adhesive tape, and/or blocks of foam densely packed into openings, as shown in Figure 4.10. This initial air-leakage test was the baseline for the air-leakage tests that followed. Air-leakage tests were then carried out by progressively removing the seals from select parts of the envelope. The sequence of removing seals from the construction gaps was followed by an air-leakage test and repeated until all porous openings were unsealed and tested.

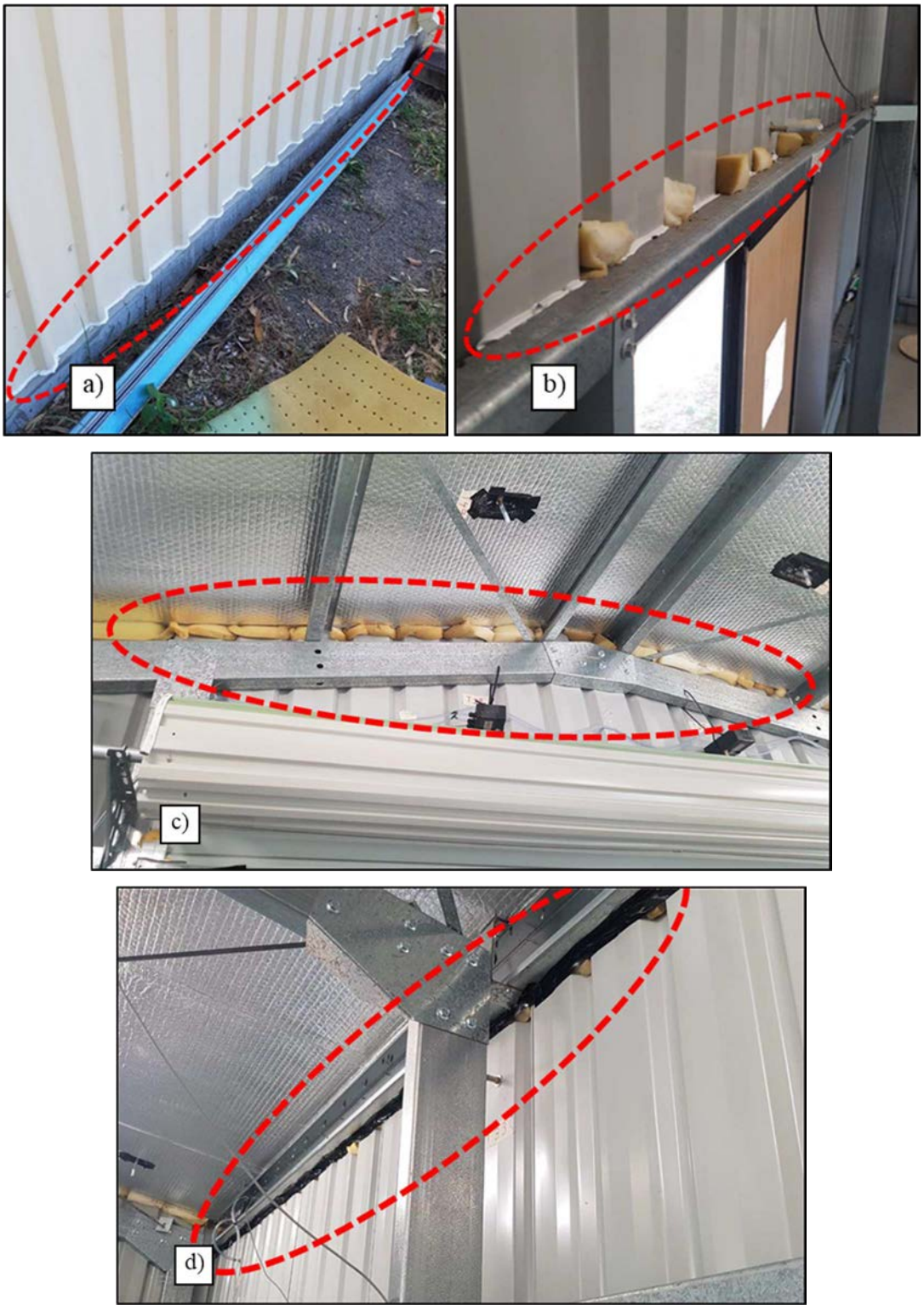
a)
b)
c)
d)

Figure 4.10. Sealed porous openings on the "Baseline" building, (a) Silicon around perimeter of floor slab (b) Silicon and foam above windows/doors (c) Foam blocks compressed into gable-end roof (d) Adhesive tape and foam under eave strut

In addition, a series of air-leakage tests were conducted on the Baseline Building with a range of defined circular openings installed in a sealed plywood window fitment. The change in flow-rate after adding the known openings into the envelope was used as validation of the Power law (Equation 2.6) relationship with the steady discharge Equation 2.7.

4.3.1. Air-Leakage Test Equipment

Air-leakage tests were carried out using a 7.5 m^3/min Air Handler Unit accompanied by a 30-kVA generator supplied by Kaltec Services Pty Ltd, shown in Figure 4.11. The roller door on the Eastern wall of the JCU-ASIS was opened and an impermeable plywood barrier with two circular openings was installed. All openings around the barrier and doorframe were then sealed (i.e. joints, flashings and the rain divider above the door). Flexible ducting connected the air-handler to the building through two 495 mm inner diameter flanged wall to duct connectors protruding from the plywood wall, to pump air from the air-handler into the JCU-ASIS.

In addition, precision NATA accredited airflow velocity equipment; Dwyer model 160G Averaging Air-Flow Grid and hot-wire probe, shown in Figure 4.12, were used to measure the steady flow-rate through the two ducts at the flanged wall to duct connection cross-sections. The flowrate through the ducts was calculated from the area-averaged velocity through the ducts. The measurements from the hot-wire probe matched the air-flow grid, thus the air-flow grid was utilized for all measurements as it required fewer measurements.

The air-flow grid had an averaging period of 4 seconds and can accurately measure velocities up to 12.5±0.1 m/s, per duct, equivalent to 4.8±0.04 m^3/s (17,300 ±140 m^3/hr) into the building.

Figure 4.11. Air Handler Unit and flexible ducting attached to the JCU-ASIS via the plywood barrier

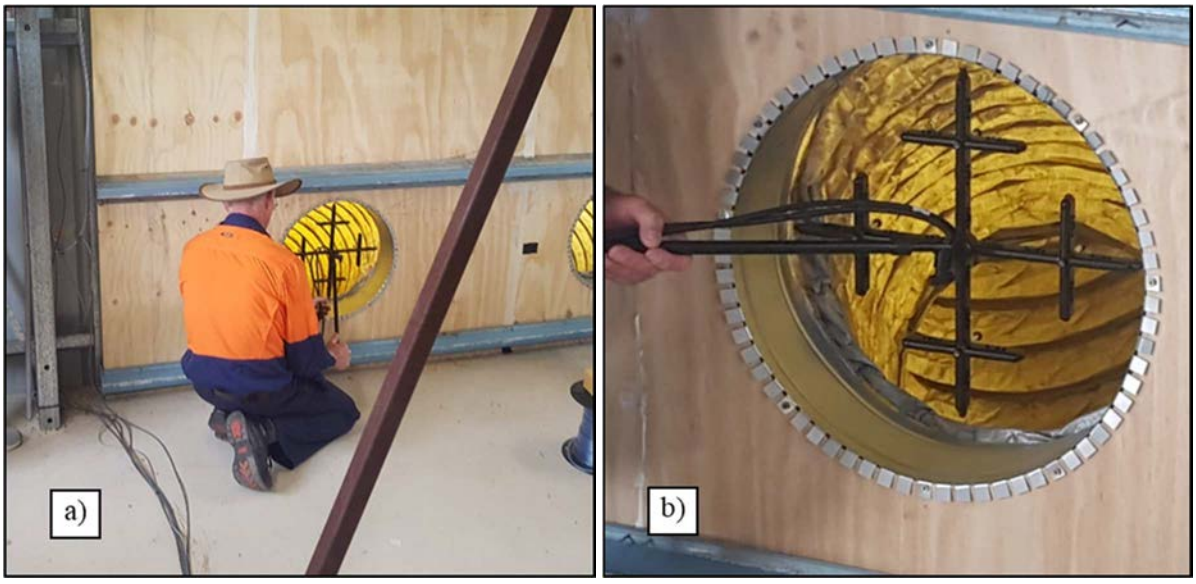

Figure 4.12. (a) and (b) Measurement of air flow-rate during an air-leakage test with the averaging airflow grid

4.3.2. Air-Leakage Testing – Defined Openings

A series of air leakage tests were carried out with five circular openings installed in the envelope with diameters of 65 mm, 90 mm, 113 mm, 135 mm, and 178 mm cut from 6 mm thick 250 mm × 250 mm Perspex sheets. The Perspex sheets were attached to a plywood frame that replaced a sliding window, as shown in Figure 4.13. The five openings were installed and tested after the sealed JCU-ASIS (i.e. Baseline Building) was tested and seals around the Personnel Access (PA) door were removed and tested.

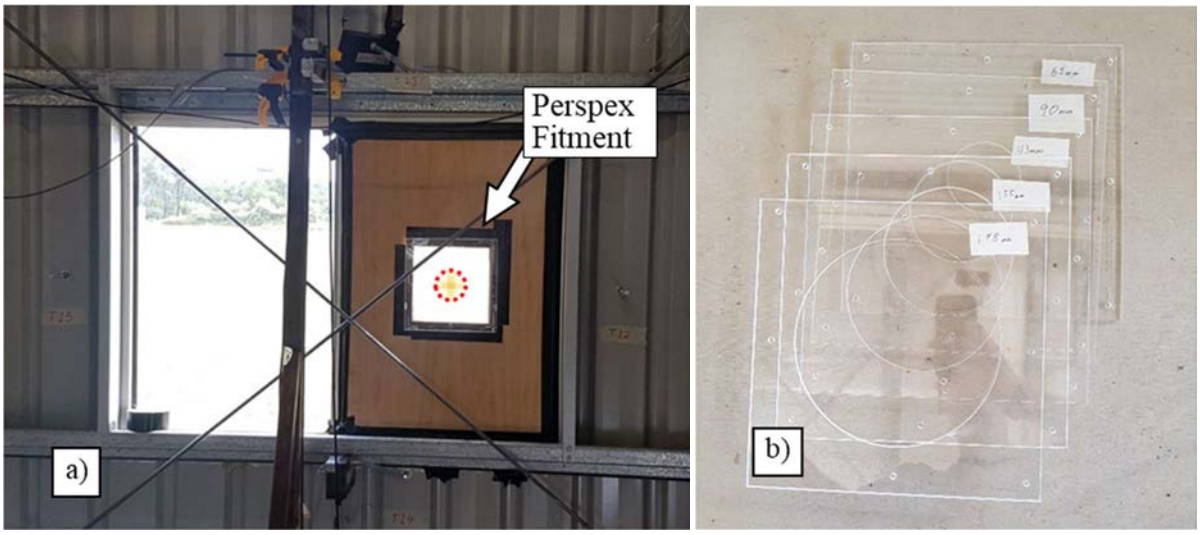

Figure 4.13. (a) Perspex sheet attached to plywood frame sealed in window fitment (b) Defined circular openings in Perspex sheets

Figure 4.14 shows the steady flow-rate ($\bar{Q}$) versus differential pressure across the envelope, ($\Delta\bar{p}$) for the Baseline Building, after the PA door was unsealed, and the series of defined circular openings were attached. The symbols are the measurements and the fitted lines are $\bar{Q}$ vs $\Delta\bar{p}$ from the best-fit Power-Law Coefficients, C and n (described in Section 4.3) substituted into the Power Law equation.

Figure 4.14 shows that the Baseline building has openings in the envelope causing air leakage. Leakage through the Baseline Building envelope was expected, as it was impractical to seal 100% of the porous openings. The porous openings that were not completely sealed included laps in the wall cladding, laps in roof insulation sheeting, ridge capping (behind roof insulation), and the flashings over the wall junctions.

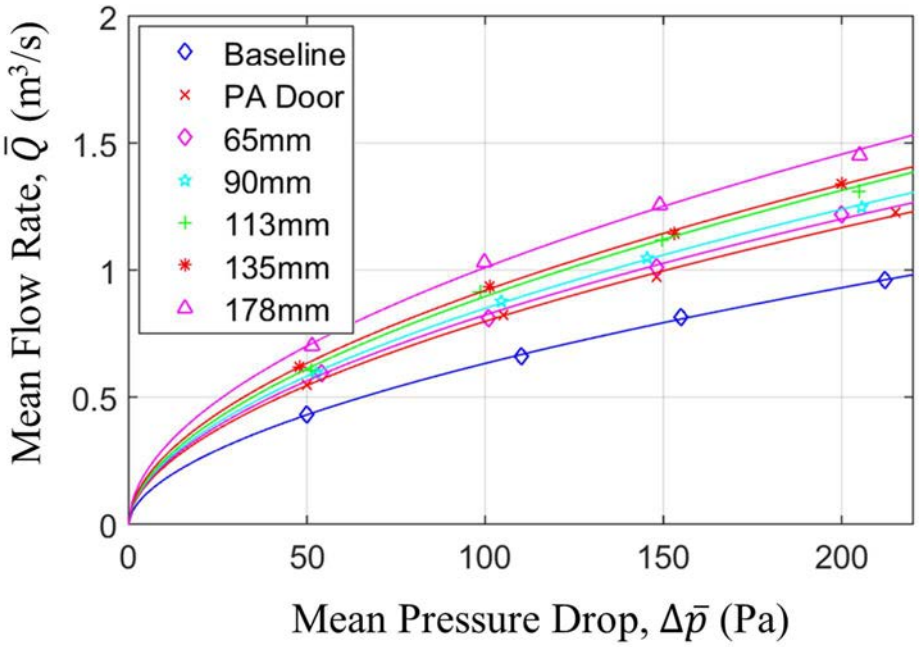

Figure 4.14. Mean flow rate vs mean pressure differential – Defined openings

The empirical flow exponent and coefficient for each Case (C and n), were determined using the unweighted log-linearized linear regression technique, detailed in Appendix D, and provided in Table 4.2. The total open area for each Case was determined from the empirical C and n values using Equation 2.7 and the steady discharge Equation 2.2 for a mean $\Delta\bar{p}$ test pressure of 125 Pa, and also given in Table 4.2. This method is used to define the open area from the $\bar{Q}$ and $\Delta\bar{p}$ measurements obtained from the irregular porous opening tests that follow.

Table 4.2. Calculated air-leakage test Power Law Coefficients and calculated open area from the Power-Law equation and steady discharge equation

Test Case	C $(m^3/s/Pa^n)$ $(\times 10^{-3})$	n	Calculated A_p, m^2 $(\times 10^{-3})$ Power-Law Equation 2.7.	Calculated A_p, m^2 $(\times 10^{-3})$ Discharge Equation 2.2.
BB	48.6	0.557	81.3	81.0
BB + PA	63.4	0.550	102.4	101.9
BB + PA + 65 mm dia.	66.7	0.546	105.6	105.1
BB + PA + 90 mm dia.	69.0	0.545	108.9	108.4
BB + PA + 113 mm dia.	70.5	0.548	113.0	112.4
BB + PA + 135 mm dia.	76.8	0.539	117.8	117.2
BB + PA + 178 mm dia.	88.9	0.528	129.0	128.6

*BB – Baseline Building
*PA – Personnel Access Door Unsealed

Table 4.3 compares the known open area of the five defined circular openings with the calculated area from Table 4.2. The results show a good match between the known area and calculated areas with the discharge coefficient *k* equal to 0.61 from potential-flow theory.

Table 4.3. Defined circular opening area and calculated open area

Circular opening diameter, m ($\times 10^{-3}$)	Known area = (Diameter)$^2 \times \pi$ /4, m^2 ($\times 10^{-3}$)	Calculated area Power-Law Equation 2.7, m^2 ($\times 10^{-3}$).	Calculated area Discharge Equation 2.2, m^2 ($\times 10^{-3}$).
65	3.32	3.22	3.15
90	6.36	6.56	6.51
113	10.0	10.5	10.5
135	14.3	15.5	15.3
178	24.9	27.0	26.7

4.3.3. Air-Leakage Testing – Background Leakage

Table 4.4 lists the nine stages of air-leakage tests carried out in sequence to ascertain the contributions of each element of the building to the total background leakage. Figure 4.15 shows the mean flow-rate ($\bar{Q}$) versus mean differential pressure across the envelope ($\Delta\bar{p}$) with symbols, and the corresponding $\bar{Q}$ vs $\Delta\bar{p}$ trend lines from the derived Power-Law coefficients *C* and *n*. Each air-leakage test consisted of a minimum of four measurements, up to $\Delta\bar{p} \cong 200$ Pa or $\bar{Q} \cong 4.5$ m^3/s, as the air-flow grid measurement range was 4.5 m^3/s and ducting seals were rated to 400 Pa.

Table 4.5 lists the fitted Power-law coefficients C and n from the non-linear regression technique, obtained from the measured $\bar{Q}$ and $\Delta\bar{p}$ values for the nine stages. The total porous opening area A_p from each sequential air-leakage test are given in Table 4.5 using the Power-law coefficients and Equation 2.7, and steady discharge Equation 2.2. Table 4.5 shows the porous opening areas from both methods (Equations 2.2 and 2.7) are very similar, as the empirical flow exponent n is about 0.5. In addition, Table 4.5 gives the individual porous open area from each stage by setting the power-law coefficient to 0.5 (i.e. steady discharge equation). It is presumed the order of the unsealing sequence would not influence the porous opening area results in Table 4.5. The porous open area through the roof is considered negligible compared to the walls as the combination of the open area from the gaps along the ridge capping and cladding overlaps are sealed from the building volume by the taught roof insulation rolled across the roof purlins and eave struts before the roof cladding was installed.

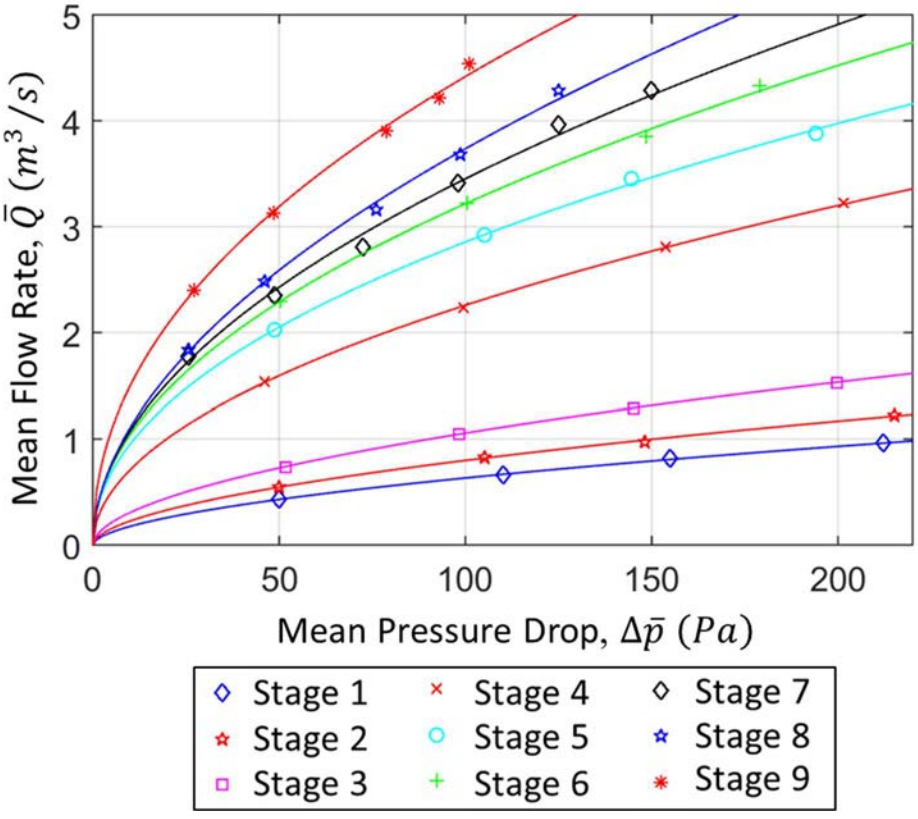

Figure 4.15. Mean flow-rate vs mean pressure across the envelope – Air-Leakage Test Stages

Table 4.4. JCU-ASIS Air-Leakage Test Sequence

Stage #	Stage Details
1	Baseline Building: caulking silicon, adhesive tape, compressed foam sealing gaps in the envelope.
2	Stage 1 + removed seals from Personnel Access door on Southern wall: Gap between door and door frame, perimeter of door frame to wall cladding.
3	Stage 2 + removed seals from all three (3) Windows: Gaps between sliding window panel and frame, perimeter of window frames and wall cladding.
4	Stage 3 + removed 12.22 m length of seals from Gable-end wall to roof flashings: Gap between wall and roof cladding on gable-ends and corner of side and gable-end walls.
5	Stage 4 + removed 12 m length of seals from Sidewall roof guttering: Gap between eave struts and wall cladding.
6	Stage 5 + removed 17.74 m length of seals from the floor Slab: Gaps between slab recess to wall cladding.
7	Stage 6 + removed seals from the 2.4 m high Western roller door tracks: Gaps between roller-door and aluminium guides (i.e. tracks) holding roller-door in place while closed, tracks to wall cladding.
8	Stage 7 + removed 2.76 m length of seals from the base of Western roller-door: Gap between roller-door and flood slab.
9	Stage 8 + removed 2.76 m length of seals above Western roller-door: Gaps between roller-door drum to door header-beam, wall cladding to header-beam, (All seals removed from envelope, except for sealed/barricaded Eastern roller-door).

Table 4.5. Power-law coefficients *C* and *n,* and cumulative and individual porous open area from Air-leakage test Stages

Stage #	C $(m^3/s/Pa^n)$ $(\times 10^{-3})$	n	A_p from Power-Law Equation 2.7, m^2 $(\times 10^{-3})$	A_p from Discharge Equation 2.2, m^2 $(\times 10^{-3})$	Each Component area A_p, m^2 $(\times 10^{-3})$
1	48.6	0.557	81	81	81
2	63.4	0.550	102	102	21
3	88.5	0.538	135	135	33
4	223	0.503	287	287	152
5	317	0.477	361	362	75
6	335	0.491	408	408	46
7	333	0.508	439	437	29
8	326	0.529	477	468	31
9	508	0.470	557	569	101

Table 4.6 provides detailed open areas of the background leakage of general construction gaps (per meter length), open area around parts of wall fitments (i.e. top, bottom, and sides, per meter length), and the combined porous open area around the total perimeter of wall fitments (per wall fitment unit).Table 4.6 can also be used to define the area of background leakage in industrial type building envelopes with different dimensions but similar construction tolerances. Table 4.6 is used to determine the total background leakage on each wall surface of the JCU-ASIS and the open area relative to the total wall (i.e. porosity $\varepsilon = A_p/A_T$) given in Table 4.6, assuming the leakage of the Baseline building is evenly distributed across the laps in the wall cladding

and junctions between the four walls. When nominally sealed, (i.e. as-built), the overall porosity of the JCU-ASI Shed $\varepsilon \cong 1.0\%$ of the total wall area.

Table 4.6. Detailed distribution of background leakage

Gap/Wall Fitment	Porous Opening Area, A_p ($\times 10^{-3}$)	
Personnel Access door	20.9	m^2/unit
Window	10.9	m^2/unit
Roller door, 2.4 m (H), 2.76 m (W)	160.7	m^2/unit
Top of roller door	36.4	m^2/m
Bottom of roller door	11.2	m^2/m
Single-track of roller door	6.1	m^2/m
Wall cladding to slab rebate	2.6	m^2/m
Side-wall cladding to roof sheeting	6.3	m^2/m
Gable-end wall flashing	12.5	m^2/m

Table 4.7. JCU-ASIS total wall porosity

Wall	Open Area A_p, m^2 ($\times 10^{-3}$)	Building Porosity, $\varepsilon\ (A_p/A_T)$
North	92	0.51 %
East	275	1.39 %
South	104	0.58 %
West	275	1.39 %
Total	746	0.99 %

4.3.4. Comparison with Other Previous Studies

The volume of air pumped into the building during air-leakage tests is generally expressed as flow-rate per unit wall area, as an effective measure of permeability relative to the pressure drop across the envelope. The total wall area of the JCU-ASIS is 75.5 m^2. Figure 4.16 shows the air-leakage test flow-rate $(\bar{Q})$ per unit wall area versus differential pressure across the envelope $(\Delta\bar{p})$, measurements and trend lines from Stage 1 (Baseline Building) and Stage 9 (Nominally sealed + sealed Eastern roller-door). Figure 4.16 also shows the air-leakage test data from the TTU WERFL building by Yeatts (1994), a typical Australian house from the CSIRO by Michell and Biggs (1982), and the averaged results from several super markets, schools, and high-rise buildings conducted by Shaw and Jones (1979) and Shaw and Tamura (1976).

Figure 4.16 shows that the effective permeability of the Baseline JCU-ASIS (Stage 1) is similar to the Australian house and a High Rise building. The Nominally sealed JCU-ASIS + sealed Eastern roller door (Stage 9) (i.e. typical industrial building) is considerably more porous than

all other building types. The larger porosity of the JCU-ASIS is largely due to the construction tolerances associated with the detailing at envelope discontinuity connections/flashings, as air-infiltration/air-leakage is not an important criterion for industrial type buildings as internal ventilation systems are at ambient temperatures in most tropical and temperate climates.

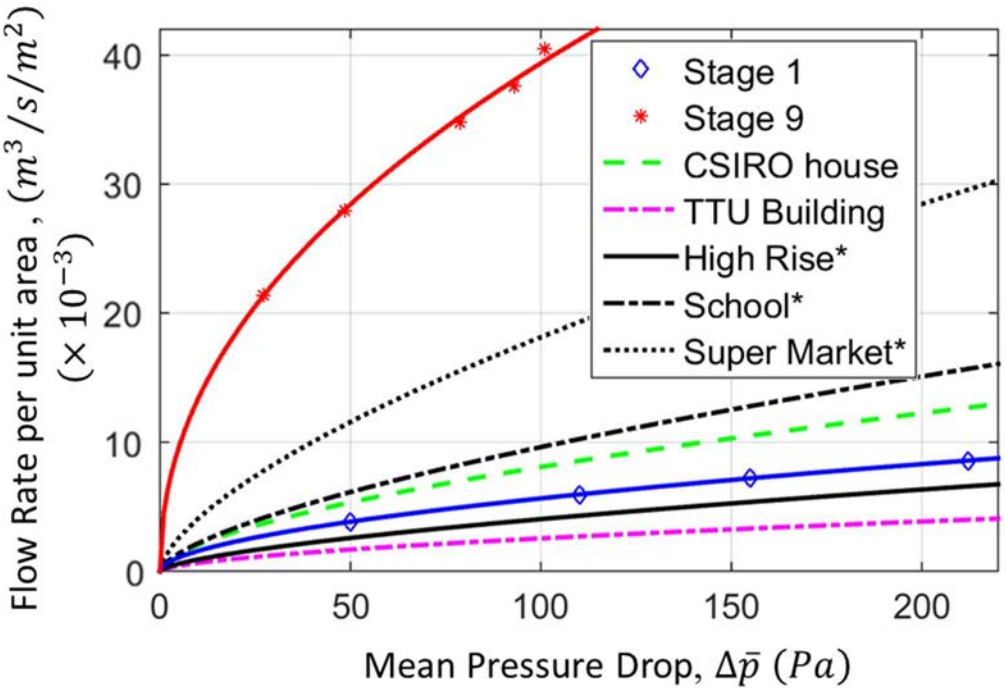

Figure 4.16. Comparison of JCU-ASIS flow rate per unit wall area vs pressure drop across the envelope with other previous buildings tested.

The air-leakage testing of the JCU-ASIS gives the area and distribution of porosity and shows significantly more porosity than other previously studied building types. The combination of accurate background leakage area and the external pressures around the envelope enables appropriate interpretation of the internal pressures data.

4.4. Building Flexibility

As indicated in Section 2.9.1, the flexibility of a building envelope will damp the internal pressure fluctuations. The ratio of the bulk modulus of air, K_A, to the bulk modulus of the building, K_B, provides a measure of the damping by means of the additional air required to enter, relative to the building volume. The influence of the flexibility can be described by effectively increasing the building volume during internal pressure analysis, where the effective building volume $V = V_B(1 + K_A/K_B)$, where V_B is the standard building volume. Here, the bulk modulus of the building $K_B = \Delta p/(\Delta V/V)$, is the change in the internal pressure per unit volumetric strain.

Linear Variable Displacement Transducers (LVDT's) installed at selected points on the JCU-ASIS were used to measure the deflection during the pressurization of the JCU-ASIS to define the volumetric change with respect to the internal pressure change. The JCU-ASIS was pressurized to 390 Pa by the air-handler unit in steps of about 50 Pa to 75 Pa, at which steady pressure was maintained, allowing measurement of deflection at the select locations.

Ten LVDTs were mounted on rigid steel frames inside the JCU-ASIS at locations shown in the schematic Figure 4.17 and detailed position information listed in Appendix B Table B.1. All measurements were relative to the independent rigid steel frames. The dashed lines in Figure 4.17 show the locations of the wall girts, mullions, and roof purlins along the columns and rafters.

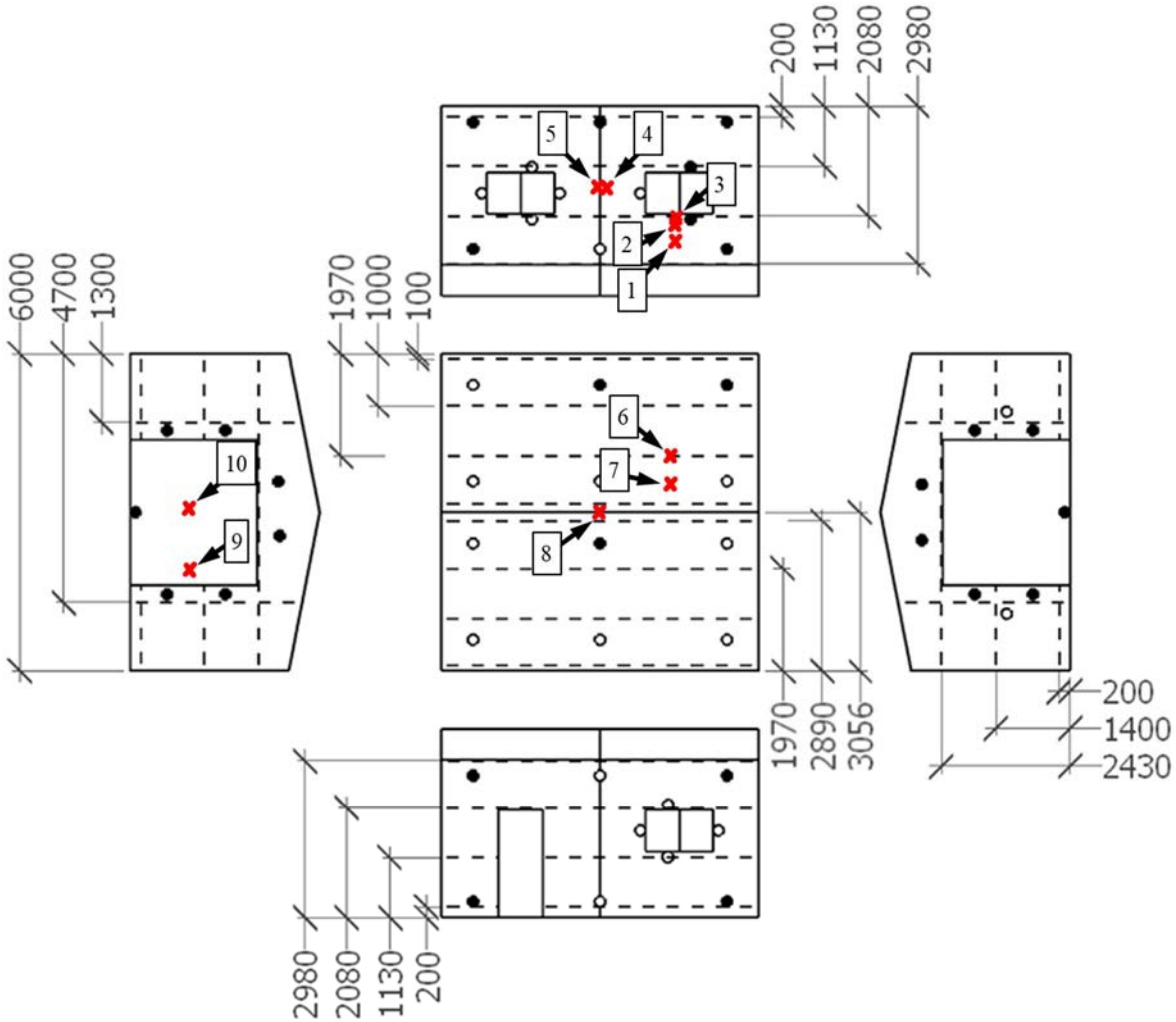

Figure 4.17. Schematic of LVDT locations – Dashed lines are purlins, girts, and mullions (all dimensions in mm)

Figures 4.18 to 4.21 show the LVDTs mounted on the steel frames on the JCU-ASIS at their respective measurement locations. Vishay® 130 mm 5 kOhm LVDTs with an accuracy of ±0.01 mm were used, and recorded at 120 Hz. 100 mm long soft springs were installed on the shafts to enable measurements with variable displacement.

Figure 4.18. LVDT #9 and #10 mounted at edge and centre of the Western roller-door

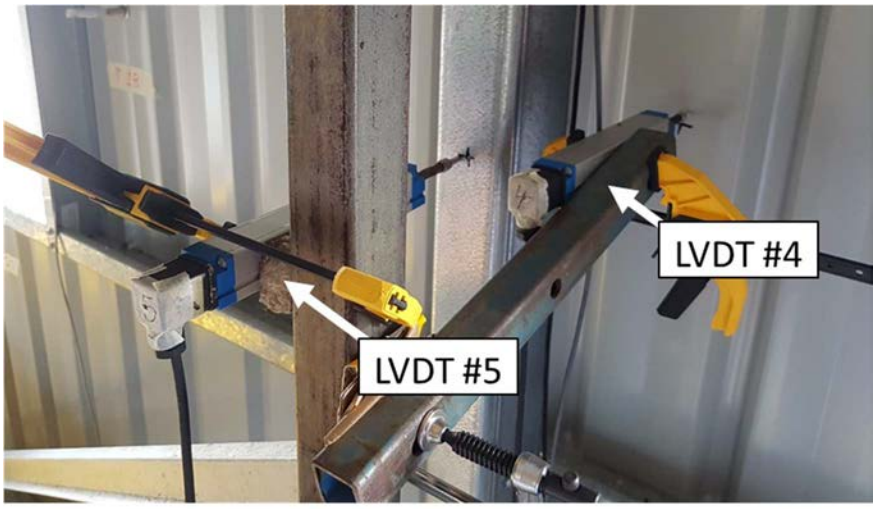

Figure 4.19. LVDT #4 and #5 mounted on the central Northern wall column and cladding beside the Northern wall column

Figure 4.20. LVDT #1, #2, and #3, mounted on the Northern wall cladding and wall girt between Eastern and middle portal frames

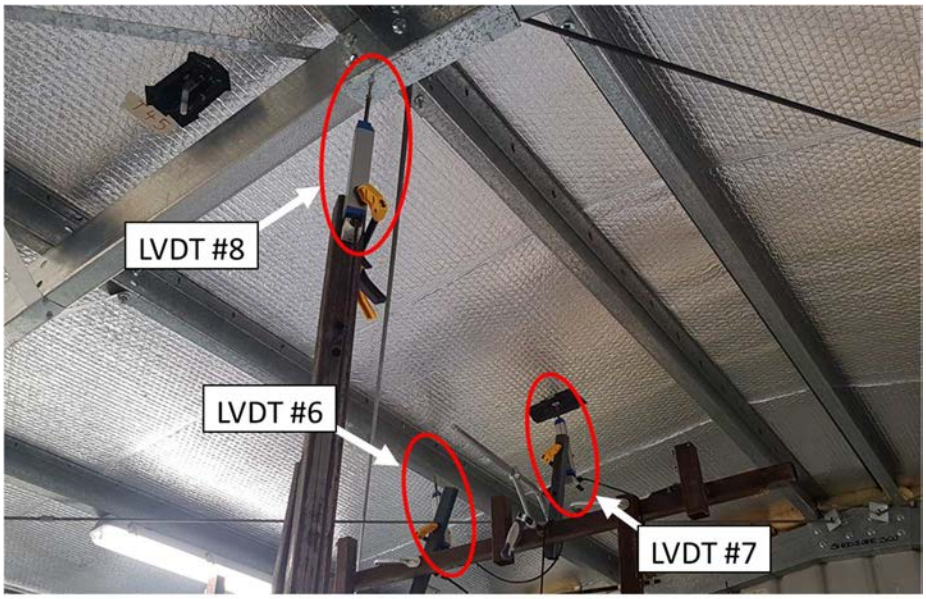

Figure 4.21. LVDT #6, #7, and #8, mounted on the roof cladding and purlin perpendicular to the roof slope, and vertically at the central portal frame apex gusset plate

Figures 4.22, 4.23, and 4.24 show the deflection vs mean pressure difference $\Delta\bar{p}$ at LVDT #1-5 on the Northern wall, LVDT #6-8 on the roof, and LVDT #9-10 on the Western roller-door, respectively.

Figure 4.22 shows that the centre of the column (LVDT #5) deflects linearly up to 0.3 mm at 390 Pa, while the cladding between the 950 mm girt spacing (LVDT #4) deflected 1.6 mm. The wall cladding between the 900 mm girt span and girt above the window between the Eastern and central portal frames (LVDT #1, #2, and #3) deflects to about 1.2 mm. Figure 4.23 shows that the roof cladding and purlin (LVDT #6 and #7) deflects linearly to about 4.1 mm and 4.3 mm, respectively and the apex of the central portal frame (LVDT #8) deflects to about 4.3 mm. The centre of the 6 m roof span is shown to be more flexible than the 3 m high sidewall due to stiffer base plate connection on the sidewall.

Figure 4.24 shows that the side of the Western roller-door (LVDT #9) deflects linearly to about 20 mm at 390 Pa, whilst the centre of the roller door (LVDT #10) deflected to 53 mm at about 210 Pa as the LVDT reached the end of its stroke length. The linear deflection of the side of the roller-door suggests that the centre of the span would also have deflected linearly up to about 100 mm at 390 Pa.

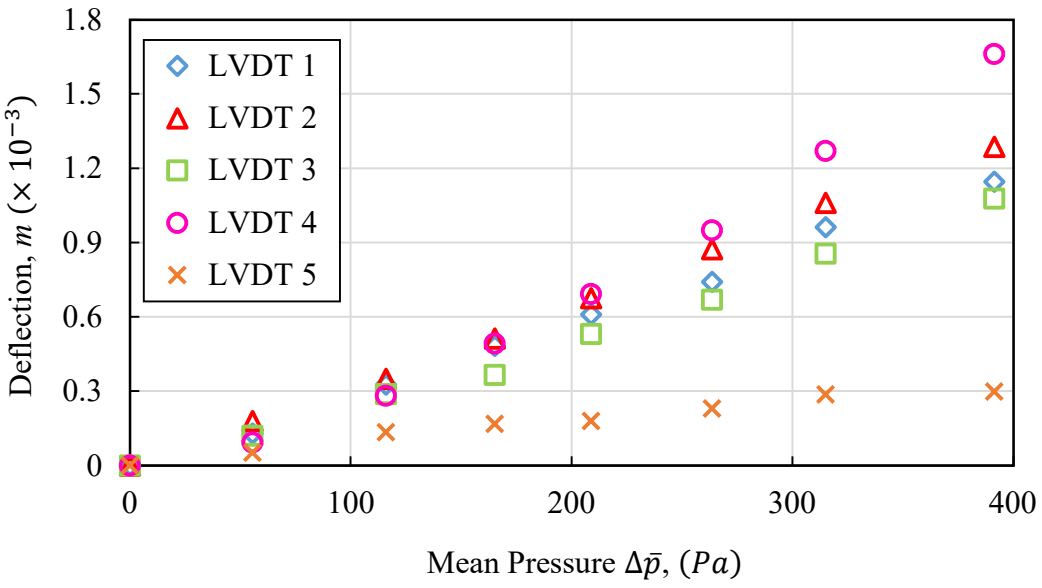

Figure 4.22. JCU-ASIS Northern wall deflection versus pressure differential

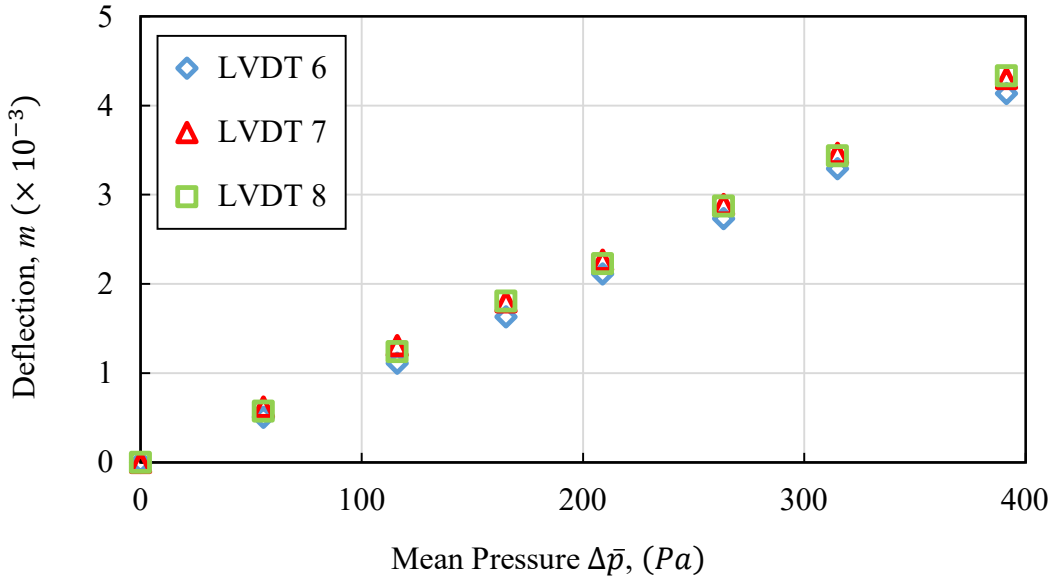

Figure 4.23. JCU-ASIS roof deflection versus pressure differential

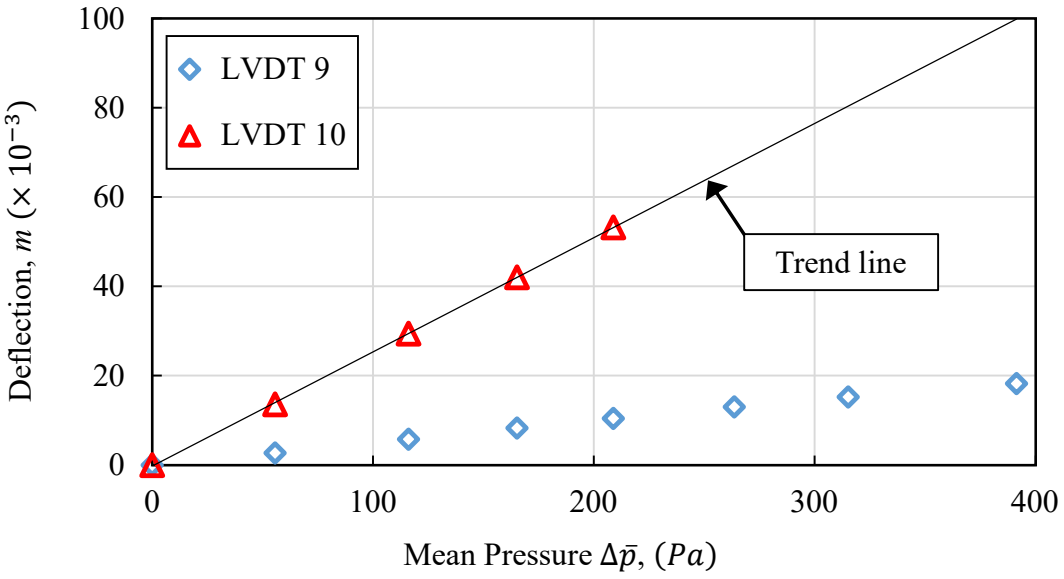

Figure 4.24. JCU-ASIS Western roller door deflection versus pressure differential

The change in building volume ΔV is estimated by Equation 4.1. Where δ_{Roof}, δ_{Side}, δ_{Gable}, and $\delta_{R.D}$ are the maximum deflections of the roof, sidewalls, gable-end walls without the roller door, and the roller door respectively. Further, h, d, and b are the eave height 3 m, sidewall length 6 m, and gable-end wall breadth 6 m, respectively. Further, $h_{R.D}$, and $b_{R.D}$ is the height and breadth of the roller doors, and α is a deflected shape factor $\cong 0.6$, Vickery (1986). The internal pressure of 390 Pa produced approximately $\delta_{Roof} = 4.3$ mm, $\delta_{Side} = 1.6$ mm, $\delta_{R.D} = 100$ mm, δ_{Gable} is estimated to be similar to δ_{Side}.

$$\Delta V = \alpha\left[\delta_{Roof} bd + 2\delta_{Side} hd + 2\delta_{Gable} hb + 2\delta_{R.D} h_{R.D} b_{R.D}\right] \quad 4.1$$

The effective volume of the JCU-ASIS is then given by $V = V_B(1 + K_A/K_B)$, where the standard building volume $V_B = 119$ m^3, $K_A = \gamma p_0 = 1.419 \times 10^5\ Pa$, and $1/K_B = (\Delta V/V)/\Delta p$. Considering the nominally sealed JCU-ASIS, applying the deflection measurements to Equation 2.9, the change in the JCU-ASIS volume at 390 Pa is given in Equation 4.2 and the ratio of the bulk modulus of air to the bulk modulus of the building in Equation 4.3.

$$\begin{aligned}\Delta V = 0.6[0.0043 \times 6 \times 6 \ + 2 \times 0.0016 \times 3 \times 6 + 2 \times 0.0016 \times 3 \times 6 \\ + 2 \times 0.1 \times 2.4 \times 2.76] = 0.96\ m^3\end{aligned} \quad 4.2$$

$$\frac{K_A}{K_B} = \ K_A\left[\frac{\Delta V/V}{\Delta p}\right] = 1.419 \times 10^5\ Pa\left[\frac{0.96\ m^3/119\ m^3}{390\ Pa}\right] \cong 3.0 \quad 4.3$$

Thus, the influence of the nominally sealed JCU-ASIS envelope flexibility on internal pressure fluctuations is described by effectively increasing the building volume by about 3 times in analytical methods, where $V = 119 \times (1 + 3) = 476$ m^3.

Vickery (1986) applied this analytical approach of the volumetric strain of low-rise industrial type buildings based on the deflection limits of structural member spans and showed that the K_A/K_B of a considerably stiff and flexible building may range between 0.2 and 5, thus the effective building volume may range between 1.2 and 6 times the standard building volume V_B.

The deflection of the Texas Tech University WERFL building was measured during pressurization up to 650 Pa and was determined to have a bulk modulus ratio K_A/K_B of about 1.5, thus effective building volume 2.5 times the standard building volume. The matching of the measured Helmholtz frequency of the WERFL building and the calculated Helmholtz frequency using the effective volume, illustrates the effective volume distortion satisfactory characterised the volume distortion of the envelope.

4.5. Wind Induced Pressures

Wind-induced internal pressures in the JCU-ASI Shed are studied in two parts (i) with a nominally sealed envelope (ii) with a range of open wall fitments (i.e. open window, rollerdoor). The wind speed and directions, and corresponding external and internal pressures on JCU-ASI Shed, were analysed and compared with results from theoretical and numerical methods, the FSTE results, and other previous model-scale and full-scale results. The distribution of background leakage from the air-leakage testing is used to define the windward and leeward open area for analysis.

A total of 2,800 hours of data was collected, and statistical analysis of the data was used to identify conditions with appropriate wind speeds from select wind directions. Stationary wind speed and wind-angle data-blocks were extracted from the 10-minute runs to produce data sets for analysis. Stationarity checks were conducted via the Trend and Run tests, detailed in Section 3.1.5 and validated with visual inspection.

Most of the data collated was for the nominally sealed JCU-ASI Shed provides data for winds approaching from several wind-directions around the compass. Mean wind approach angles within ±30° from the orthogonal building directions were utilised to define windward walls for each Case. Although stationary, mean wind angles within ±30° orthogonal directions are considered for analysis, similar to the FSTE, wind-induced pressures are not assessed in terms of the mean approach wind speed, (i.e. pressure coefficients C_p), as the range of C_p values produced has significant variation within the mean wind angles $\bar{\theta} = 0° \pm 30°$ and may be misinterpreted. The internal pressure response in the JCU-ASIS is characterised with respect to the external pressures applied to the building (i.e. across walls and openings).

Further, pressures were recorded at relatively low wind speeds compared to severe windstorms, it is acknowledged this increases uncertainties in results, however, meaningful internal to external pressure relationships are still derived, presented, and discussed in the following section.

Internal and external pressures measured on the walls and roof are presented along with spatially-averaged external pressures across potential openings (i.e. closed wall fitments). The spatially-averaged pressures were determined while the JCU-ASIS was nominally sealed by averaging the pressure time series from selected pressure taps on and around wall fitments to provide an estimate of the temporally varying external pressures applied to that opening area. An area-averaged response function was applied to the external pressure from a tap beside open wall fitments to produce an effective spatially-averaged external pressure across the open wall fitment.

4.5.1. Nominally Sealed Building

External and internal pressures were measured on the JCU-ASI Shed with all the doors and windows closed and different levels of wall porosity, as listed in Table 4.8. Case NS1 is the building as-built with no openings (other than the background porosity of the building) (i.e. Stage 9 from the air leakage test sequence with the addition of leakage around the Eastern roller door). Case NS2 is the building as-built with the addition of the top and bottom of the Western

roller door sealed (i.e. Stage 7 from the air leakage test sequence with the addition of leakage around the Eastern roller door), significantly reducing the porosity of the Western wall, providing a similar porosity distribution to a building with a single Eastern roller door (no Western roller door).

Table 4.8. Nominally sealed JCU-ASI Shed background leakage area

Wall Surface	Case #			
	NS1		NS2	
	Open Area, m^2 ($\times 10^{-3}$)	% of Wall	Open Area, m^2 ($\times 10^{-3}$)	% of Wall
North	91.6	0.509	91.6	0.509
East Wall	275	1.39	275	1.39
South Wall	104	0.577	104	0.577
West Wall	275	1.39	134	0.706
Total	746	0.988	610	0.808

Data collected for Cases NS1 and NS2 amounts to 4,188 and 3,311 10-minute runs respectively. The stationary wind data blocks extracted from the total number of tests is summarized in Table 4.9 for each wind angle range, where the stationary signal length is about 1-minute. The analysis of the wind-induced data is primarily focused on winds from $\theta \approx 90°$.

Table 4.9. Stationary wind data range – Nominally Sealed Cases

Case #	NS1		NS2	
Wind angle range	Mean Wind Speed range, m/s	Total Minutes	Mean Wind Speed range, m/s	Total Minutes
335.5° – 22.5°	1.9 – 4.5	43	1.5 – 4.4	22
22.5° – 67.5°	1.5 – 5.3	136	2.0 – 6.8	150
67.5° – 112.5°	1.5 – 3.9	87	1.6 – 5.7	109
112.5° – 157.5°	1.5 – 3.2	23	1.5 – 3.5	17
157.5° – 202.5°	1.8 – 5.2	20	-	-

Figures 4.25 and 4.26 show typical internal and external point pressure measurements on the windward, sidewall, and leeward wall and roof taps (i.e. taps T7, T13, T26, and T41) for Cases NS1 and NS2 respectively, and the corresponding wind speed and direction for winds approaching from $\theta \cong 90°$.

The pressure power spectral density (i.e. spectra) $S_p(f)$ of the same pressure taps for winds from $\theta \cong 90°$ for Cases NS1 and NS2 are shown in Figure 4.27 and 4.28 respectively. The spectra shown in Figures 4.27 and 4.28 are the averaged of the 1-minute stationary signals for $\theta \cong 90°$. The trends observed are expected to be similar for increases in approach wind speed.

Figures 4.25 and 4.26 show that the windward wall tap (T7) experiences positive pressures whilst the other walls and roof are subjected to negative pressures. The pressure taps on the roof (T41) and sidewall (T13) are in regions of flow separation (i.e. 0.6 m and 1.3 m from the windward roof and wall edges) and are subjected to high intermittent suction pressures. The pressure tap on the leeward wall (T26), experiences low negative pressures. Further, pressure fluctuations at the windward wall tap (T7) follows trends in the variations of approach wind speed and direction (from $\theta \cong 90°$) which produce highly complex pressure fluctuations.

Figures 4.27 and 4.28 show the pressures on the roof (T41) and sidewall (T13) have greater energy at higher pressure fluctuations (greater than 1 Hz) due to the building induced turbulence compared to the windward wall pressure (T7). The pressure tap on the leeward wall (T26) in the wake of the building experiences the least amount of energy of the external pressure signals.

Figures 4.25 and 4.26 show that the internal pressures for NS1 and NS2 fluctuate between the windward and leeward wall pressures, with internal pressures slightly more positive for Case NS2. This is due to by the greater windward opening area relative to leeward opening area ($A_W/A_L = 0.83$) compared to Case NS1 ($A_W/A_L = 0.58$) for winds approaching from $\theta \cong 90°$. Further, Figure 4.27 and 4.28 show that the internal pressure spectral energy in Case NS2 is greater than NS1 and is explained by the lower area of background leakage on the leeward wall, reducing the influence of the low energy wake pressures on the internal pressure fluctuations.

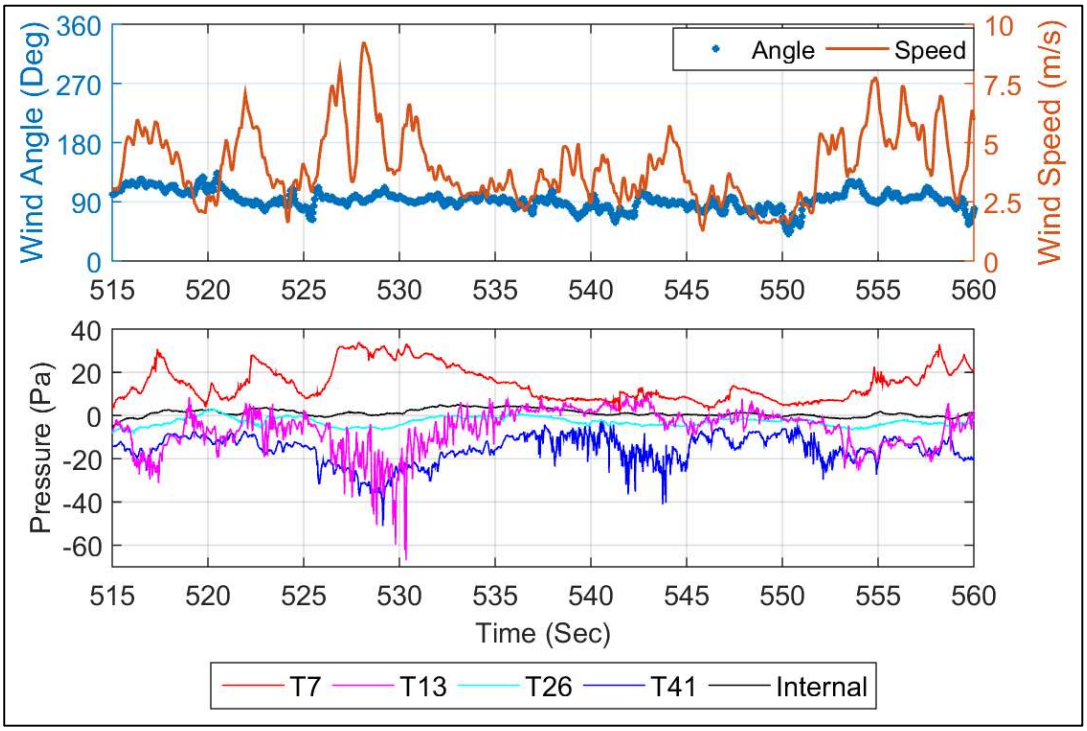

Figure 4.25. Wind speed, wind direction ($\bar{\theta} \cong 90°$), and internal and external point pressures vs time: Case NS1

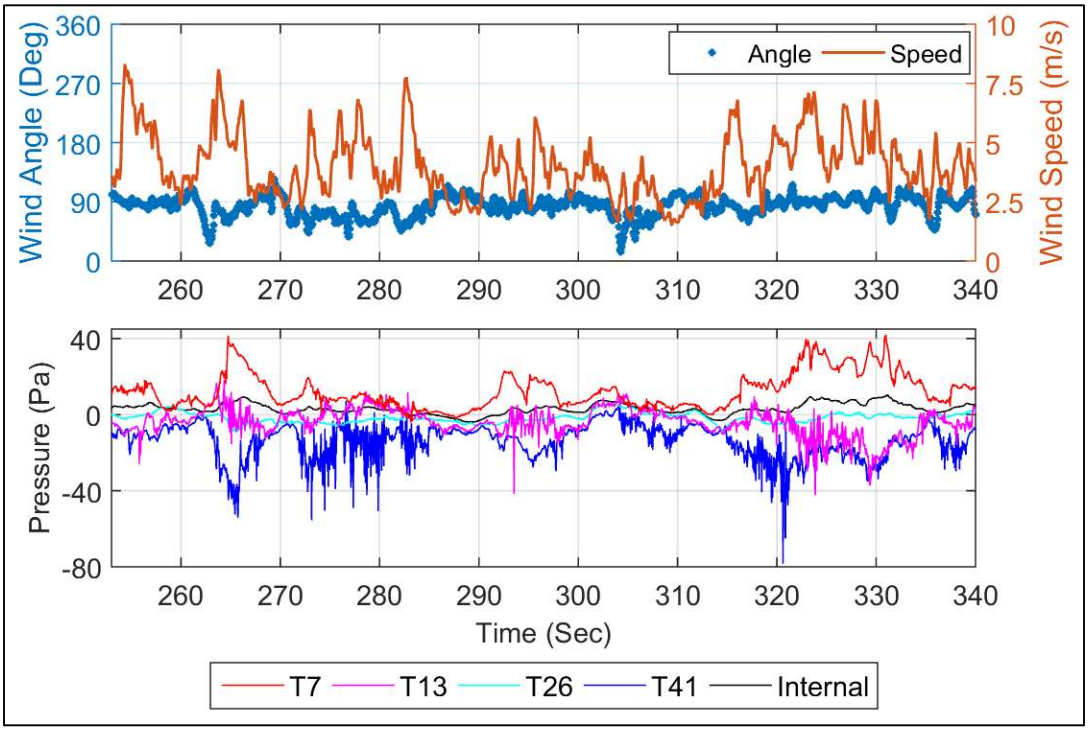

Figure 4.26. Wind speed, wind direction ($\bar{\theta} \cong 90°$), and internal and external point pressures vs time: Case NS2

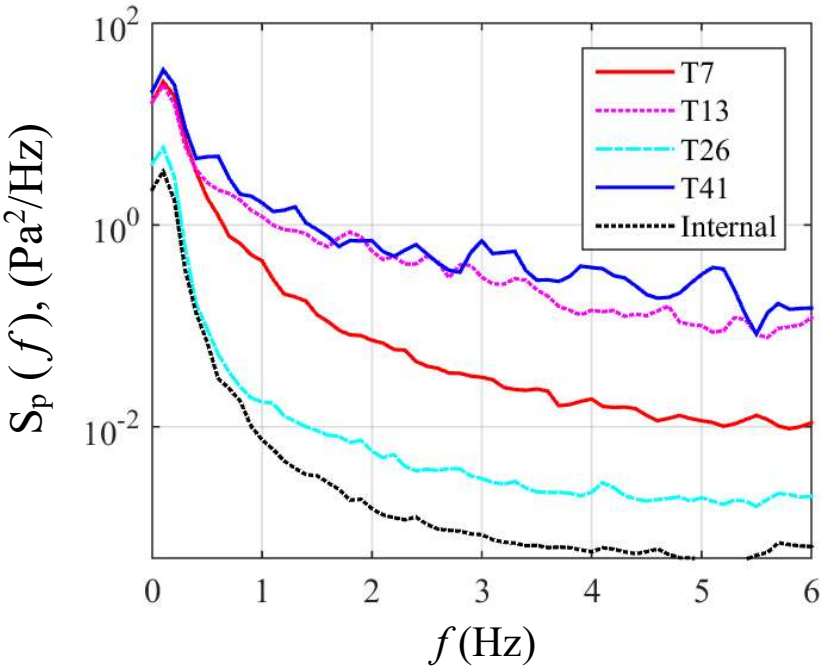

Figure 4.27. Internal and external pressure spectra: Case NS1

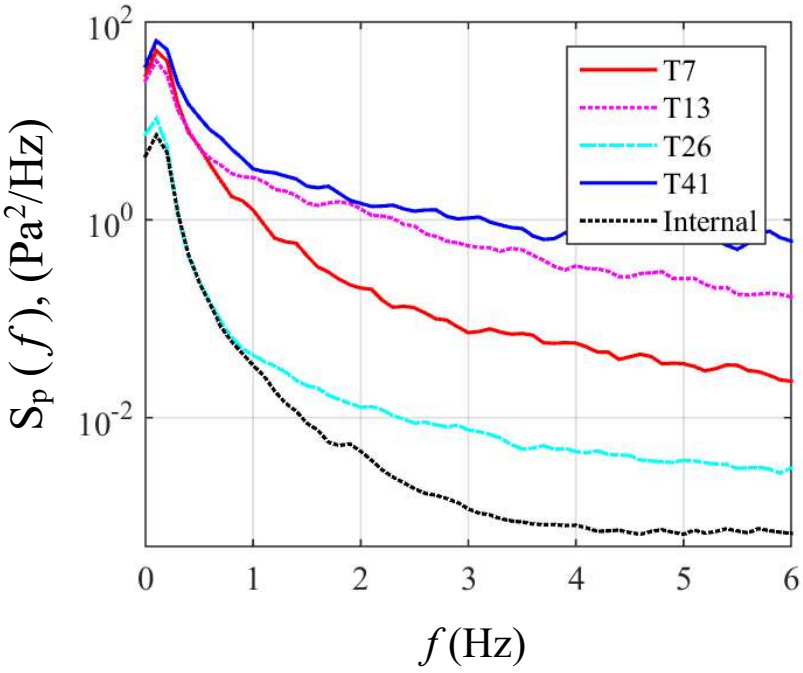

Figure 4.28. Internal and external point pressure spectra: Case NS2

Figures 4.29 and 4.30 show the spatially-averaged external pressure on the four walls for Cases NS1 and NS2, respectively for the same time-history signals as in Figures 4.25 and 4.26. Here the Eastern wall pressure was acquired from spatially-averaging of pressure taps T1, T2, T3, T5, T6, T7, and T8; the Northern wall from pressure taps T10, T11, T17, T22, and T23; the Western wall from pressure taps T24, T25, T26, T27, T28, T29, and T30; and Southern wall from pressure taps T31, T32, T39, and T40.

Figure 4.30 shows that the internal pressure is mostly influenced by the windward Eastern wall pressure (most porous wall of the JCU-ASIS due to gap above roller-door) significantly contributing to the internal pressure, whereas the internal pressure signal in Case NS1 (i.e. Figure 4.29) fluctuates about 0 Pa.

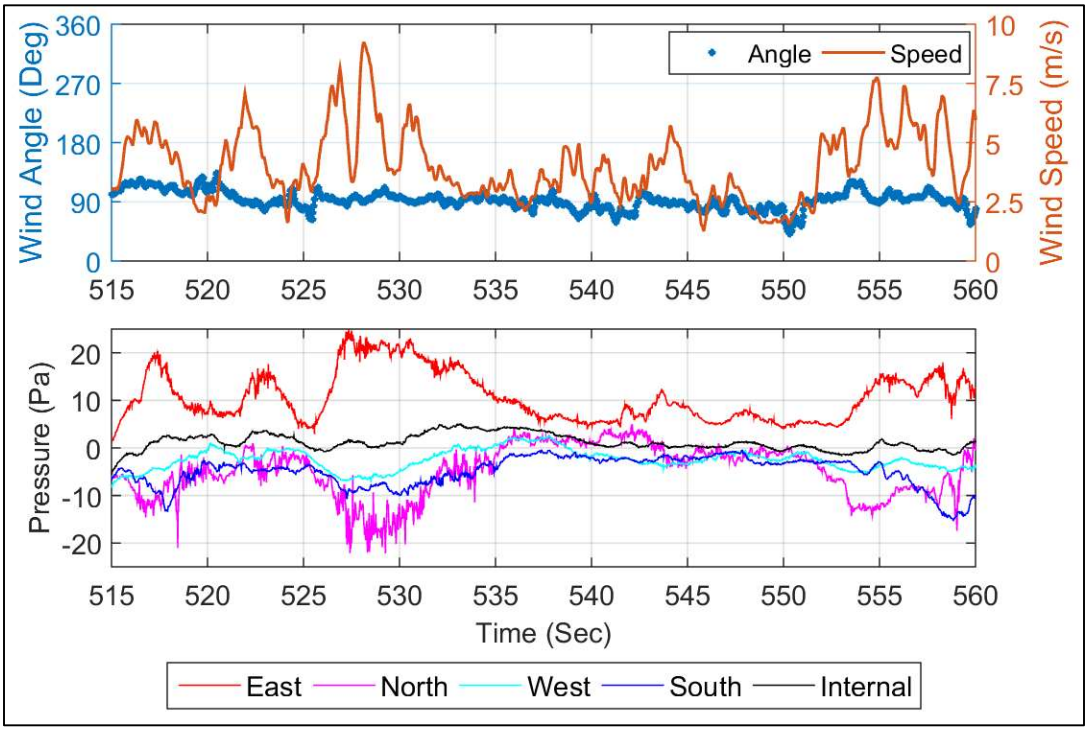

Figure 4.29. Wind speed, wind direction ($\bar{\theta} \cong 90°$), and internal and area-averaged external pressures vs time: Case NS1

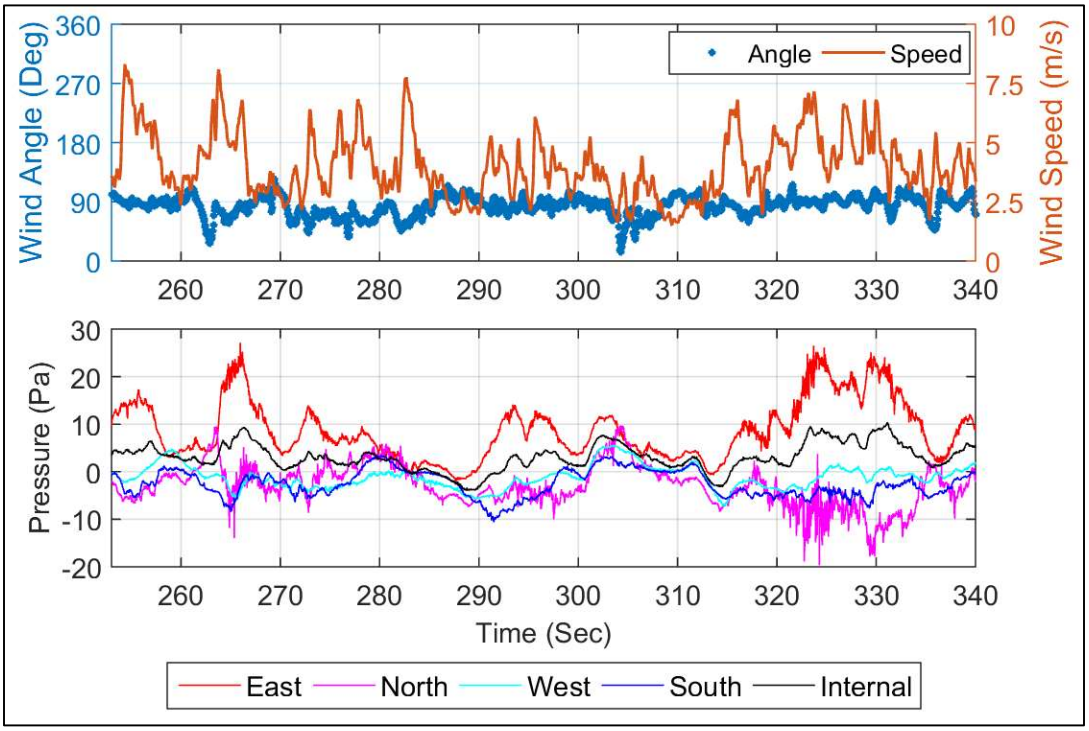

Figure 4.30. Wind speed, wind direction ($\bar{\theta} \cong 90°$), and internal and area-averaged external pressures vs time: Case NS2

Figures 4.31 and 4.32 show the spatially-averaged pressure spectra for Cases NS1 and NS2, respectively. Similar to Figures 4.27 and 4.28, the windward (i.e. Eastern) wall pressure fluctuations are similar to the wind velocity fluctuations with 90% of the energy below 0.5 Hz. The leeward (i.e. Western) wall has the least amount of pressure energy in the wake of the building, where the area-averaged pressure on the side (i.e. Northern and Southern) walls has significantly less energy than the single tap pressures behind the windward edge (i.e. T13) shown in Figures 4.27 and 4.28. This is due to the area-averaging of pressures in the flow separation region and reattachment regions which is more distant from the windward edge. Further, the Northern wall has more energy than the Southern wall although they are both side walls due to stronger winds typically approaching from the East-North-East, with a mean wind approach angle $\bar{\theta} = \pm 30°$.

Figures 4.31 and 4.32 also show that the internal pressure fluctuations are similar to the leeward wall pressure fluctuations and are significantly attenuated compared to the windward and sidewall pressure fluctuations. The range of pressure fluctuations admitted through the envelope, that generate the internal pressure fluctuations, is described by Vickery (1986) and Harris (1990) by the characteristic frequency f_c of the building, discussed in Section 2.6. Where external pressure fluctuations above f_c are attenuated and not passed effectively through the porous openings, where frequencies below f_c are admitted through the envelope.

The formula that describes f_c derived by Vickery (1986), given in Equation 2.12, predicts that f_c is not constant (f_c decrease as $\overline{U}_h$ increases), and that the range of internal pressure is also a function of the approach wind conditions.

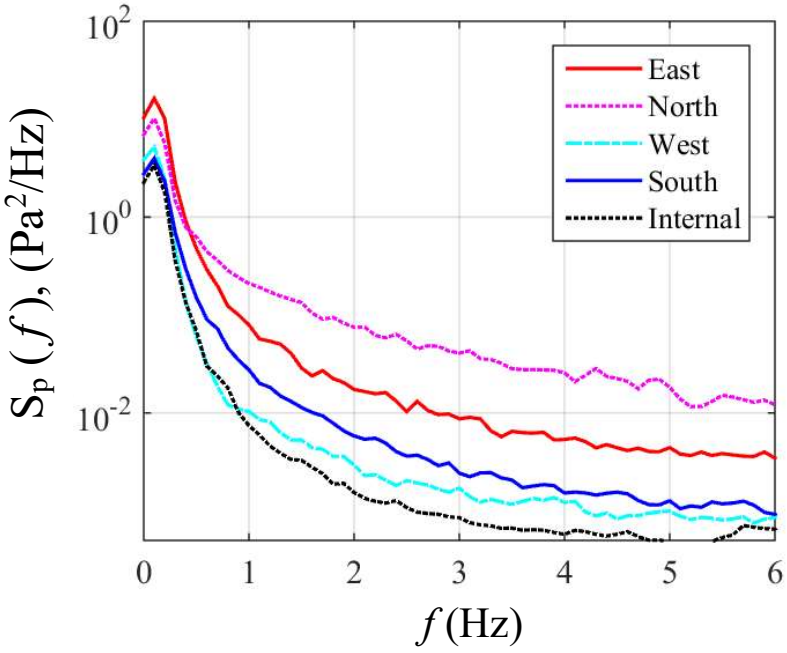

Figure 4.31. Internal and area-averaged external wall pressure spectra for Case NS1, $\bar{\theta} \cong 90°$

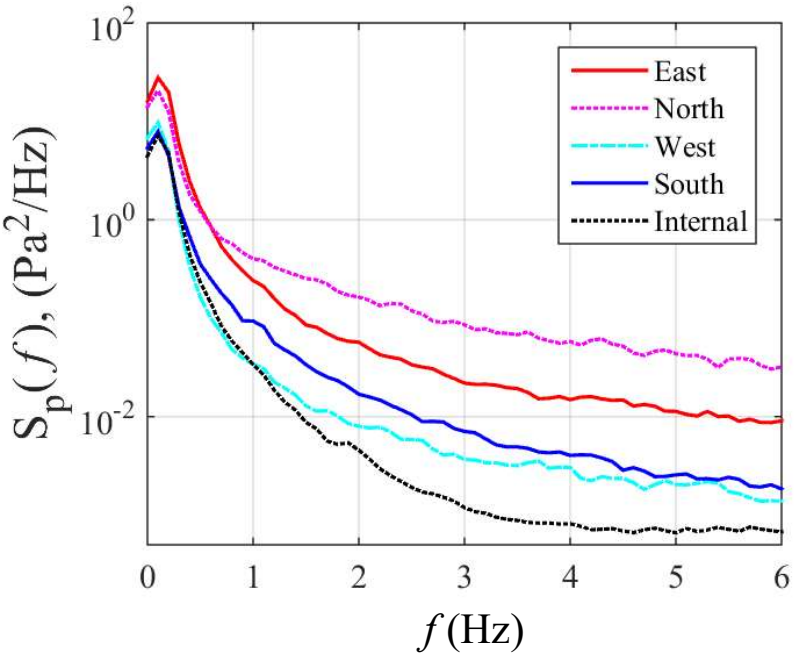

Figure 4.32. Internal and area-averaged external wall pressure spectra for Case NS2, $\bar{\theta} \cong 90°$

Figures 4.33 and 4.34 show the internal spectrum and combined spatially-averaged external wall pressure spectra across all four walls for Cases NS1 and NS2 respectively. As the porosity across the envelope is across all walls, the combined external pressure signal across the envelope drives all internal pressure fluctuations. Figures 4.33 and 4.34 show that the internal pressure fluctuations follow the low frequencies of the driving fluctuations before attenuation at higher frequencies above the characteristic frequency f_c, at about 0.3 Hz and 0.6 Hz for Case NS1 and NS2 respectively. The greater characteristic frequency of Case NS2 (i.e. $f_{c,NS2} > f_{c,NS1}$) is explained by reduced influence of low energy pressure fluctuations in the wake of the building. Sharma (1996) showed that f_c is highly dependent on the magnitude of porosity from model-scale wind tunnel studies, further, a model-scale study by Humphreys *et. al.* (2017) showed that as the uniform porosity increases the characteristic frequency also increases, inducing greater internal pressure fluctuations.

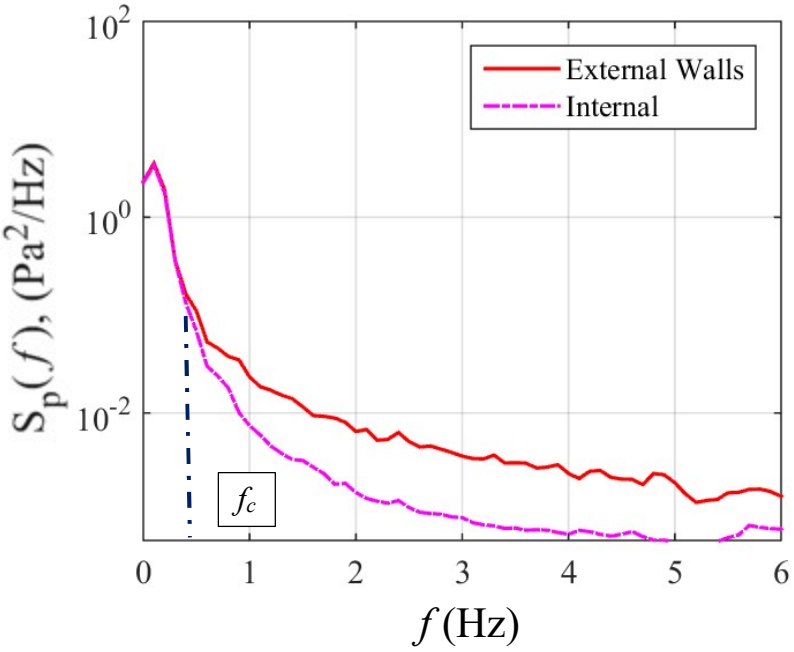

Figure 4.33. Internal and combined external wall pressure spectra for Case NS1, $\bar{\theta} \cong 90°$

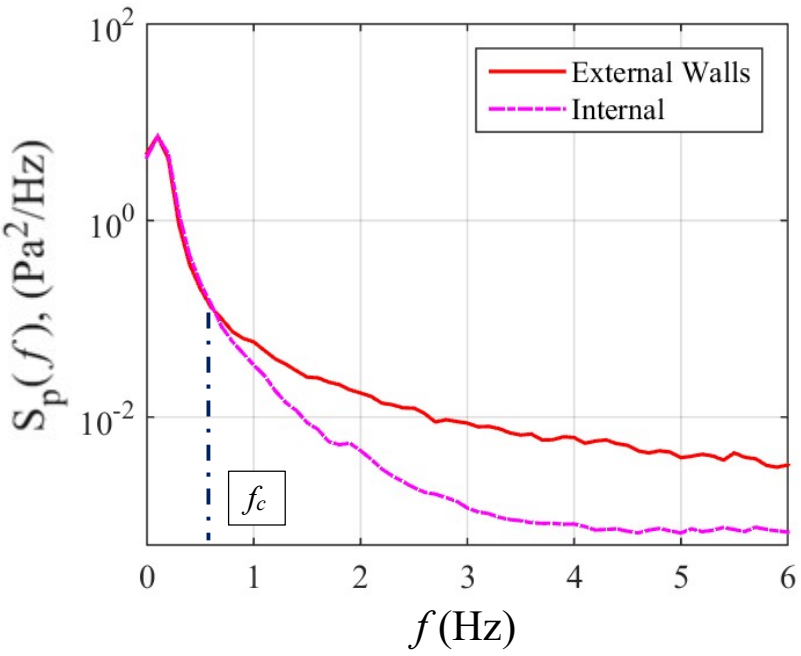

Figure 4.34. Internal and combined external wall pressure spectra for Case NS2, $\bar{\theta} \cong 90°$

Table 4.10 shows the mean, standard deviation, minimum, and maximum ($\bar{p}$, σ_p, $\check{p}$, and $\hat{p}$) internal pressure, area-averaged external wall pressures, and combined Leeward* walls (i.e. combined Northern, Southern, and Western walls for $\theta \cong 90°$) pressure signals on the JCU-ASIS, averaged from the stationary signals for $\theta \cong 90°$.

Table 4.10 shows that the mean internal pressure in the nominally sealed building Cases NS1 and NS2 is between the mean windward and leeward wall pressures and slightly positive. This is due to the uneven distribution of building porosity around the JCU-ASIS envelope (i.e. largest porosity on Eastern (windward) wall relative to leeward walls). These findings are similar to the full-scale study by Morrison and Reinhold (2015) at IBHS where internal pressures in a nominally sealed industrial building were significantly influenced by the approach wind angle relative the wall with a closed roller door, that had considerable leakage area relative the rest of the building.

Table 4.10. Internal and area-averaged external pressures for $\bar{\theta} \cong 90°$

Surface	NS1				NS2			
	$\bar{p}, Pa$	σ_p, Pa	$\check{p}, Pa$	$\hat{p}, Pa$	$\bar{p}, Pa$	σ_p, Pa	$\check{p}, Pa$	$\hat{p}, Pa$
Internal	0.87	1.14	-2.12	3.81	2.99	1.65	-0.83	7.12
Eastern Wall	6.12	2.67	0.52	13.9	9.35	3.53	2.26	19.7
Northern Wall	-2.49	2.53	-11.1	4.36	-2.17	3.67	-13.0	7.16
Western Wall	-1.25	1.52	-5.15	2.24	-1.74	1.93	-6.65	2.62
Southern Wall	-2.18	1.48	-6.29	1.57	-2.99	1.90	-8.32	1.37
Leeward* Walls	-1.97	1.51	-6.23	1.72	-2.30	2.01	-7.61	2.29

* Spatially-Averaged pressure across Northern, Southern, and Western walls.

The mean internal pressure $\bar{p}_i$ can be analytically calculated using Equation 2.4, from the mean external pressure and porous opening areas on the windward, side and leeward walls (four external surfaces). The mean internal pressure $\bar{p}_i$ can also be calculated by using the spatially averaged windward wall pressure $\bar{p}_w$ and the Leeward* wall pressure $\bar{p}_L$ (spatially-averaged across the Northern, Southern, and Western walls) (i.e. only two effective external surfaces, Windward and Leeward*) and their respective opening area. The two effective surfaces approach is the principle that simplifies Equation 2.4 into Equation 2.5, that is used by wind loading standards to define the quasi-steady internal pressure coefficients, where $\bar{p}_w \geq \bar{p}_i \geq \bar{p}_L$ is a function of the windward to leeward opening area ratio (A_W/A_L).

Calculation of the mean internal pressure from Table 4.10 using Equation 2.4 (i.e. using all four external surface porous open areas and pressures) for Cases NS1 and NS2 equals $\bar{p}_{i,(Eqn\ 2.4)}$ = 0.32 Pa and 2.52 Pa, respectively. These are 7 % and 4% less than the measured $\bar{p}_i$ for Cases NS1 and NS2 of $\bar{p}_i$ = 0.87 Pa and 2.99 Pa, relative the mean pressure differential across the

Windward and Leeward* surfaces, (i.e. $(\bar{p}_{i,(Eqn\ 2.4)} - \bar{p}_i)/(\bar{p}_w - \bar{p}_L)$). Calculation of the mean internal pressure using Equation 2.5 (i.e. from the spatially averaged pressure across the Leeward* walls) for Cases NS1 and NS2 equals $\bar{p}_{i,(Eqn\ 2.5)}$ = 0.09 Pa and 2.48 Pa, are 10% and 4% less than the measured $\bar{p}_i$, respectively, (i.e. $(\bar{p}_{i,(Eqn\ 2.5)} - \bar{p}_i)/(\bar{p}_w - \bar{p}_L)$).

This assessment shows that the use of detailed open areas and pressure distributions, Equation 2.4 is more accurate than Equation 2.5, as Equation 2.4 accounts for uneven background leakage around the envelope. The calculated mean internal pressure from Equation 2.5 is however considered satisfactory, considering uncertainties with respect to external pressures across envelope.

The mean internal pressure assessment shows that if the envelope was considered uniformly porous (i.e. A_w / A_L = 0.25), the theoretical mean internal pressure equals -1.1 Pa for both Cases NS1 and NS2, from both Equations 2.4 and 2.5. This shows knowledge of the detailed distribution of the background leakage has a significant influence on the estimated internal pressure, further demonstrating the need for the correct assessment of the potential envelopes openings during the assessment of the internal pressure in nominally sealed buildings.

4.5.2. Building with a Large Wall Opening

Another aim was to study the characteristics of large positive internal pressures resulting from a single large windward wall opening. The JCU-ASIS has six potential openings (i.e. wall fitments) in the envelope as noted in Section 4.2.1 and shown in Figure 4.4. As the most frequent winds at the site are from the North-East, these tests were conducted with either the window on the Northern Wall or the roller-door on the Eastern Wall open. External pressure taps around these two openings are used to obtain the external pressure fluctuations at their openings.

Table 4.11 lists the test configurations, detailing the different opening configurations, opening area on each wall, including different Eastern roller-door positions. All large opening tests were conducted with seals above and below the Western roller-door (as in Case NS2). Case NS2 is also presented in Table 4.11 as a closed roller door comparison case.

Table 4.11 Large Opening Cases – Wall Open Areas

Case #	Opening details	Open Area on Wall, m^2				A_w/A_L
		North	East	South	West	
NS2	Nominally sealed	0.09	0.28*	0.10	0.13	0.83
1	Window on North Wall 100% Open	0.55*	0.28	0.10	0.13	1.06
2	Roller-Door on East Wall 12.5% Open	0.09	1.05*	0.10	0.13	3.14
3	Roller-Door on East Wall 25% Open	0.09	1.96*	0.10	0.13	5.84
4	Roller-Door on East Wall 50% Open	0.09	3.47*	0.10	0.13	10.4
5	Roller-Door on East Wall 100% Open	0.09	6.67*	0.10	0.13	19.9

* indicates the windward wall open area, A_w : All other wall open areas are combined into A_L

Table 4.11 also lists the A_w/A_L ratio for each Case, ranging from 0.83 for Case NS2 to about 20 for Case #5. As discussed in Section 2.5, once the external pressure at an opening contributes to about 80% of the mean internal pressure, (i.e. $A_w/A_L \geq 2$), it generally considered dominant. Thus, Cases NS2 and #1 are not considered large openings, and not expected to generate large internal pressures. Whereas, Cases #2 to #5 are expected to generate large internal pressures as A_w/A_L ranges from about 3 to 20, and Equation 2.5 estimates the mean internal pressure equal about 90% to ≈ 100% of the mean external pressure, relative to the differential pressure across the building (i.e. $(\bar{p}_i - \bar{p}_L)/(\bar{p}_w - \bar{p}_L)$).

Further, Table 4.12 lists the cumulated length of stationary wind data and wind speeds that have a mean duration of about 1-minute, and mean wind approach angle θ = 0° ± 30° for Case #1 and θ = 90° ± 30° for the Cases NS2 and Cases #2 to #5.

Table 4.12 Range of Stationary data – Large Opening Cases

Case #	Mean wind speeds, m/s			Minutes of data
	minimum	mean	maximum	
NS2	1.6	3.2	5.7	109
1	2.9	4.2	6.3	14
2	2.0	3.3	6.4	87
3	1.8	3.6	6.8	81
4	1.9	3.6	6.7	85
5	1.9	3.3	6.1	86

Typical time histories of wind speed, approach wind angle, and internal and external pressures for Case NS2 and Cases #1 to #5 are shown in Figure 4.35 to 4.40. Here the external pressure signal from a tap beside the large openings is shown from tap T13 above the North window for Case #1, and for tap T7 beside the Eastern roller door for Cases NS2 and Cases #2 to #5.

Figures 4.39 and 4.40 show that for the larger opening Cases #4 and #5, where A_W/A_L is about 10 and 20 respectively, the mean internal pressures are similar to the external pressure at tap T7 beside the large opening, and attenuated internal pressure fluctuations. Equation 2.5 indicates for a large windward opening (i.e. $A_W/A_L \geq 10$) the mean internal pressure $\overline{p_i}$ is effectively equal to the mean external pressure applied to the opening $\cong 0.99\overline{p_{e,w}}$. The attenuation of the internal pressure response relative to tap T7 is a combination of the area-averaging of the external pressure across the opening, damping due to background leakage, and viscous losses through the opening.

Further, Figures 4.35 to 4.38 show that for Cases NS2, #1, #2, and #3, with A_W/A_L of about 0.8, 1.1, 3, and 6 respectively, the mean internal pressure and pressure fluctuations are significantly lower than the mean external pressure beside the large openings. In these Cases, external suction pressures at the porous openings on the side and leeward walls have a more significant influence on the internal pressure fluctuations at smaller A_W/A_L ratios.

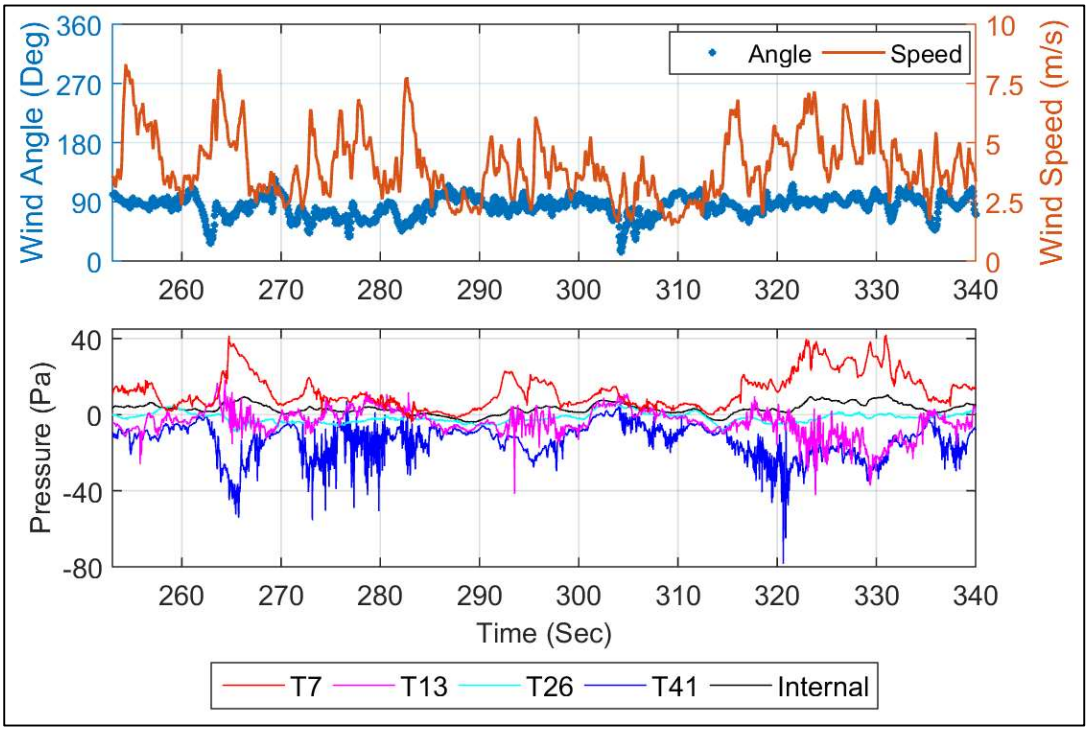

Figure 4.35. Wind speed, wind direction ($\bar{\theta} \cong 90°$); and internal and external point pressures vs time: Case NS2

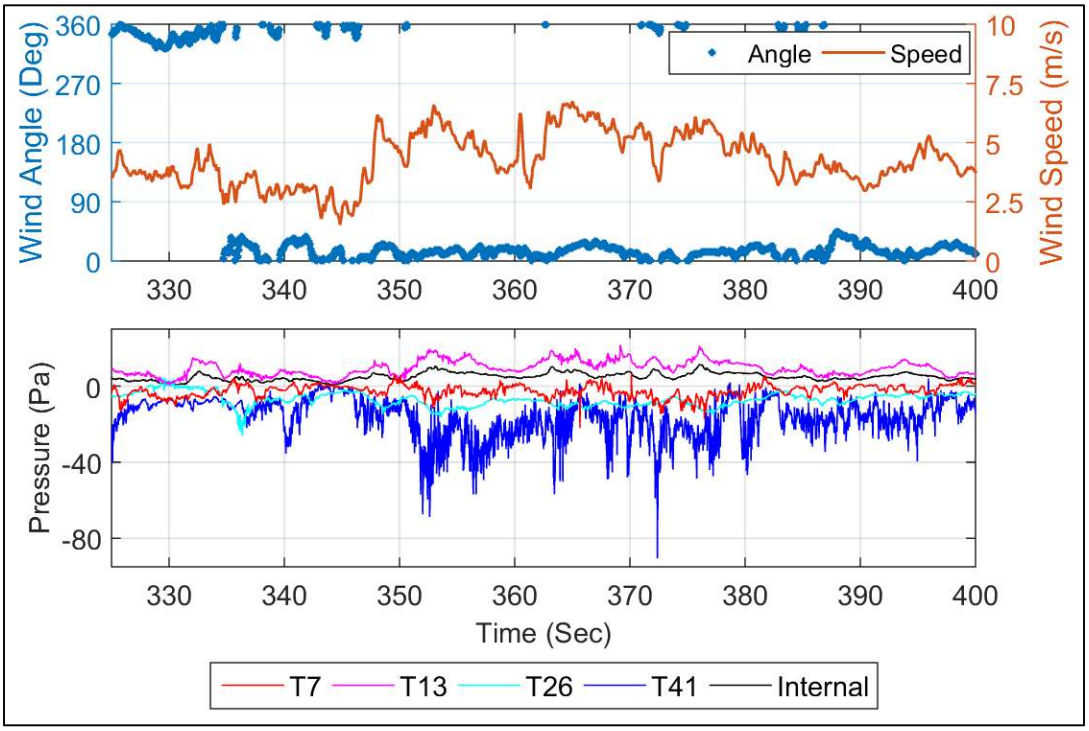

Figure 4.36. Wind speed, wind direction ($\bar{\theta} \cong 0°$); and internal and external point pressures vs time: Case #1

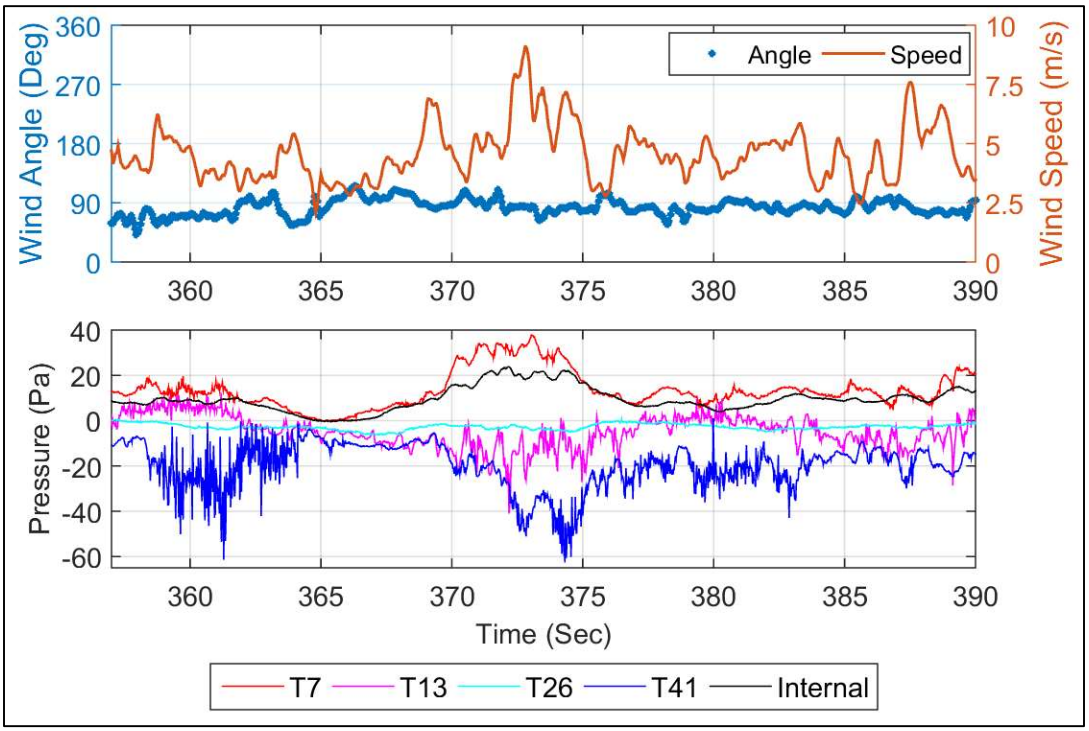

Figure 4.37. Wind speed, wind direction ($\bar{\theta} \cong 90°$); and internal and external point pressures vs time: Case #2

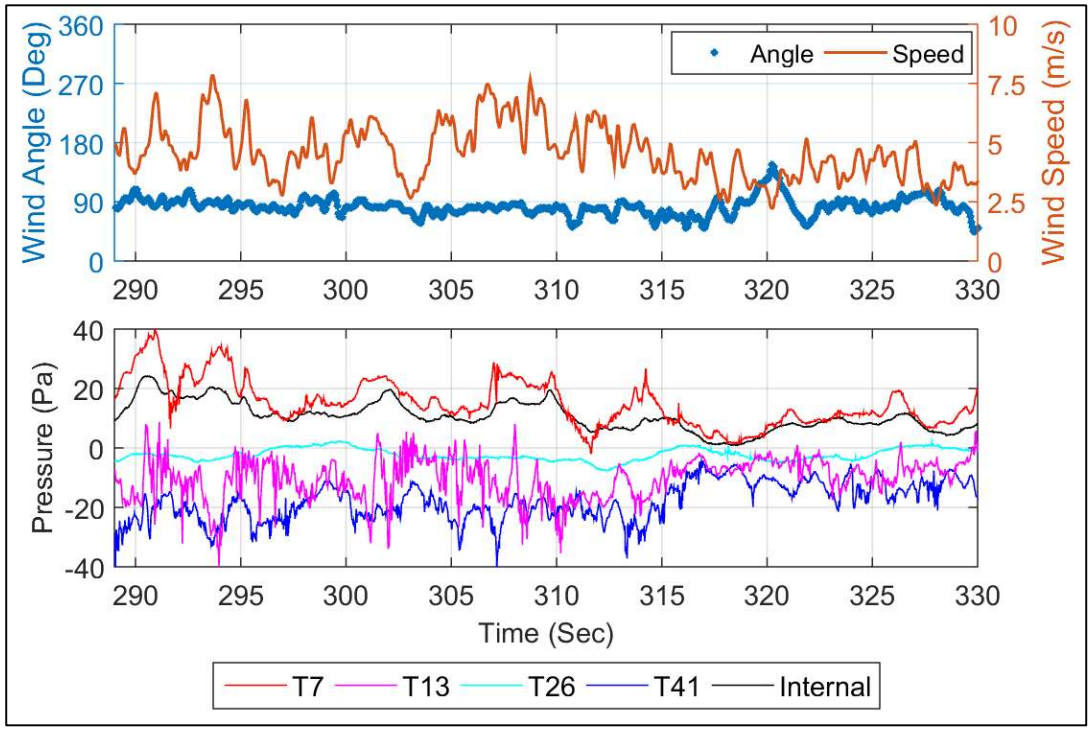

Figure 4.38. Wind speed, wind direction ($\bar{\theta} \cong 90°$); and internal and external point pressures vs time: Case #3

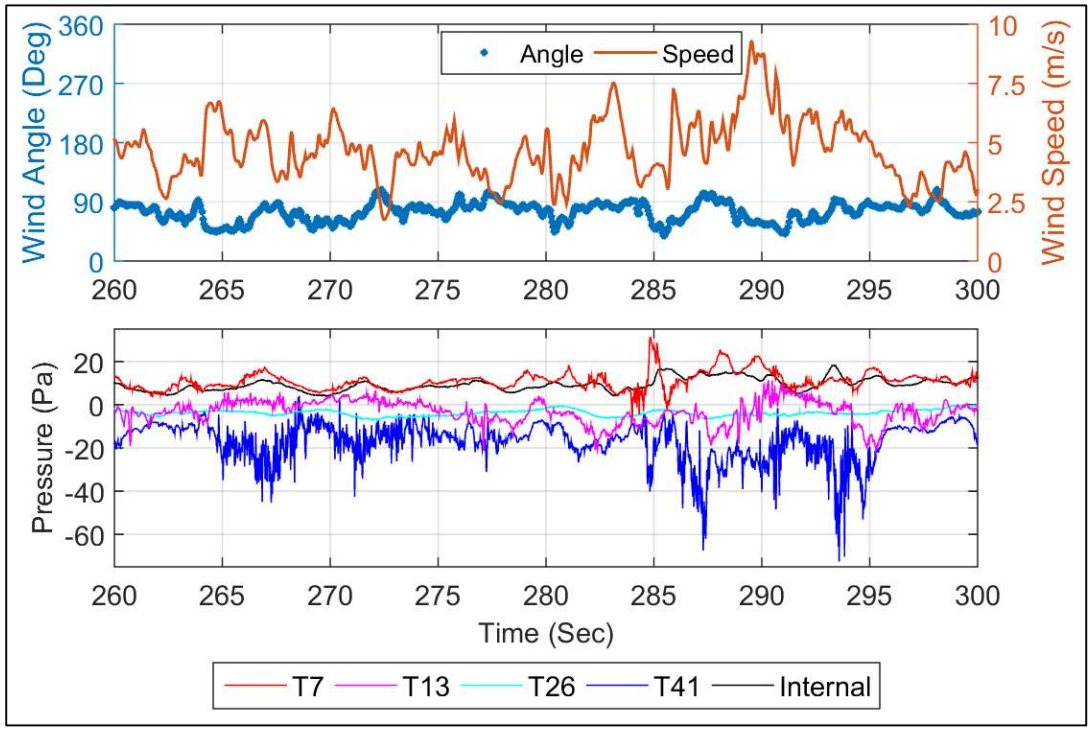

Figure 4.39. Wind speed, wind direction ($\bar{\theta} \cong 90°$); and internal and external point pressures vs time: Case #4

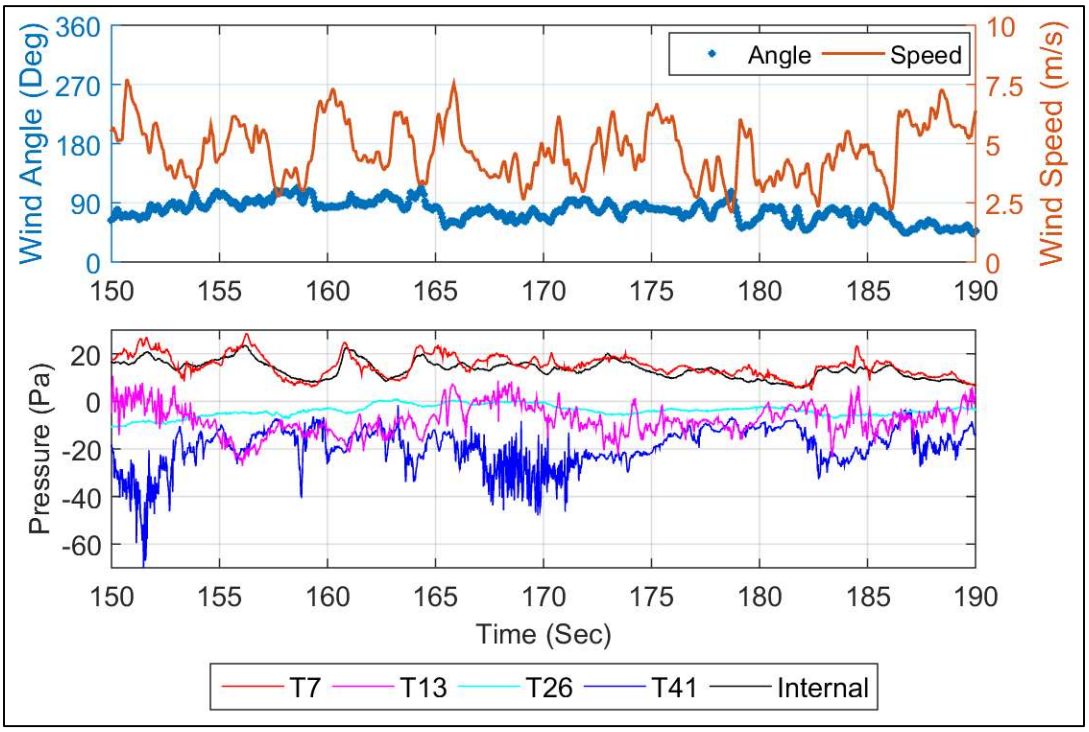

Figure 4.40. Wind speed, wind direction ($\bar{\theta} \cong 90°$); and internal and external point pressures vs time: Case #5

Figures 4.41 to 4.46 show the pressure power spectral densities (i.e. spectra) $S_p(f)$ of the internal and external pressure from taps T7, T13, T26, and T41 for Cases NS2 and Cases #1 to #5. It is noted that the wind direction for Case #1, shown in Figures 4.36 and 4.42, is for $\theta \cong 0°$, is different to all other Cases, where $\theta \cong 90°$.

Figure 4.41 shows internal and external point pressure fluctuations for the Nominally Sealed Case NS2, discussed in Section 4.4.1. The external windward, side and leeward wall pressure spectra in Figures 4.43 to 4.46 (i.e. Cases #2 – #5) with $\theta \cong 90°$ show the same pressure spectra patterns as for the nominally sealed Cases NS1 and NS2 shown in Figure 4.27.

Figure 4.42 shows the pressure spectra on the roof tap T41, where $\theta \cong 0°$, is very similar to Case NS2 where $\theta \cong 90°$, as the pressure tap T41 is 0.6 m from the windward roof edge for both wind approach angles. Further, Figure 4.42 (Case 1, $\theta \cong 0°$) shows the sidewall pressure on T7 and T26 (i.e. 1.5 m from the windward edge, 1.8 m from the ground) have similar spectra to the windward wall tap T13. In comparison, the sidewall pressures for Case NS2 ($\theta \cong 90°$), at tap

T13 (i.e. 1.3 m from the windward edge, 2.1 m from the ground), has greater energy at the higher frequencies (greater than 1 Hz) than the windward wall tap T7; this may be because tap T13 is closer to the windward edge for $\theta \cong 90°$ relative to taps T7 and T26 for $\theta \cong 0°$. These are similar findings to model-scale and full-scale studies by Cermak (1976), where closer proximity to the windward discontinuities sustain greater intermittent building induced pressure fluctuations within the flow separation region.

Figure 4.42 for large opening Case #1 shows the energy in the internal pressure spectra is closer to the windward wall pressure spectra on Tap T13, compared to Case NS2, with significantly more internal pressure energy between 0.5 and 3 Hz, and significantly less than the external pressure on the windward wall.

Figure 4.43 to 4.46 (large opening Cases #2 to #5 respectively) show the energy in the internal pressure spectra $S_{pi}(f)$ below about 1 Hz, is between the windward and leeward wall pressure spectral energy and increases as A_w/A_L increases, due to the greater influence of the windward wall pressure fluctuations. The energy in $S_{pi}(f)$ between 1 Hz and 4 Hz shows greater variations between Cases #2 to #5, with the larger opening Cases #4 and #5 showing an abrupt decrease of internal pressure energy at 3.1 Hz and 3.4 Hz respectively. Cases #2 and #3 show a gradual energy decay. An abrupt decrease in the spectra is typical at the resonant Helmholtz frequency.

The Helmholtz frequencies $f_H = [(a_s/2\pi)\sqrt{(\sqrt{A}/(C_I V))}\,]$ calculated for each of the single large opening cases (Cases #1 to #5) are given in Table 4.13, for the inertial coefficient $C_I = 0.9$ used by several other model and full-scale studies (from potential flow theory) and $C_I = 1.45$ (matched from the Full-Scale Test Enclosure analysis (Section 3.2.1)). Here, A and V is the size of the single large opening area and effective building volume $V = 119 \times (1 + 3) = 476$ m^3.

The calculated Helmholtz frequency from $C_I = 1.45$ is indicated in Figures 4.43 to 4.46. The abrupt decrease in the internal pressure spectra for Cases #4 and #5 at 3.1 Hz and 3.4 Hz are close to the estimated Helmholtz frequency f_H and is confirmation of a highly damped response. The frequencies at the abrupt decay (3.1 Hz and 3.4 Hz) is inferred as Helmholtz frequencies for Cases #4 and #5. The inertial coefficients $C_I = 1.2$ and 1.4 match these f_H values of 3.1 Hz and 3.4 Hz for Cases #4 and #5 respectively, and are within the range of inertial coefficients derived from other previous model-scale and full-scale studies.

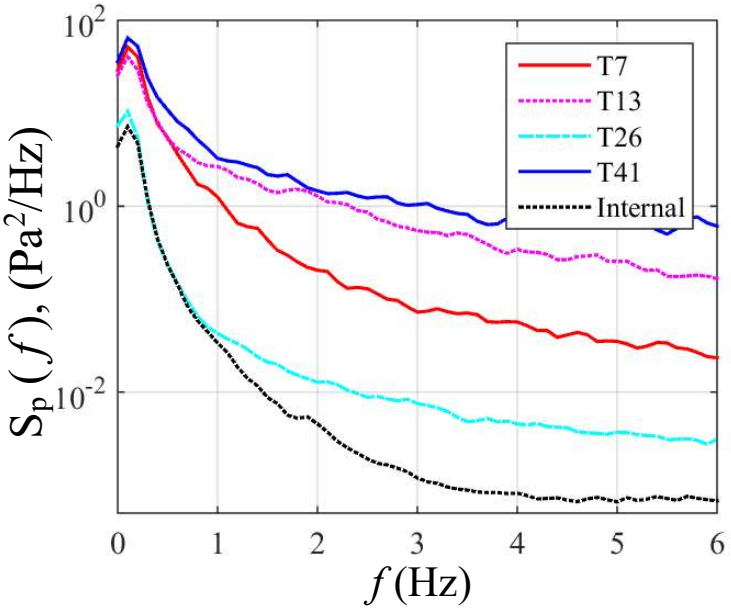

Figure 4.41. Internal and external point pressure spectra vs frequency: Case NS2, $\bar{\theta} \cong 90°$

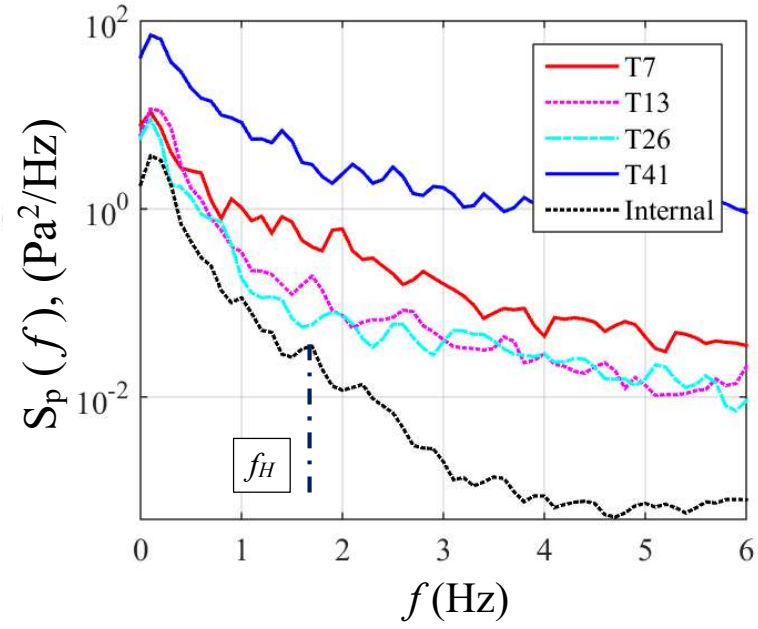

Figure 4.42. Internal and external pressure spectra vs frequency, indicating f_H for $C_I = 1.45$; Case #1, $\bar{\theta} \cong 0°$

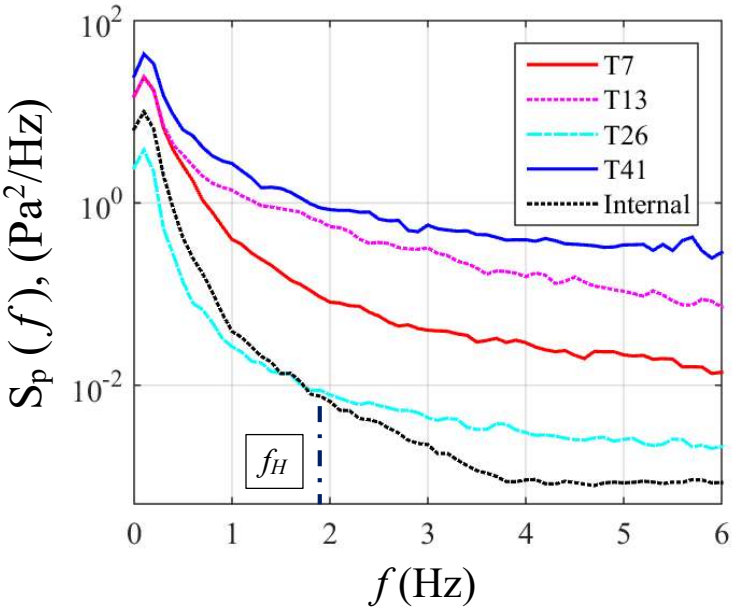

Figure 4.43. Internal and external pressure spectra vs frequency, indicating f_H for C_I = 1.45; Case #2, $\bar{\theta} \cong 90°$

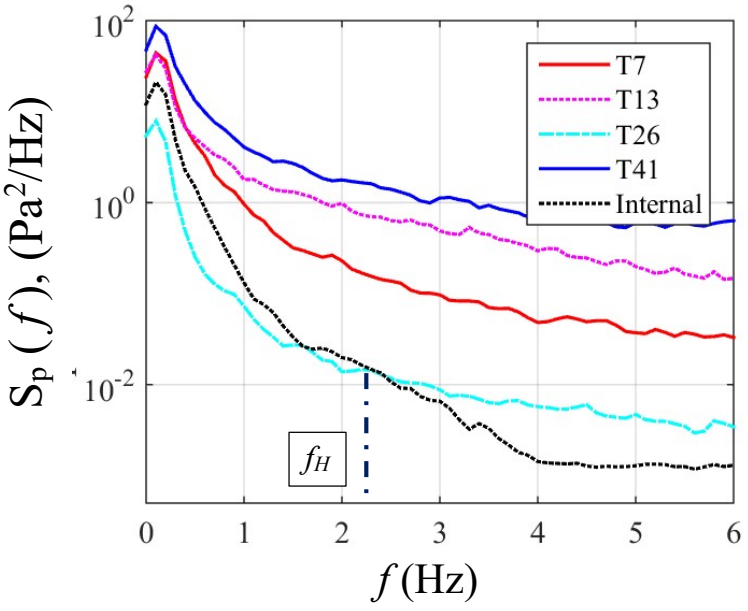

Figure 4.44. Internal and external pressure spectra vs frequency, indicating f_H for C_I = 1.45; Case #3, $\bar{\theta} \cong 90°$

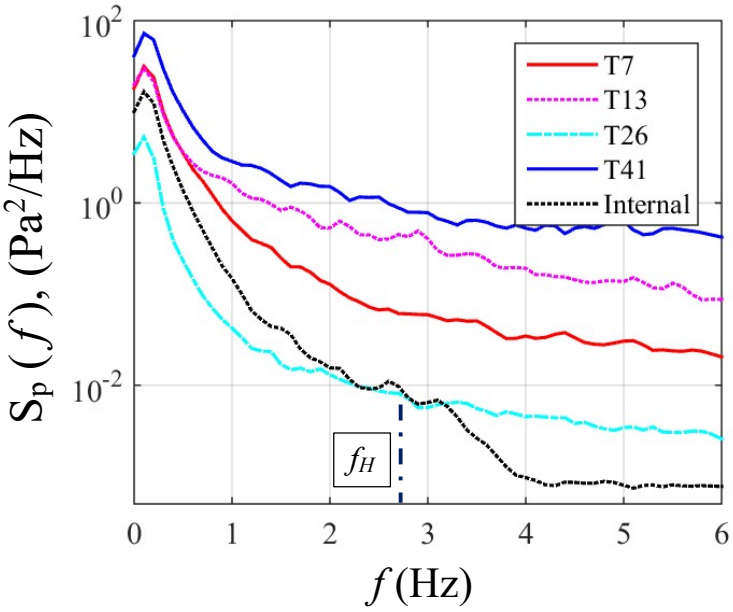

Figure 4.45. Internal and external pressure spectra vs frequency, indicating f_H for $C_I = 1.45$; Case #4, $\bar{\theta} \cong 90°$

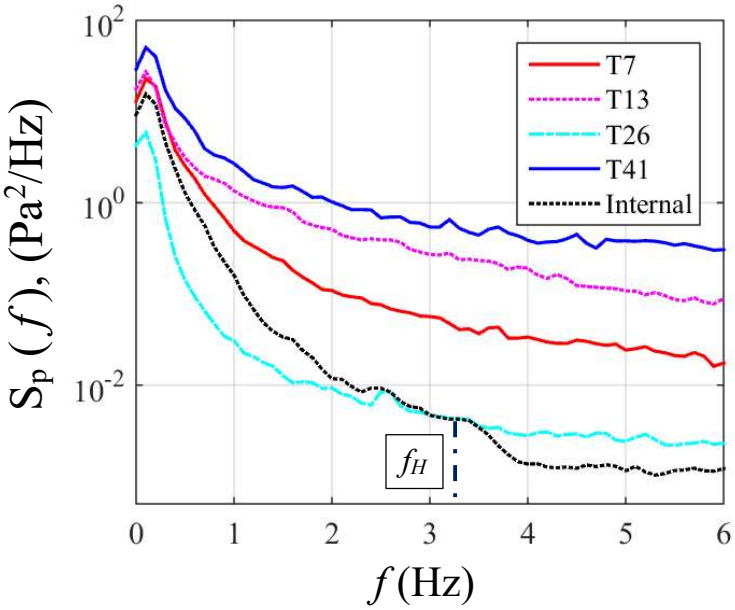

Figure 4.46. Internal and external pressure spectra vs frequency, indicating f_H for $C_I = 1.45$; Case #5, $\bar{\theta} \cong 90°$

Table 4.13 Calculated Helmholtz resonant frequency

Case #	Opening area A, m^2	f_H, Hz ($C_I = 0.9$)	f_H, Hz ($C_I = 1.45$)
1	0.46	2.17	1.71
2	0.83	2.52	1.98
3	1.66	2.99	2.36
4	3.31	3.56	2.81
5	6.62	4.23	3.34

Assessment of the internal pressure relative to the area-averaged external pressure applied to the opening is required to analyse the internal pressure response. As the area-averaged external pressure applied to the large openings cannot be simultaneously captured while the wall fitment is open, the external pressures measured around the wall fitments are used as a means to derive an effective area-averaged external pressure applied across the open wall fitment.

The external pressures around the perimeter of the Eastern roller door (taps T1, T2, T3, T5, T6, T7, and T8) and the Northern window (taps T13 and T14) were assessed to see if the presence of an adjacent opening influences their pressure fluctuations. This analysis is detailed in Appendix E, where pressures around the wall fitments are analysed for each Case (defined in Table 4.11) and compared with the external pressures from the nominally sealed Cases.

The assessment shows for Case #1 (i.e. Northern window (0.55 × 0.83 m)) the opening has a negligible influence on the external pressures adjacent to the opening measured at taps T13 and T14 (above and below the window respectively) for $\theta \cong 0°$. Thus, the spatially averaged

pressure signal from taps T13 and T14 is used as the effective area-averaged external pressure across the open window on the Northern face for the assessment of the internal pressure response in Case #1. Figure 4.47 shows the pressure spectra for tap T13 and the effective external pressure applied to the Northern window for Case #1.

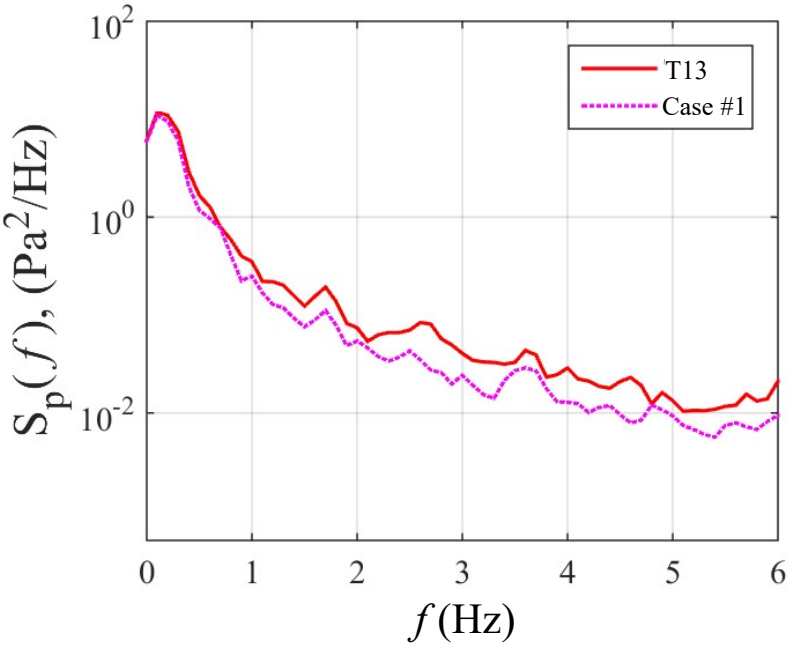

Figure 4.47. Pressure spectra for tap T13 and area-averaged taps T13 and T14 across the window from Case #1, $\bar{\theta} \cong 0°$

The presence of the open Eastern roller door has a greater influence on the adjacent external pressure measurements for $\theta \cong 90°$, further detailed in Appendix E. The analysis shows from the pressures measured around the open roller door, the measurements from tap T7 had the least relative variation between the nominally sealed building and Case #2 to #5. Area-averaged external pressures from the nominally sealed Eastern wall were used to develop transfer functions to apply to tap T7 measurements, for Case #2 to #5, to define effective area-averaged external pressures applied to the open wall fitments for each Case.

Here pressure taps T1, T2, and T8 were used to define the area-averaged pressure signal for Case #2 and #3 (lower portion of the roller door), and weighted proportions of taps T1 to T8 estimate the area-averaged pressure signal for Cases #4 and #5 (roller door open 50% and 100%). The area-averaged external signals from the nominally sealed building were then used to define the transfer functions $|X(f)|^2 = (S_{Area}(f)/S_{T7}(f))$ to apply to pressures measured at tap T7 for Case #2 to #5. Here $S_{Area}(f)$ and $S_{T7}(f)$ are the spectra of the area-averaged and tap T7 pressure fluctuations respectively, shown in Figure 4.48. Figure 4.48 shows that the area-averaged pressure spectral energy is less than the pressure energy on tap T7 across all frequencies, explained by the spatial-averaging of fluctuations at higher frequencies caused by the temporal variation of fluctuations across the Eastern wall. These effective external pressure signals are used for the assessment of internal pressure fluctuations in the following sections.

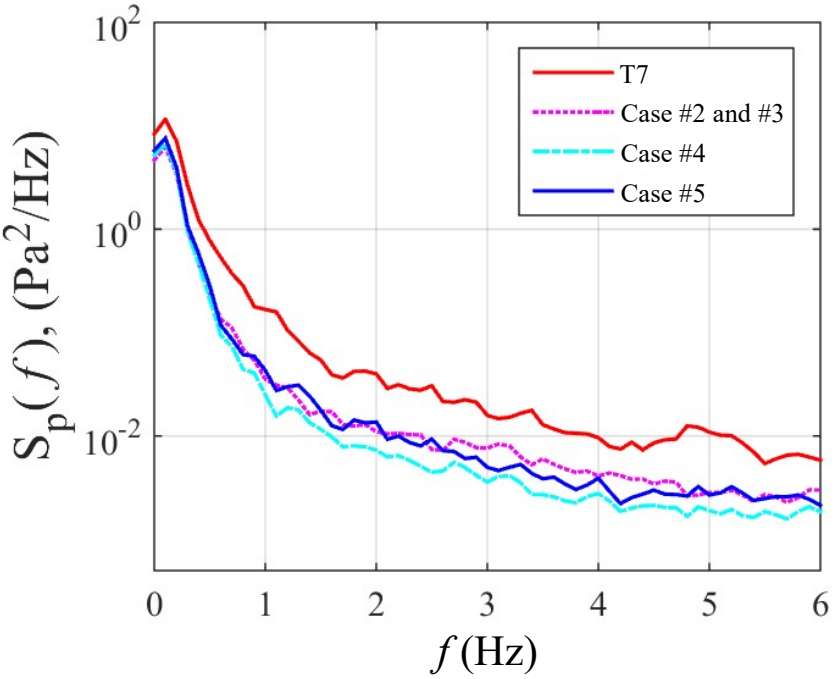

Figure 4.48. Pressure spectra for tap T7 and area-averaged taps across the roller door from Case NS2 for Cases #2 to #5, $\bar{\theta} \cong 90°$

Figures 4.49 to 4.53 show the internal pressure spectra and effective windward wall area-averaged external pressure spectra applied to the large openings for Cases #1 to #5. Figure 4.49 shows the internal pressure fluctuations for Case #1 are significantly damped compared to the area-averaged pressure on the window, due to the low $A_w/A_L \approx 1.1$.

Figure 4.50 (i.e. Cases #2) shows that the internal pressure fluctuations are moderately attenuated between 0.1 Hz to about 1 Hz, followed by steady and significant attenuation beyond 1 Hz, up to about 4 Hz, where the magnitude plateaus at 5×10^{-4} Pa^2/Hz.

Figures 4.51 to 4.53 (i.e. Cases #3 to #5) show that the internal pressure spectra is equal to or marginally attenuated compared to the external pressure fluctuations between 0.1 Hz and 1 Hz, with attenuation increasing beyond 1 Hz. Figures 4.51 to 4.53 also show that the internal pressure spectral energy is greater between about 2 Hz and 4 Hz, than internal pressure spectral energy in Figure 4.50 (i.e. Case #2), this relative increase in energy at the higher frequencies is within the calculated Helmholtz frequency range given in Table 4.13.

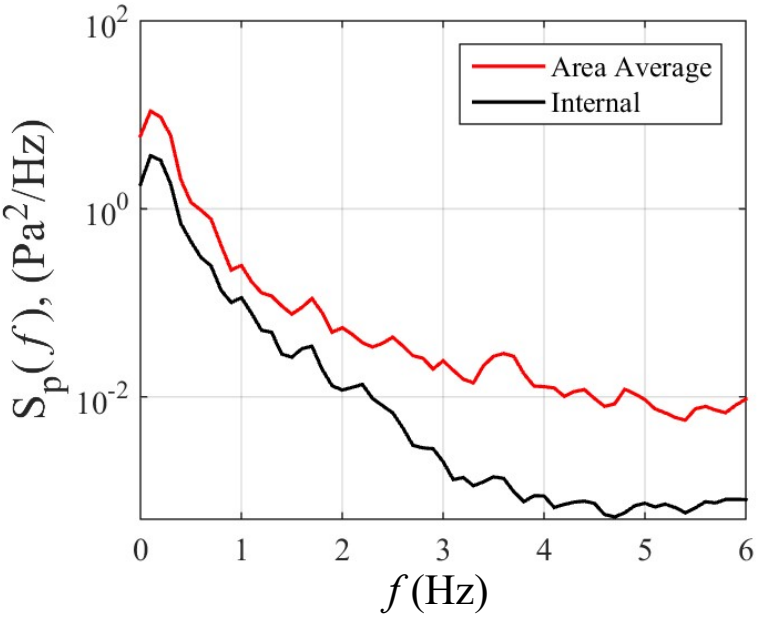

Figure 4.49. Pressure spectra of internal and effective area-averaged external pressure on opening: Case #1, $\bar{\theta} \cong 0°$

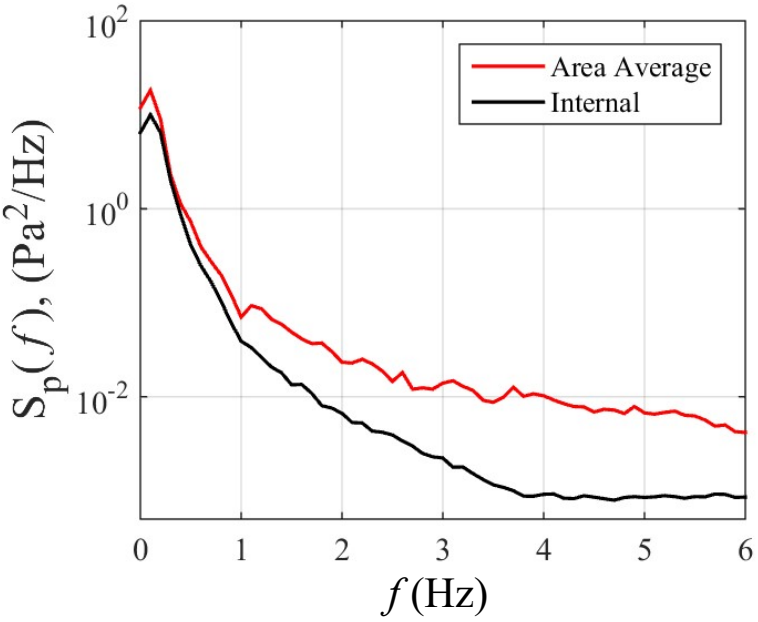

Figure 4.50. Pressure spectra of internal and effective area-averaged external pressure on opening: Case #2, $\bar{\theta} \cong 90°$

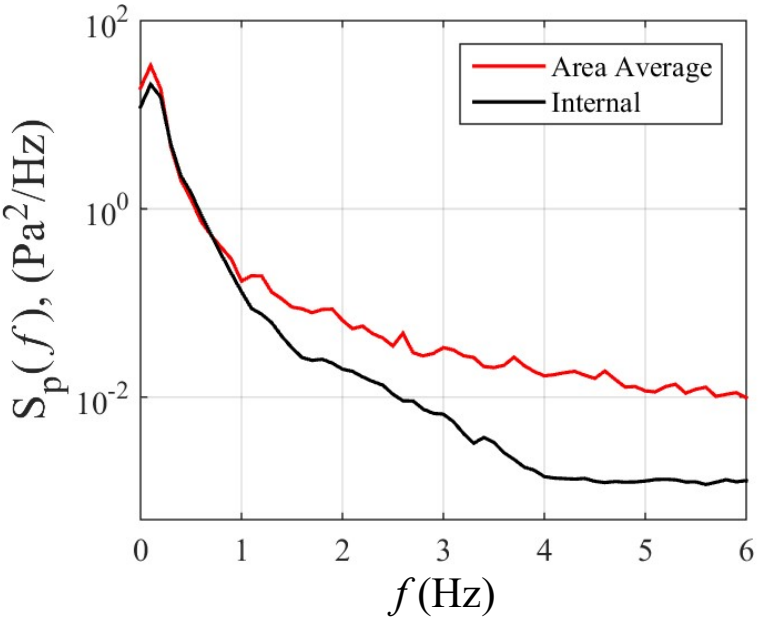

Figure 4.51. Pressure spectra of internal and effective area-averaged external pressure on opening: Case #3, $\bar{\theta} \cong 90°$

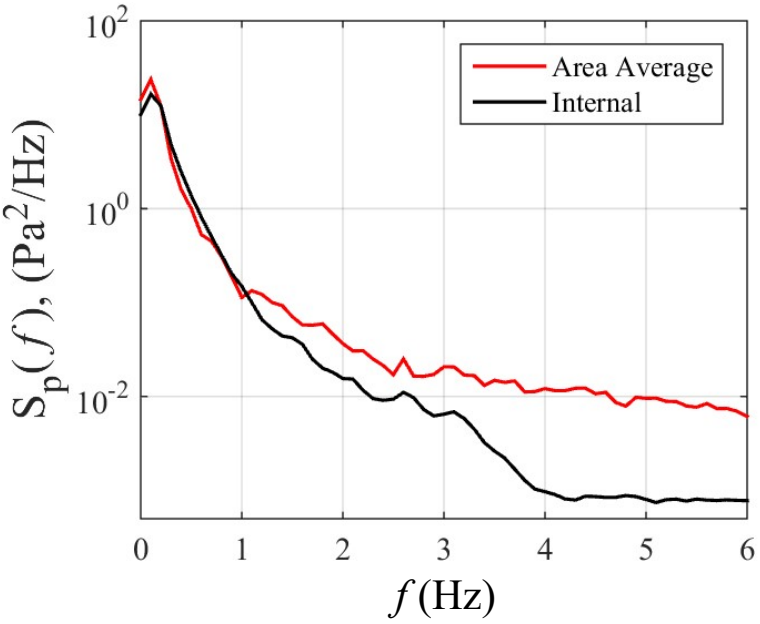

Figure 4.52. Pressure spectra of internal and effective area-averaged external pressure on opening: Case #4, $\bar{\theta} \cong 90°$

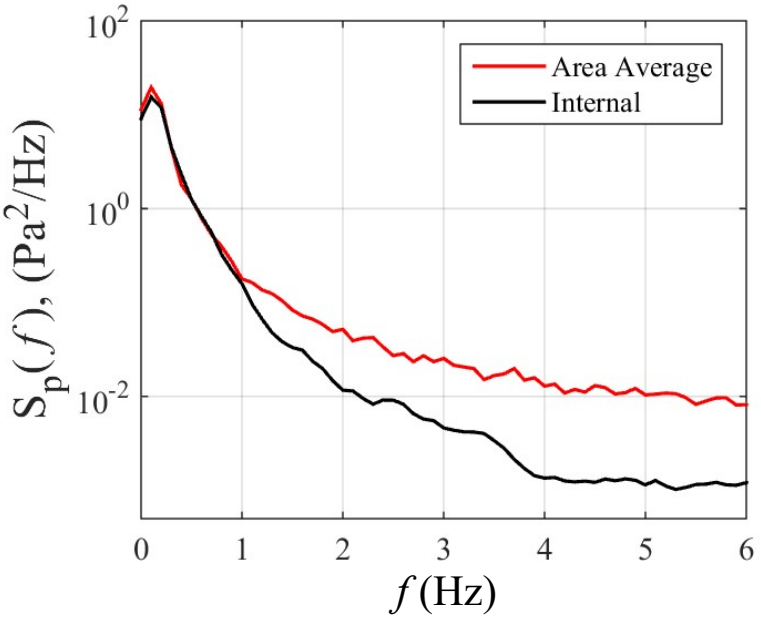

Figure 4.53. Pressure spectra of internal and effective area-averaged external pressure on opening: Case #5, $\bar{\theta} \cong 90°$

4.5.3. Internal to External Pressure Ratios and Peak Pressure Factor

The mean, standard deviation, minimum, and maximum internal pressures are analysed with respect to the area-averaged external pressures applied to the windward and leeward* walls (spatially averaged pressure across the leeward and side walls). The analysis determines if the quasi-static method can be used to satisfactorily estimate the peak internal pressures from peak external pressures for the Nominally Sealed building (Cases NS1 and NS2) and with large openings (Cases #1 to #5).

Table 4.14 presents the mean, standard deviation, minimum, and maximum pressures for the windward wall, leeward* walls, and internal pressure for Cases NS1, NS2 and Cases #1 to #5. Here, the windward wall pressure $p_{e,w}(t)$ for Case #1 is from the area-averaged pressure across tap T13 and T14. For Cases #2 to #5 is the effective area-averaged external pressure applied to the opening (detailed in Section 4.5.2), and for Cases NS1 and NS2 $p_{e,w}(t)$ is the area-averaged pressure across the Eastern wall. The Leeward* wall pressures are the spatially-averaged pressure across the Side and Leeward walls for each Case.

Table 4.14. Mean, Standard deviation, Minimum, and Maximum Effective Windward, Internal, and Leeward* Pressure – All Cases

Case #	Windward Wall Pressure, Pa				Leeward Wall Pressure, Pa				Internal Pressure, Pa			
	$\bar{p}_{e,w}$	$\sigma_{p_{e,w}}$	$\check{p}_{e,w}$	$\hat{p}_{e,w}$	$\bar{p}_{e,L}$	$\sigma_{p_{e,L}}$	$\check{p}_{e,L}$	$\hat{p}_{e,L}$	$\bar{p}_i$	σ_{p_i}	$\check{p}_i$	$\hat{p}_i$
NS1	5.6	2.8	-0.3	14.2	-1.8	1.6	-6.5	2.3	0.8	1.3	-2.6	4.3
NS2	8.4	3.7	0.9	20.4	-1.9	2.1	-7.9	3.3	2.8	1.8	-1.5	7.9
1	7.0	3.0	0.9	18.2	-1.8	1.2	-5.9	0.6	4.0	1.7	0.6	9.8
2	5.8	2.5	-0.5	14.8	-2.5	1.5	-6.8	1.2	5.4	2.3	0.8	12.3
3	7.3	3.2	-0.9	18.6	-2.7	1.8	-8.7	1.6	7.0	3.1	1.2	16.8
4	6.9	2.9	0.0	16.0	-2.8	1.7	-7.7	1.1	6.7	2.8	1.4	15.0
5	7.3	3.1	-0.2	17.4	-2.0	1.7	-6.8	1.9	7.2	3.0	1.7	16.3

The measured mean internal pressure $\bar{p}_i$ can be described as a ratio between the mean external driving pressures (i.e. Windward wall pressure $\bar{p}_{e,W}$ and Leeward* wall pressure $\bar{p}_{e,L}$) as $(\bar{p}_i - \bar{p}_{e,L})/(\bar{p}_{e,w} - \bar{p}_{e,L})$. This ratio of the measured mean internal pressure relative to the measured mean windward to leeward pressure differential can also be derived analytically using Equation 2.5, $\left[\bar{p}_i = \bar{p}_{e,w}/\left(1 + \left(\frac{A_L}{A_w}\right)^2\right) + \bar{p}_{e,L}/\left(1 + \left(\frac{A_W}{A_L}\right)^2\right)\right]$, (where A_w/A_L is known from air-leakage tests). Here the ratio of the mean internal pressure relative to the mean pressure difference between $\bar{p}_{e,W}$ and $\bar{p}_{e,L}$ is $\left([\bar{p}_i - \bar{p}_{e,L}]/[\bar{p}_{e,w} - \bar{p}_{e,L}]\right) = 1/(1 + [A_L/A_w]^2)$. Table

4.15 gives the ratio of the measured and theoretical mean internal pressure relative to the mean windward to leeward pressure differential. This is also shown in Figure 4.54 relative to A_W/A_L. Table 4.15 and Figure 4.54 show that the theoretical mean internal pressures (estimated from Equation 2.5) satisfactorily estimates the experimental mean internal pressures as a function of the windward and leeward opening area ratio. These findings are similar to results by Ginger (2000) for the full-scale TTU WERFL building where the mean internal pressure was satisfactorily estimated by A_w / A_L from Equation 2.5, for known windward and leeward open areas. Table 4.15 and Figure 4.54 show the measured mean internal pressure with respect to the windward and leeward external pressure differential $\left[\left(\bar{p}_i - \bar{p}_{e,L}\right)/\left(\bar{p}_{e,w} - \bar{p}_{e,L}\right)\right]$ is very similar to the mean internal pressure determined from Equation 2.5 for $A_w/A_L \geq 3.14$. This is because the influence of the windward wall pressure is large (i.e. theoretical windward wall component of $\bar{p}_i \geq 0.96\bar{p}_{e,w}$).

For A_w/A_L between 0.58 and 1.06, the theoretical influence of the leeward wall pressure is greater than the measured influence due to the leeward* wall pressure distribution across the uneven background leakage (i.e. greater leakage on the Western (leeward) wall relative to the Northern and Southern (side) walls). Where the leeward* wall pressure is the spatially average pressure across the three leeward walls and does not account for the uneven leakage area. These results are similar to the nominally sealed building, in Section 4.5.1, where estimation of the mean internal pressure was more accurate when the uneven background leakage is considered in the analysis. However, Equation 2.5 is considered a good estimate for $\bar{p}_i$ when $\bar{p}_{e,w}$, $\bar{p}_{e,L}$, and A_w /A_L are known.

Table 4.15. Mean internal pressure relative to Windward and Leeward* wall pressure differential for all Cases – Theoretical and Measured windward wall pressure contribution

Case #	A_w/A_L	Theoretical	Measured
NS1	0.58	0.25	0.35
NS2	0.83	0.41	0.46
1	1.06	0.55	0.66
2	3.14	0.91	0.96
3	5.84	0.97	0.98
4	10.4	0.99	0.98
5	19.9	1.00	0.99

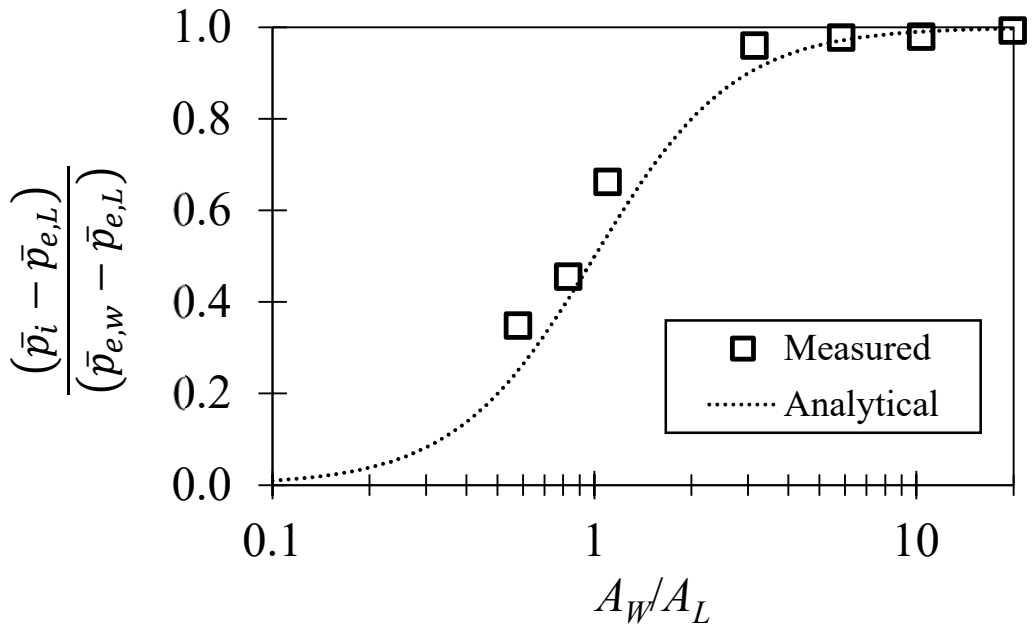

Figure 4.54. Measured and theoretical mean internal pressure relative to mean external Windward and Leeward wall pressure differential vs A_w/A_L

The mean internal pressure $\bar{p}_i$ (i.e derived from Equation 2.5) is used to define quasi-steady internal pressure coefficients $\tilde{C}_{pi}$ (i.e. $\tilde{C}_p \cong \bar{C}_p = \bar{p}/[½\rho\overline{U}_h^2]$) given in wind loading standards, such as AS/NZS 1170.2 (2011) and ASCE 7 (2011). AS/NZS 1170.2 (2011) defines peak (i.e. design) internal pressures (and external pressures) with respect to a 0.2-second peak design wind speed $\widehat{U}_h$ (at mid-roof-height), where $\hat{p}$ (or $\check{p}$) = $\tilde{C}_p ½\rho\widehat{U}_h^2$, as detailed in Section 2.9.4. Here, the quasi-steady approximation infers that pressure fluctuations follow the approach wind velocity fluctuations and that the ratio of the peak to mean pressure (peak pressure factor G_p = $\hat{p}/\bar{p}$) is equal to the velocity gust factor squared $\left(\widehat{U}_h/\overline{U}_h\right)^2$.

Further, AS/NZS 1170.2 (2011) considers internal pressure fluctuations as quasi-static (i.e. ignores amplification and attenuation of internal pressure fluctuations), thus applies the same peak pressure factor $G_p = \left(\widehat{U}_h/\overline{U}_h\right)^2$ to internal and external pressures (i.e. $(\hat{p}_i/\bar{p}_i) = (\hat{p}_e/\bar{p}_e)$). Therefore, the quasi-steady methodology applies an equal G_{pi} for all internal pressures, and $\hat{p}_i$ = $G_{pi} \times \bar{p}_i$, where $\bar{p}_i$ is a function of A_w/A_L (i.e. Equation 2.5). When $\bar{p}_i$ is near zero (i.e. around $0.5 < A_w/A_L < 1$), wind loading standards apply a minimum range of peak internal pressures ($\hat{p}_i$ and $\check{p}_i$) to overcome this issue.

The amplification and attenuation of the peak internal pressure can be characterised by the change in the peak internal pressure factor G_{pi}. The quasi-steady peak pressure factors can be presumed to be equal to the peak pressure factor from the external pressure applied to the windward openings $G_{pe,w}$. The assumption that for a quasi-static internal pressure response would produce $G_{pi} = G_{pe,w}$, is considered suitable as both the external pressure across the opening and the internal pressure are both subjected to the attenuation of higher frequencies from the spatial-averaging across the opening. Thus, any change in G_{pi} relative to $G_{pe,w}$ will be from the amplification or attenuation from inertial effects and viscous losses of the flow through large openings and damping from the background leakage.

Table 4.16 shows G_{pi}, $G_{pe,w}$, and the ratio between the internal and external peak pressure factors $G_{pi}/G_{pe,w}$, for Cases NS1, NS2 and Cases #1 to #5, from the mean and peak pressures from Table 4.14, where the windward wall peak pressure factor is about 2.5. This is similar to the quasi-steady gust factor (i.e. velocity gust factor squared) in AS/NZS 1170.2 (2011) for Terrain Category 2 at a 5 m height of $2.95 = 1.72^2$. Here the shorter mean run length of about 1-minute

and natural variation of wind direction during stationary runs would contribute to reduced peak pressure factors compared a longer windstorm.

For the large opening Cases #2 to #5 where $A_w/A_L > 2$ (i.e. $A_w/A_L = 3.14$, 5.84, 10.4, and 19.9), Table 4.16 shows G_{pi} is 12%, 7%, 3%, and 6% less than $G_{pe,w}$ respectively, with attenuation increasing from A_w/A_L =10.4 to 3.14 (i.e. quasi-static approximation is conservative relative to JCU-ASIS measurements). For $A_w/A_L < 2$, (i.e. not a large opening) for Case #1, $A_w/A_L = 1.06$ and $G_{pi} = 0.94G_{pe,w}$ and Cases NS2 and NS1 (i.e. $A_w/A_L = 0.83$ and 0.58) equal $1.16G_{pe,w}$ and $2.22G_{pe,w}$. Here, $G_{pi}/G_{pe,w} > 1$ as the mean internal pressures is small relative to the internal pressure fluctuations, which is anticipated for A_w/A_L around 0.5 to 1. The quasi-steady internal pressure coefficient is corrected for in wind loading standards.

Table 4.16. Internal and external windward wall opening peak pressure factors for the Nominally Sealed and Large Opening Cases

Case #	A_w/A_L	G_{pi}	$G_{pe,w}$	$G_{pi}/G_{pe,w}$
NS1	0.58	5.59	2.54	2.20
NS2	0.83	2.82	2.43	1.16
1	1.06	2.44	2.60	0.94
2	3.14	2.27	2.57	0.88
3	5.84	2.38	2.56	0.93
4	10.4	2.25	2.33	0.97
5	19.9	2.26	2.39	0.94

The attenuation of the peak internal pressures for the large opening Cases #2 to #5 (where $A_w/A_L \geq 3.14$), is a combination of the influence from the inertial effects and viscous energy losses of the flow through the large opening, described by the Helmholtz resonator model, and additional damping from the background leakage. Previous studies (Vickery and Bloxham (1992), Womble *et al.* (1995), Pearce and Sykes (1999), Oh *et al.* (2007), Ginger (2000), Guha *et al.* (2013b), etc.) typically analyse the mean, standard deviation, and peak internal pressure generated from large openings with respect to the external pressure fluctuations applied to the large opening (i.e. $A_w/A_L \geq 2$).

Table 4.17 lists the mean, standard deviation, and peak internal to external pressure ratios. Here, both $\sigma_{pi}/\sigma_{pe,w}$ and $\hat{p}_i/\hat{p}_{e,w}$ are less than $\bar{p}_i/\bar{p}_{e,w}$, which also highlights the attenuation relative to a quasi-static response as $[\hat{p}_i/\hat{p}_{e,w}]/[\bar{p}_i/\bar{p}_{e,w}]$ equals $G_{pi}/G_{pe,w}$. Where both $\sigma_{pi}/\sigma_{pe,w}$ and $\hat{p}_i/\hat{p}_{e,w}$ range from about 0.90 to 0.96 and 0.83 to 0.94 for Cases #2 to #5 respectively.

Table 4.17. Internal to windward external pressure ratios – large opening Cases ($A_w/A_L > 2$)

Case #	A_w/A_L	$\bar{p}_i/\bar{p}_{e,w}$	$\sigma_{pi}/\sigma_{pe,w}$	$\hat{p}_i/\hat{p}_{e,w}$
2	3.14	0.942	0.901	0.830
3	5.84	0.969	0.959	0.901
4	10.4	0.970	0.961	0.938
5	19.9	0.991	0.964	0.936

The internal pressure response in the JCU-ASIS is compared to previous model-scale and full-scale studies, and the Full-Scale Test Enclosure (FSTE) (i.e. Section 3.2 and Humphreys *et al.* (2019)) in the following Section.

4.5.4. Comparison With Other Previous Studies

As detailed in Sections 2.4, 2.5, and 2.7, previous model-scale studies by Vickery and Bloxham (1992), Yu *et al. (2006),* Ginger *et al. (2008, 2010),* and Guha *et al. (2011b)* have shown the internal pressure response in a building with a single windward wall opening can be described by a non-dimensional Helmholtz resonator model (Equation 2.13). Here the internal pressure response is described by opening area to building volume parameter $S^* = \left(A^{3/2}/V\right)(a_s/\overline{U}_h)^2$ and integral length-scale of turbulence to opening area parameter $\Phi_5 = \lambda_u/\sqrt{A}$. The S* and Φ_5 values for the large opening Cases #2 to #5 (i.e. $A_W/A_L > 2$) are given in Table 4.18.

A_w is the large windward opening area, V is the effective building volume = 476 m^3, $\overline{U}_h$ is the mean wind speed at mid-roof-height (≅ 5 m tower measurement), a_s is the speed of sound ≈ 340 m/s, and λ_u is the integral length-scale of turbulence ≅ 35 m, detailed in Section 4.2.5. Here, S* and Φ_5 range from 24 to 390 and 34 to 14 respectively. A typical low-rise building may have an S* ≈ 20 (i.e. between 0.045 and 375) and Φ_5 ≈ 35 (i.e. between about 20 and 70) under a range of windstorm conditions (Sharma (2013)).

Table 4.18. Windward open area A_w, mean wind speed $\bar{U}$, and non-dimensional parameters S^* and Φ_5 for Large opening Cases #2 to #5

Case #	A_w, m^2	$\bar{U}$, m/s	S^*	Φ_5
2	1.05	3.3	24	34
3	1.96	3.6	52	25
4	3.47	3.6	123	19
5	6.67	3.3	390	14

Model-scale studies of single large openings by Vickery and Bloxham (1992), Yu et al. (2006), Ginger *et al.* (2008, 2010), Guha *et al.* (2011b), and Holmes and Ginger (2012) have shown that internal pressure fluctuations (i.e. both $\sigma_{pi}/\sigma_{pe,w}$ and $\hat{p}_i/\hat{p}_{e,w}$) increase as S* increases and to a lesser extent, as Φ_5 decreases. These model-scale findings have recorded similar trends as the full-scale TTU WERFL building study by Ginger *et al*. (1997), where Helmholtz resonance was present for 1%, 2%, and 5% windward wall openings (S* = 0.62, 1.74, and 6.9). As S* increased, the magnitude of the resonant response increased, and the peak internal pressure was approximately equal to or less than the peak windward external pressure, ($0.96 \leq \hat{p}_i/\hat{p}_{e,w} \leq 1$, with $G_{pi}/G_{pe,w} \cong 1$).

These findings were also validated from the Full-Scale Test Enclosure (FSTE) results in Section 3.2, that examined a wider range of S* values ($0.06 \leq S^* \leq 5.8$) that are within the typical full-scale range, at Φ_5 values larger than a typical full-scale building ($\Phi_5 > 500$). The FSTE observed resonance at Helmholtz frequency for $S^* \geq 0.88$ (similar to Ginger *et al*. (1997)). Here $\hat{p}_i/\hat{p}_{e,w} < 1$ occurs for $S^* \leq 0.75$; $\hat{p}_i/\hat{p}_{e,w} \approx 1$ for $S^* \approx 0.9$, and $\hat{p}_i/\hat{p}_{e,w} > 1$ for $S^* \geq 1.9$. Here $\hat{p}_i/\hat{p}_{e,w} = G_{pi}/G_{pe,w}$ as $\bar{p}_i = \bar{p}_{e,w}$ for a single building opening.

In comparison, model-scale studies that have analysed internal pressure with and without background leakage, such as Vickery and Bloxham (1992), Womble *et al.* (1995), Pearce and Sykes (1999), Oh *et al*. (2007), Yu *et al*. (2008), Kim and Ginger (2013), and Guha *et al*. (2013b); have shown that damping from background leakage has a greater influence on buildings with smaller volume and larger opening area (i.e. increasing S*). This is because the damping is otherwise low when S* is large; as S* decreases, the damping in the system increases, attenuating the internal pressure response, thus the proportion of damping from background leakage decreases.

The model-scale tests by Vickery and Bloxham (1992) with S* < 9, concluded that porosity leeward openings (background leakage) has a minor influence on the internal pressure fluctuations for $A_w/A_L \geq 10$, however significantly reduces internal pressures relative to the windward external pressure fluctuations for $A_w/A_L \leq 3$. Further, Yu *et al.* (2008) validated an internal pressure model, with wind tunnel experiments, that accounts for background leakage. The model by Yu *et al*. (2008) shows that for $A_w/A_L > 20$, there is less than a 5% reduction in the internal pressure fluctuations σ_{pi} compared to the internal pressure fluctuations without porous openings σ_{pi} (i.e. $A_w/A_L = \infty$) for S* = 3 to 33. However, as A_w/A_L decreases to 10, the reduction increases from 2.5% to 7.5% for S* = 3 to 33 respectively, with a similar trend that background leakage has a greater damping influence at greater S* values as damping is otherwise low, and Helmholtz resonance is more pronounced.

Other full-sale studies by Fahrtash and Liu (1990) and Guha et al. (2013a) also conducted internal pressure measurements in porous and flexible buildings. Fahrtash and Liu (1990) conclude that the additional damping effects of the envelope flexibility and background leakage, in the buildings examined (i.e. UMC Observatory and a Missouri residential garage), attenuated Helmholtz resonance and significantly damped internal pressure fluctuations (i.e. $C_{\sigma pi}/C_{\sigma pe,w}$ = 0.4 and 0.24). Guha *et al*. (2013a) also showed that internal pressure fluctuations and Helmholtz resonance were attenuated in a warehouse due to the background leakage ($A_L \cong 10\%$ of the 21 m^2 roller door) and envelope flexibility for oblique windward openings. The study by Guha *et al*. (2013a) shows S* in the range of about 25 and 200, from which $C_{\sigma pi}/C_{\sigma pe,w}$ and $\hat{C}_{pi}/\hat{C}_{pe,w}$ were primarily in the range of about 0.85 to 1.05 and 0.7 to 1.0 respectively.

The internal to external standard deviation and peak pressure ratios ($\sigma_{pi}/\sigma_{pe,w}$ and $\hat{p}_i/\hat{p}_{e,w}$) from the windward dominant openings Cases #2 to #5 are shown in Figure 4.55 and 4.56 vs S* along with the full-scale windward wall opening studies by Fahrtash and Liu (1990), WERFL building by Ginger (1997), and FSTE (Section 3.2). Here, the results from the FSTE and Ginger (1997) have minimal background leakage (i.e. $A_L \cong 0$), $\Phi_5 > 70$, and S* values between 0.19 and 6.9. In comparison, the JCU-ASI Shed has background leakage, smaller Φ_5 values ($34 > \Phi_5 > 14$), and larger S* values ($24 \geq S^* \geq 390$). Here the additional damping from envelope flexibility is incorporated in S* for both the WERFL building and the JCU-ASI Shed.

Figures 4.55 and 4.56 show that although S* is large during the JCU-ASIS tests (i.e. upper bound of typical S* values), internal pressure fluctuations and peak pressures are attenuated by the background leakage.

It is also noted that $\hat{p}_i/\hat{p}_{e,w}$ from a single large windward opening, like that of the WERFL Building and FSTE, is not equivalent to $\hat{p}_i/\hat{p}_{e,w}$ from the JCU-ASIS (due to $\bar{p}_i/\bar{p}_{e,w} < 1$ because of the background leakage). An appropriate comparison of the peak pressure response is a comparison of the peak internal to external pressure factors G_{pi} / G_{pe}, as peak pressure factors account for the variation in the mean internal pressure as A_w /A_L changes, further G_{pi} / G_{pe} = $\hat{p}_i/\hat{p}_{e,w}$ for a single opening.

Where the JCU-ASIS internal peak pressure factor is attenuated by 3% to 12% relative to the external peak pressure factor, as S* decreases from 123 to 24 respectively.

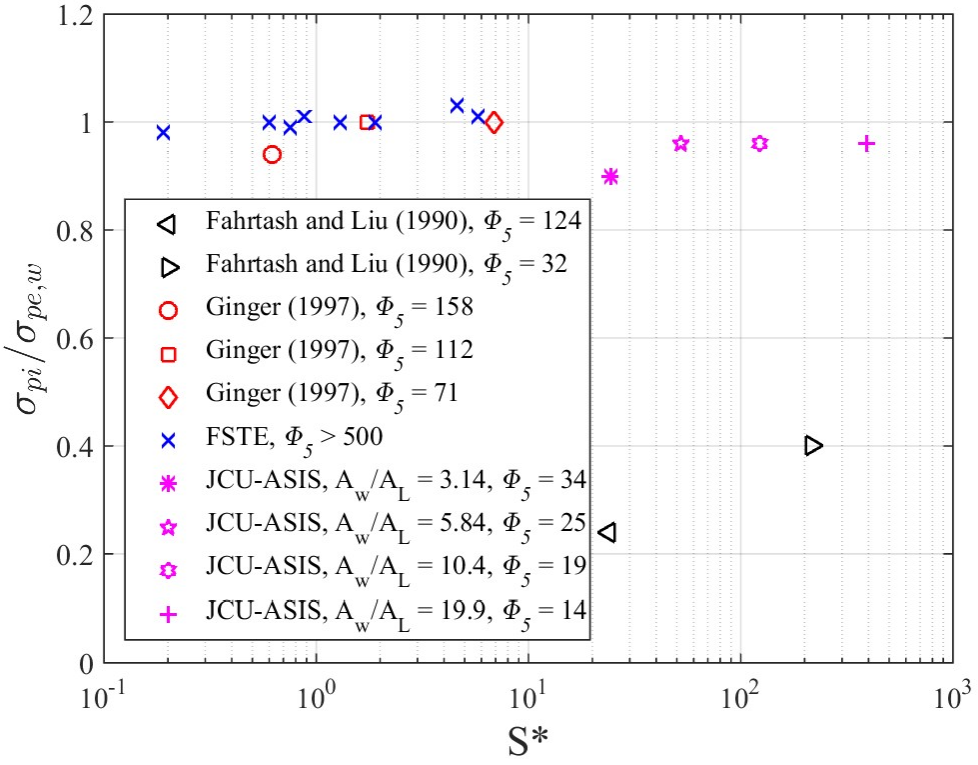

Figure 4.55. Internal to external standard deviation pressure ratio from the JCU-ASIS, FSTE, and other previous full-scale studies

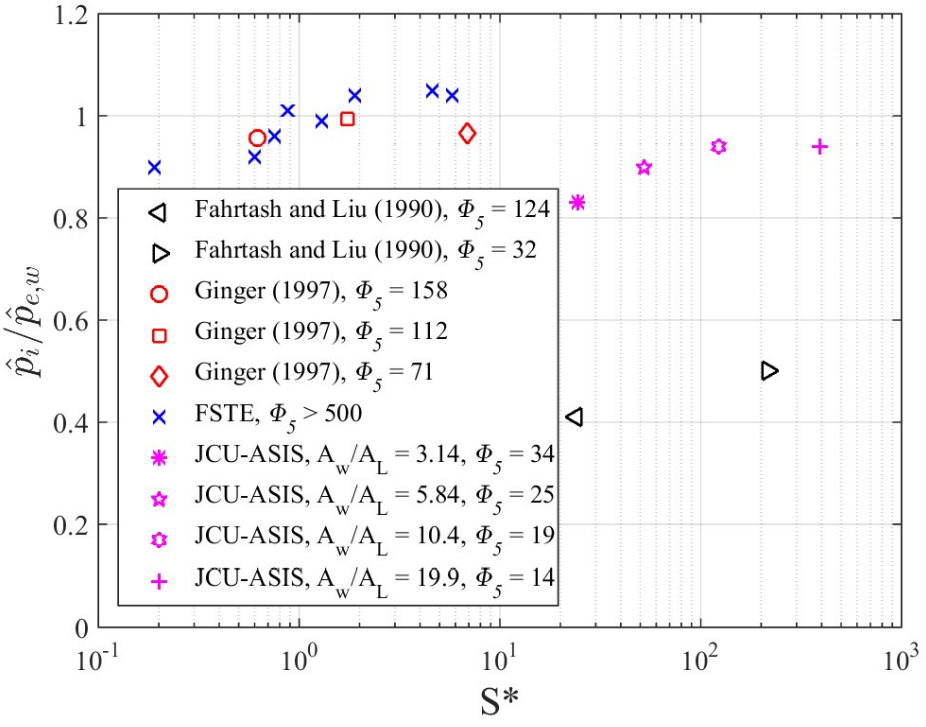

Figure 4.56. Internal to external peak positive pressure ratio from the JCU-ASIS, FSTE, and other previous full-scale studies

The examination of the JCU-ASIS internal pressure response from large windward wall openings, was conducted at the upper bound of typical S* values due to the moderate wind speeds and building volume (typical building S* values: 0.045 – 375, JCU-ASIS S* values: 24 – 390).

The assessment of variable wind speeds on the internal pressure response was detailed by Sharma (2013), who modelled the internal pressure response at two full-scale wind speeds, for three length-scales (including full-scale). Sharma (2013) showed that experiments at lower wind speeds lead to an overestimation of the internal pressure response. However, analysing the results in terms of S* would account for these variations. Thus, the assessment of the internal pressures in the JCU-ASIS at typical S* values (i.e. greater wind speeds) is expected to produce greater attenuation of the internal pressure response.

4.5.5. Summary and Conclusions

A full-scale study on the wind-induced internal pressure fluctuations was conducted on the James Cook University – Australian Steel Institute Shed (JCU-ASIS). The study involves three experimental procedures. Firstly, air-leakage tests carried out to determine the distribution of background leakage around the building envelope. Secondly, the envelope flexibility/effective building volume of the JCU-ASIS were calculated. Thirdly, the measurements of wind-induced internal and external pressures were carried out on the Nominally sealed JCU-ASIS (Cases NS1 and NS2) and JCU-ASIS with a large windward wall opening (Cases #1 to #5). The results provide unique full-scale internal pressure data to assess the internal pressure response in a typical industrial building with respect to analytical methods and other previous model-scale and full-scale studies.

The air-leakage tests accurately defined the area and distribution of background leakage around the envelope. The results show the total porosity of the nominally sealed JCU-ASIS is about 1% of the total wall area, which is greater than other building types, and particularly greater

than buildings in temperate climates. The air-leakage test results can be used to describe the background leakage in other industrial type buildings.

The JCU-ASIS envelope deformation was measured at several locations during pressurization of the building, to calculate the bulk modulus of the building. With the effective volume ≅ 4 times the standard building volume, equal to about 476 m^3.

The mean internal pressure in the JCU-ASIS can be estimated analytically if the area and distribution of building openings are known. The internal pressure fluctuations in the nominally sealed JCU-ASIS are small in comparison to external pressures and increase as the windward to leeward opening area increases. The characteristic frequency f_c increases as the windward to leeward opening area increased, where frequencies above f_c are attenuated as they pass through the envelope.

Further, the internal pressure fluctuations in the JCU-ASIS from a large windward wall opening are significantly attenuated relative to the external pressures applied to the opening due to added damping from the background leakage. Where the background leakage attenuates peak internal pressures by 3% (at S* ≅ 120) to 12% (at S* ≅ 24), relative to the quasi-static method used in wind loading codes and standards. Background leakage is also shown to significantly damp Helmholtz resonance.

CHAPTER 5: CONCLUSIONS AND RECOMMENDATIONS

Internal pressures can apply significant loads on industrial buildings during a windstorm, thus internal pressures must be satisfactorily estimated to enable their optimal structural design. The quasi-static approximation used by wind loading standards fails to account for parameters that amplify or attenuate internal pressure fluctuations. These parameters have been studied previously by model-scale wind tunnel tests and analytical techniques.

The aim of this thesis was to assess the influence of these critical parameters on the internal pressures in a full-scale industrial building. This was motivated by a lack of full-scale data to validate previous model-scale and analytical studies that show conditions where the quasi-static approach does not adequately describe peak (i.e. design) internal pressures.

Two full-scale studies were conducted under natural wind conditions; (i) A sealed 2.4 × 2.5 × 6 m controlled Full-Scale Test Enclosure (FSTE), with a range of single windward wall openings (ii) A typical 6 × 6 × 3 m Industrial Building (JCU-ASIS) with and without large windward wall openings. Further, the porosity and flexibility of the JCU-ASIS envelope were determined by pressurizing the building. These studies provide a unique set of full-scale test data that were used to validate analytical methods and model-scale studies. The results are also represented non-dimensionally, thus provide internal pressure data for the structural design of typical industrial buildings.

The conclusions and recommendations derived from these full-scale studies are detailed as follows:

5.1. Conclusions

These full-scale studies produce several important outcomes as detailed below:

Nominally Sealed Building – JCU-ASIS

- Internal pressure fluctuations in the nominally sealed JCU-ASIS are small in comparison to external pressures. The magnitude of internal pressure fluctuations increases as the windward to leeward open area increases.
- The porosity of the nominally sealed JCU-ASIS walls was determined via air-leakage tests and equal to about 1% of the total wall area. This level of porosity is greater than buildings in temperate climates, and consistent with other previous air-leakage tests.
- The distribution and magnitude of the background leakage in the JCU-ASIS envelope is dependent on the wall fitments and construction tolerances. This knowledge is critical to assess the flow through the building and the resultant internal pressures.
- The quasi-static internal pressure approximation satisfactorily defines mean internal pressures by theoretical analysis of the spatially and temporally averaged external pressures on the windward and leeward surfaces and the windward to leeward open area ratio A_W/A_L. This requires accurate knowledge of the external pressure distribution, and the size and location of all openings in the envelope.
- The envelope flexibility/bulk modulus of the JCU-ASIS was determined by pressurizing the building. The influence of the flexibility on the internal pressure response is characterised by increasing the JCU-ASIS building volume by three times (i.e. $V = 4V_B$).

Single Large Opening – Sealed Full-Scale Test Enclosure:

- The internal pressure behaviour from a single large opening in an otherwise sealed building is influenced by the size and location of the opening, the building's effective volume, the external pressure fluctuations, and the characteristics of the flow through the opening.

- Damping of the flow through the opening is characterised by the non-dimensional opening area to building volume parameter S* = $\left(A^{3/2}/V\right)(a_s/\overline{U}_h)^2$. It is shown that as S* decreases, internal pressure fluctuations decrease due to an increase in damping. Conversely, as S* increases, internal pressure fluctuations increase due to a reduction in damping, where the tendency for Helmholtz resonance increases while damping is low.
- An increase in internal pressure energy occurs for S* from about 0.9 to 5.8 at the predicted Helmholtz frequency range from 2 to 3.5 Hz, for an inertial coefficient C_I between 1.2 and 1.5. This range of C_I values is within the range derived by other previous model-scale studies.
- Peak and standard deviation internal pressures equal external pressures applied to the opening for S* ≅ 0.9. The quasi-static approximation used in wind loading standards is satisfied for S* ≅ 0.9.
- Peak and standard deviation internal pressures are amplified for S* ≥ 1.9, and attenuated for S* ≤ 0.75, between 5 to 10%.
- As S* increases (from 0.9 to 5.8), additional energy loss occurs, characterised by the loss coefficient C_L increasing (from 10 to 20). The increase in C_L occurs due to increased viscous losses from a reduction in the absolute mean velocity through the opening. Other previous model-scale studies have identified a similar relationship ($C_L = f$(S*)).
- The increasing loss coefficient C_L damps Helmholtz resonance as S* increases.

Single large windward openings with background leakage – JCU-ASIS

- The background leakage in a typical industrial building with a large windward wall opening reduces the mean internal pressure relative to the pressure applied to the large opening and increases attenuation of internal pressure fluctuations.
- The area and distribution of background leakage in the envelope must be specified accurately to satisfactorily define the mean internal pressure and internal pressure fluctuations.
- Peak and standard deviation internal pressures are less than the external pressures applied to large windward wall openings, for windward to leeward open area ratio A_w/A_L up to 20, and at large S* values up to 390.

- The quasi-static approximation of the internal pressure response (i.e. peak internal pressure factor G_{pi} equals the peak external pressure factor $G_{pe,w}$), is conservative for the JCU-ASIS as background leakage significantly damps internal pressure fluctuations.
- Peak internal pressure factor G_{pi} is about 3 to 12% less than peak external pressure factor G_{pe} as S* decreases from 390 to 24.
- Model-scale studies that incorporate background leakage (small diameter holes) cannot correctly model the flow through the small openings due to low Re, producing unsatisfactory flow simulation and unrealistic results.

5.2. Recommendations

Based on the conclusions, the following recommendations and further research is suggested.

- The outcomes of this thesis present the measured peak internal pressure response relative to the quasi-static peak internal pressure approximation (used by wind loading standards) with respect to the non-dimensional opening area to building volume parameter S*. This information can be used to optimise the design internal pressures for similar industrial buildings given different wind speeds, area of the windward opening, and building dimensions.
- Accurate assessment of a building envelopes flexibility can be used to develop an accurate opening area to building volume parameter S*, subsequently used to optimise design internal pressures.
- Information on the magnitude and distribution of background leakage (gaps around fitments and construction tolerances) in industrial building envelopes is presented in Table 4.6. This information can be readily used to improve the calculation of windward to leeward open area ratios, and subsequent calculation of mean and peak internal pressures in steel-clad industrial buildings.
- Further assessment of the internal pressure response for a greater range of S* values and background leakage area is recommended to further characterise the internal pressure response for other building conditions.

- Combination of S*, C_L, and background leakage into a single parameter that characterises the peak internal pressure response could be used to define a correction factor to apply to the quasi-static internal pressure approximation, providing a simple method to optimise design internal pressures.

5.3. Concluding Statement

Characterisation of internal pressure fluctuations in buildings with a large windward wall opening is complex and sensitive to many parameters including the building volume, envelope flexibility, magnitude and distribution of background leakage, size and location of larger openings, and external pressure fluctuations.

The contribution of this thesis demonstrated that the internal pressure fluctuations in an industrial type building with a large windward wall opening are significantly damped by the magnitude of background leakage in the envelope. The quasi-static approach used to estimate design internal pressures is conservative in industrial buildings due to the large damping. Further, for buildings with negligible background leakage, Helmholtz resonance may occur when damping is low, and the quasi-static approach is satisfactory for a large windward opening when the opening area to building volume parameter S* is equal to about 0.9.

The results of this research should prove useful in the calculation of internal pressures in industrial type buildings and assist in further model-scale and analytical studies that examine internal pressures in industrial type buildings.

REFERENCES

ASCE Standard. (2011). Minimum Design Loads for Buildings and Other Structures. *American Society of Civil Engineers 7-10*. New York.

ASHRAE, H. (2005). Fundamentals, American Society of Heating Refrigeration and Air-Conditioning Engineers. Inc. Atlanta, GA.

ASTM, A. (2003). Standard E779-03: Standard Test Method for Determining Air Leakage Rate by Fan Pressurization. Paper presented at the American Society for Testing and Materials.

Bohra, L. K. (2004). *Flow and Pressure Drop of Highly Viscous Fluids in Small Aperture Orifices.* Retrieved from http://hdl.handle.net/1853/7269

Bond, W. N. (1920). The Effect of Viscosity on Orifice Flows. *Proceedings of the Physical Society of London, 33*(1), 225-230. doi:10.1088/1478-7814/33/1/322

Boughton, G., & Flack, D. (2008). *Shoalwater and Roleystone WA tornadoes Wind damage to buildings*. Retrieved from Cyclone Testing Station, School of Engineering, James Cook University, Queensland, 4811:

BS/EN13829. (2001). British Standard: Thermal performance of buildings - Determination of air permeability of buildings - Fan pressurization method.

Cermak, J. (1976). Aerodynamics of buildings. Annual Review of Fluid Mechanics, 8(1), 75-106.

Chaplin, G. C., Randall, J. R., & Baker, C. J. (2000). The turbulent ventilation of a single opening enclosure. *Journal of Wind Engineering and Industrial Aerodynamics, 85*(2), 145-161. doi:http://dx.doi.org/10.1016/S0167-6105(99)00136-1

Cook, N. J. (1986). *Designers guide to wind loading of building structures - Part 2: Static Structures*. Butterworths, London, UK.

Dagan, Z., Weinbaum, S., & Pfeffer, R. (1982). An infinite-series solution for the creeping motion through an orifice of finite length. *Journal of Fluid Mechanics, 115*, 505-523.

Davenport, A., & Surry, D. (1984). The *estimation of internal pressures due to wind with application to cladding pressures and infiltration.* Paper presented at the Proc., Wind pressure workshop.

Fahrtash, M., & Liu, H. (1990). Internal pressure of low-rise building—field measurements. *Journal of Wind Engineering and Industrial Aerodynamics, 36*, 1191-1200. doi:10.1016/0167-6105(90)90116-t

Ginger, J. D., Holmes, J. D., & Kim, P. Y. (2010). Variation of internal pressure with varying sizes of dominant openings and volumes. *Journal of Structural Engineering, 136*(10), 1319-1326. doi:10.1061/(ASCE)ST.1943-541X.0000225

Ginger, J. D., Holmes, J. D., & Kopp, G. A. (2008). Effect of building volume and opening size on fluctuating internal pressures. *Wind and Structures An International Journal, 11*(5), 361-376. doi:10.12989/was.2008.11.5.361

Ginger, J. D., Mehta, K. C., & Yeatts, B. B. (1997). Internal pressures in a low-rise full-scale building. *Journal of Wind Engineering and Industrial Aerodynamics, 72*(1-3), 163-174. doi:10.1016/S0167-6105(97)00241-9

Grose, R. (1983). Orifice flow at low Reynolds number. *Journal of pipelines, 3*(3), 207-214.

Guha, T. K., Sharma, R. N., & Richards, P. J. (2011a). Internal pressure dynamics of a leaky building with a dominant opening. *Journal of Wind Engineering and Industrial Aerodynamics, 99*(11), 1151-1161. doi:10.1016/j.jweia.2011.09.002

Guha, T. K., Sharma, R. N., & Richards, P. J. (2011b). Influence factors for wind induced internal pressure in a low rise building with a dominant opening. Journal of wind and Engineering, 8(02), 1-17.

Guha, T. K., Sharma, R. N., & Richards, P. J. (2013a). Field studies of wind induced internal pressure in a warehouse with a dominant opening. *Wind and Structures An International Journal, 16*(1), 117-136. doi:10.12989/was.2013.16.1.117

Guha, T. K., Sharma, R. N., & Richards, P. J. (2013b). Internal Pressure in a Building with a Single Dominant Opening: An Experimental and Numerical Case Study. *Journal of Structural Engineering (Madras), 41*(1), 243-252. doi:10.3850/978-981-07-8012-8_156

Happel, J. (1965). AIChEJ, 4 (1958) 197.| 4| 5| 6 J, Happel and H. Brenner, Low Reynolds Number Hydrodynamics: Prentice Hall, Englewood Cliffs, NJ.

Harris, R. I. (1990). The propagation of internal pressures in buildings. *Journal of Wind Engineering and Industrial Aerodynamics, 34*(2), 169-184. doi:10.1016/0167-6105(90)90142-Y

Hasegawa, T., Suganuma, M., & Watanabe, H. (1997). Anomaly of excess pressure drops of the flow through very small orifices. *Physics of Fluids, 9*(1), 1-3.

Heiselberg, P., Svidt, K., & Nielsen, P. V. (2001). Characteristics of airflow from open windows.

Henderson, D., Ginger, J., Leitch, C., Boughton, G., & Flack, D. (2006). Tropical Cyclone Larry Damage to buildings in the Innisfail area. Retrieved from Cyclone Testing Station, School of Engineering, James Cook University, Queensland, 4811

Henry. Liu. (1975). *Wind pressure inside buildings.* Paper presented at the Proceedings of the 2nd US National Conference on Wind Engineering Research, Colorado State University, June.

Holmes, J. D. (1979). *Mean and fluctuating internal pressures induced by wind.* Paper presented at the Fifth international conference on wind engineering, Fort Collins, Colorado, U.S.A.

Holmes, J. D. (2007). *Wind Loading of Structures*: Taylor & Francis.

Holmes, J. D., Allsop, A. C., & Ginger, J. D. (2014). Gust durations, gust factors and gust response factors in wind codes and standards. *Wind and Structures, 19*(3), 339-352. doi:10.12989/was.2014.19.3.339

Holmes, J. D., & Ginger, J. D. (2012). Internal pressures - The dominant windward opening case - A review. *Journal of Wind Engineering and Industrial Aerodynamics, 100*(1), 70-76. doi:10.1016/j.jweia.2011.11.005

Humphreys, M. T., Ginger, J. D., & Henderson, D. J. (2017). Internal Pressure Fluctuations in Large Open Plan Buildings. *Paper presented at the 9th Asia-Pacific Conference on Wind Engineering*, Auckland, New Zealand.

Humphreys, M. T., Ginger, J. D., & Henderson, D. J. (2019). Internal pressures in a full-scale test enclosure with windward wall openings. *Journal of Wind Engineering and Industrial Aerodynamics*, 189, 118-124. doi:https://doi.org/10.1016/j.jweia.2019.03.024

Idel'Chik, I. E. (1960). *Handbook of Hydraulic Resistance: Coefficients of Local Resistance and of Friction*. Berlin: Springer.

Irminger, J. O. V., & Nokkentved, C. (1936). Wind-pressure on buildings, experimental researches. *Ingeniorvidenskabelige Skrifter*.

Irwin, P. A., & Dunn, G. (1994). *Review of internal pressures on low rise buildings*. RWDI Report: 93-270.

Jensen, M., & Franck, N. (1963). *Model-scale tests in turbulent wind*: Danish Technical Press.

Johansen, F. (1930). Flow through pipe orifices at low Reynolds numbers. *Proceedings of the royal society of London. series A, containing Papers of a Mathematical and Physical character, 126*(801), 231-245.

Karava, P., Stathopoulos, T., & Athienitis, A. K. (2004). Wind Driven Flow through Openings – A Review of Discharge Coefficients. *International Journal of Ventilation, 3*(3), 255-266. doi:10.1080/14733315.2004.11683920

Kim, P. Y., & Ginger, J. D. (2013). Internal pressures in buildings with a dominant opening and background porosity. *Wind and Structures An International Journal, 16*(1), 47-60. doi:10.12989/was.2013.16.1.047

Kusmanto, F., Jacobsen, E. L., & Finlayson, B. A. (2004). Applicability of continuum mechanics to pressure drop in small orifices. *Physics of Fluids, 16*(11), 4129-4134. doi:10.1063/1.1800051

Kwok, K. C., & Hitchcock, P. A. (2009). Characterisation of and wind-induced pressures in a compartmentalised building during a typhoon. *Journal of wind and Engineering, 6*(2), 30-41.

Levitan, M. L., & Mehta, K. C. (1992). Texas Tech field experiments for wind loads part 1: building and pressure measuring system. *Journal of Wind Engineering and Industrial Aerodynamics, 43*(1-3), 1565-1576. doi:10.1016/0167-6105(92)90372-h

Liu, H., & Rhee, K. H. (1986). Helmholtz oscillation in building models. *Journal of Wind Engineering and Industrial Aerodynamics, 24*(2), 95-115. doi:10.1016/0167-6105(86)90001-2

Liu, H., & Saathoff, P. J. (1981). Building Internal Pressure: Sudden Change. *Journal of the Engineering Mechanics Division, 107*(2), 309-321.

Michell, D., & Biggs, K. L. (1982). *An Apparatus for air-tightness measurements on houses*. Revision of Building Research: BUILDING RESEARCH Melbourne.

Morrison, M. J., Kopp, G. A., Gavanski, E., Miller, C., & Ashton, A. (2014). Assessment of damage to residential construction from the tornadoes in Vaughan, Ontario, on 20 August 2009. *Canadian Journal of Civil Engineering, 41*(6), 550-558. doi:10.1139/cjce-2013-0570

Morrison, M. J., & Reinhold, T. A. (2015). Performance of Metal Roofing to Realistic Wind Loads and Evaluation of Current Test Standards. Paper presented at the 14th International Conference on Wind Engineering, Porto Alegre, Brazil, June 21-26

Oh, J. H. (2004). *Wind-Induced Internal Pressures In Low-Rise Buildings.* (Master of Engineering Science), University of Western Ontario.

Oh, J. H., Kopp, G. A., & Inculet, D. R. (2007). The UWO contribution to the NIST aerodynamic database for wind loads on low buildings: Part 3. Internal pressures. *Journal of Wind Engineering and Industrial Aerodynamics, 95*(8), 755-779. doi:10.1016/j.jweia.2007.01.007

Pearce, W., & Sykes, D. M. (1999). Wind tunnel measurements of cavity pressure dynamics in a low-rise flexible roofed building. *Journal of Wind Engineering and Industrial Aerodynamics*, 82(1-3), 27-48.

Shanmugasundaram, J., Arunachalam, S., Gomathinayagam, S., Lakshmanan, N., & Harikrishna, P. (2000). Cyclone damage to buildings and structures — a case study.

Journal of Wind Engineering and Industrial Aerodynamics, 84(3), 369-380. doi:10.1016/S0167-6105(99)00114-2

Sharma, R. N. (1996). *The influence of internal pressure on wind loading under tropical cyclone conditions.* University of Auckland.

Sharma, R. N. (2013). *The Fundamentals of Building Internal Pressure Dynamics Induced Through a Dominant Opening.* Paper presented at The Eighth Asia-Pacific Conference on Wind Engineering, Chennai India. December 10–14

Sharma, R. N., & Richards, P. J. (1997). Computational modelling in the prediction of building internal pressure gain functions. *Journal of Wind Engineering and Industrial Aerodynamics, 67–68*, 815-825. doi:http://dx.doi.org/10.1016/S0167-6105(97)00121-9

Sharma, R. N., & Richards, P. J. (2003). The influence of Helmholtz resonance on internal pressures in a low-rise building. *Journal of Wind Engineering and Industrial Aerodynamics, 91*(6), 807-828. doi:http://dx.doi.org/10.1016/S0167-6105(03)00005-9

Shaw, C. Y. (1981). Air Tightness: Supermarkets and Shopping Malls. *ASHRAE, 23*(3), 44-46.

Shaw, C. Y., & Jones, L. (1979). Air tightness and air infiltration of school buildings. ASHRAE Transactions, 85(1), 85 - 95.

British Standards (2001). BS EN 13829:2001 Thermal performance of buildings - Determination of air permeability of buildings - Fan pressurization method.

Standards Australia, & Standards New Zealand. (2011). AS/NZS 1170.2:2011 (A5) *Australian and New Zealand Standard – Structural Design Part 2: Wind Actions*.

Stathopoulos, T., & Luchian, H. D. (1989). Transient Wind-Induced Internal Pressures. *Journal of Engineering Mechanics, 115*(7), 1501-1514. doi:10.1061/(asce)0733-9399(1989)115:7(1501)

Stathopoulos, T., Surry, D., & Davenport, A. G. (1979). *Internal pressure characteristics of low-rise buildings due to wind action*. Paper presented at the 5th International Conference on Wind Engineering, Fort Collins, Colorado USA.

Stehle, J., & Henderson, D. (2001). *Field damage survey of the Dubbo NSW windstorm of the 6th January 2001.* Paper presented at the 9th Australian Wind Engineering Workshop.

Tamura, G. T., & Shaw, C. Y. (1976). Studies on exterior wall air tightness and air infiltration of tall buildings. *ASHRAE Trans. (United States), 82*.

Urquhart, R., & Richman, R. (2015). The relationship between flow exponents and flow values and associated implications for air leakage testing using fan (de) pressurization methodology. *14th Canadian conference on building science and technology*

Vickery, B. J. (1986). Gust-Factors for Internal-Pressures in Low Rise Buildings. *Journal of Wind Engineering and Industrial Aerodynamics, 23*(1-3), 259-271. doi:10.1016/0167-6105(86)90047-4

Vickery, B. J. (1991). Comments on "the propagation of internal pressures in buildings" by R.I. Harris. *Journal of Wind Engineering and Industrial Aerodynamics, 37*(2), 209-212. doi:http://dx.doi.org/10.1016/0167-6105(91)90074-7

Vickery, B. J., & Bloxham, C. (1992). Internal pressure dynamics with a dominant opening. *Journal of Wind Engineering and Industrial Aerodynamics, 41*(1–3), 193-204. doi:10.1016/0167-6105(92)90409-4

Vickery, B. J., & Karakatsanis, C. (1987). External Wind Pressure Distributions And Induced Internal Ventilation Flow In Low-Rise Industrial And Domestic Structures. *ASHRAE Transactions*(93), 2198-2213.

W., P., & M., S. D. (1999). Wind tunnel measurements of cavity pressure dynamics in a low-rise flexible roofer building. *Journal of Wind Engineering & Industrial Aerodynamics, 82*, 27-48.

White, F. M. (2003). *Fluid Mechanics* (5th ed.): McGraw-Hill USA.

Womble, J., Yeatts, B., Cermak, J., & Mehta, K. (1995). *Internal wind pressures in a full and small-scale building.* Paper presented at the Proc., 9th Int. Conf. on Wind Engineering.

Woods, A. R., & Blackmore, P. A. (1995). The effect of dominant openings and porosity on internal pressures. *Journal of Wind Engineering and Industrial Aerodynamics, 57*(2–3), 167-177. doi:10.1016/0167-6105(95)00003-A

Xu, H., Yu, S., & Lou, W. (2014). The inertial coefficient for fluctuating flow through a dominant opening in a building. *Wind and Structures, an International Journal, 18*(1), 57-67. doi:10.12989/was.2014.18.1.057

Xu, H., Yu, S., & Lou, W. (2017). The loss coefficient for fluctuating flow through a dominant opening in a building. *Wind and Structures, 24*(1), 79-93. doi:10.12989/was.2017.24.1.079

Yang, Q., Gao, R., Bai, F., Li, T., & Tamura, Y. (2018). Damage to buildings and structures due to recent devastating wind hazards in East Asia. *Natural Hazards*. doi:10.1007/s11069-018-3253-8

Yeatts, B. B. (1994). *Internal Pressure For Buildings.* (Master of Science), Texas Tech University.

Yu, S.-c., Lou, W.-j., & Sun, B.-n. (2006). Wind-induced internal pressure fluctuations of structure with single windward opening. *Journal of Zhejiang University SCIENCE A, 7*(3), 415-423. doi:10.1631/jzus.2006.A0415

Yu, S.-c., Lou, W.-j., & Sun, B.-n. (2008). Wind-induced internal pressure response for structure with single windward opening and background leakage. *Journal of Zhejiang University-SCIENCE A, 9*(3), 313-321. doi:10.1631/jzus.A071271

APPENDIX A: NUMERICAL METHODS

The second-order, non-linear, differential Equation 2.9 requires the solution of first and second order internal pressure terms. These terms can be approximated with finite difference methods. The backwards finite difference method was utilized to approximate the first and second order terms, shown in Equations A.1 and A.2, respectively. Where *j* is the current time step and Δt is the time step between measurements.

$$\dot{C}_{pi}(j) = \frac{C_{pi}(j) - C_{pi}(j-1)}{\Delta t} \tag{A.1}$$

$$\ddot{C}_{pi}(j) = \frac{C_{pi}(j) - 2C_{pi}(j-1) + C_{pi}(j-2)}{(\Delta t)^2} \tag{A.1}$$

APPENDIX B: EXPERIMENTAL TESTING EQUIPMENT

This appendix details the equipment used during the full-scale experiments. This includes the data acquisition systems, pressure transducers, displacement transducers, and anemometers.

B.1. Data Acquisition System

National Instruments compact Data Acquisition (DAQ) system, NI-cDAQ-9178, was used along with three 32-channel, 0 to 10 Volt analogy input modules, NI-9205 with an accuracy of ±0.4 mV, and one 32-channel digital output module, NI-9476, where utilized for the experiments. A custom designed LabVIEW program was built to record the pressure transducers, displacement transducers, and anemometers signals received and output digital voltage signal to actuate the solenoid valves when required. The analogy input and digital output modules are shown in Figure B.1. Figure B.2 shows a portion of the front panel of the LabVIEW program, DAQ system, and power supplies during the JCU-ASIS experimental setup.

Figure B.1. Data acquisition system NI-cDAQ 9178 and input/output modules

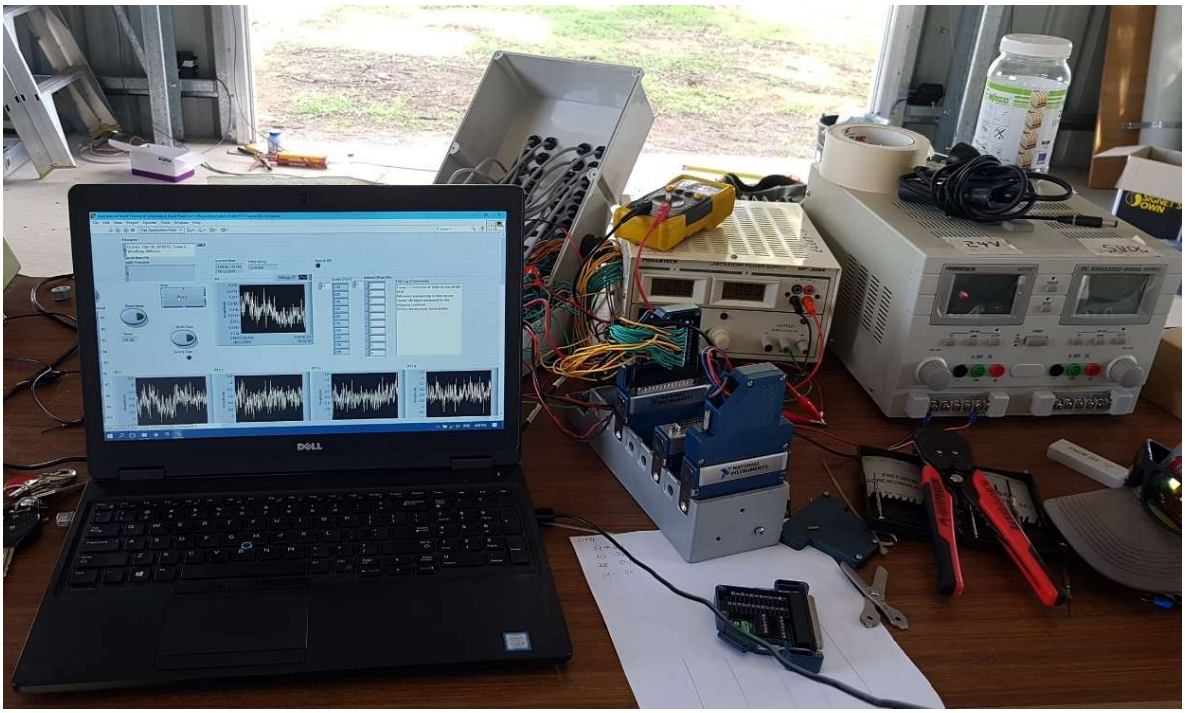

Figure B.2. LabVIEW program, NI-cDAQ, and power supplies during the JCU-ASIS experimental setup

B.2 Pressure Transducers

Honeywell TruStability® board mount differential pressure transducers were used to measure the wind-induced pressures for the FSTE and JCU-ASIS. A transducer is shown in Figure B.3, Figure B.4 shows a transducer in the protective housing attached to the solenoid valve and tubing, and Figure B.5 shows a transducer in situ connected to Tap T7. The Honeywell TruStability® transducer product code is HSCSNB002NDAA5. The transducers are temperature compensated with an analogy output signal from 0 to 5 Volts. The pressure range is ± 500 Pa with a total error band of ±0.25 % (≈ 1 Pa). A Turbulent Flow Instrumentation – Dynamic Pressure Measurement System was used to calibrate the transducers, accounting for the tubing, solenoid valve, and wiring response.

Figure B.3. Honeywell TruStability® pressure transducer

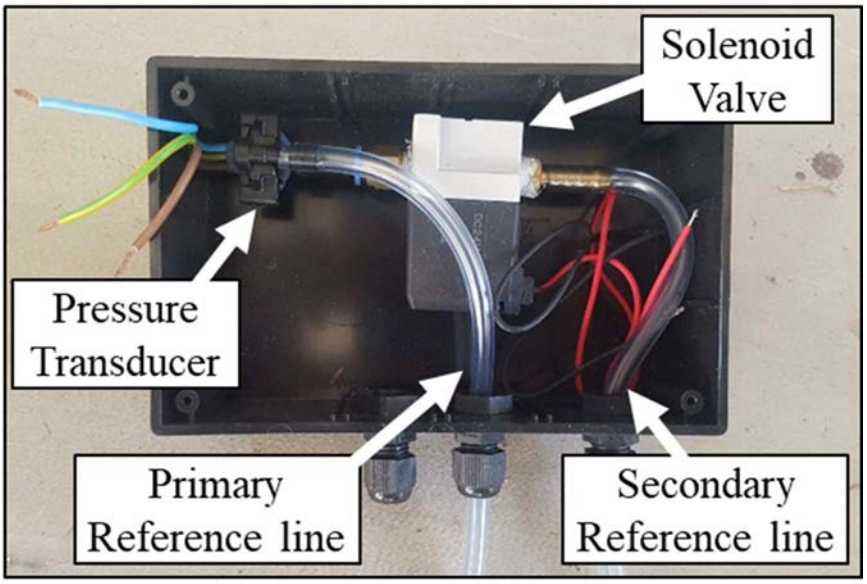

Figure B.4. Pressure transducer and Solenoid valve in housing

Figure B.5. Pressure transducer in situ connected tap T7 on the JCU-ASIS

All pressure transducers were referenced to atmospheric pressure from reference pressure pits, shown in Figures B.6 and B.7 for the FSTE and JCU-ASIS respectively, and supplied to each transducer via 4 mm vinyl tubing. The active pressure port passes through a solenoid valve prior to connection to a pressure tap. Each solenoid is actuated prior to each 10 minute run, applying atmospheric pressure to the active pressure port, zeroing the transducers. Direct operated poppet type 3-port SMC series VT307 solenoid valves (part number VT307K-5DZ1-01) were connected to each pressure transduce.

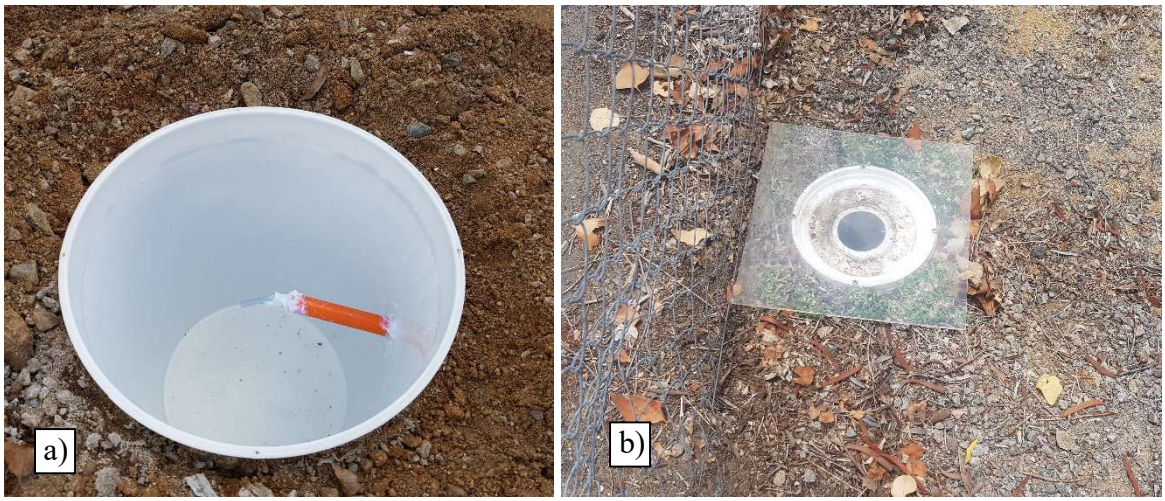

Figure B.6. FSTE reference pressure pit (a) Installation of underground tubing/conduit into pit (b) Pit in situ with flat Perspex lid

Figure B.7. JCU-ASIS reference pressure pit (a) Installation of underground tubing/conduit into pit (b) Pit in situ with flat lid flush with ground

B.3. Anemometers

The FSTE experiments used a marine rated R.M. Young propeller anemometer, Model 05106, mounted on tripod at a measurement height of 3 m, shown in Figure B.8 during the experimental setup. The anemometer is sampled and logged at 10 Hz to a memory card, powered by an on-board battery, the time history was later post processed to a 3 second moving average signal. The anemometer sends 3 pulses per propeller revolution, with a range of 0 to 100 m/s and an accuracy of ±0.3 m/s or 1% of the reading. Synchronisation of the anemometer and pressure measurements was conducted by synchronising the on-board time of the anemometer data logger and PC running the LabVIEW code.

Figure B.8. FSTE during setup, (foreground) R.M. Young Anemometer 5 m from the FSTE, (background) Timber wall installed in FSTE.

An ultrasonic R.M. Young anemometer (Model 81005A) was used for the JCU-ASIS experiment, detailed in Section 4.2.5. The anemometer has a minimum wind speed threshold of 0.2 m/s and was configured to output the wind speed, angle, pitch, and sonic temperature (-50 to +50 °C) as four analogy signals ranging from 0 to 5 Volt. The wind speed measurement range is 0 to 40 m/s with an accuracy of ±0.05 m/s (for 0 to 30 m/s) and ±1.5 m/s (for 30 to 40 m/s). The signals were recorded at 20 Hz by the NI cDAQ and later post processed to 5 Hz with a moving average filter.

B.4. Displacement Transducers

Vishay® 130 mm 5 kOhm Linear Variable Displacement Transducers (LVDTs) measured the deflection of the JCU-ASIS envelope during the pressurization testing detailed in Section 4.3. The accuracy of the LVDT measurements is ±0.01 mm and were recorded at 120 Hz. Table B.1 provides details on the precise location of each LVDT on the JCU-ASIS shown in Figure B.9.

Table B.1. LVDT Location Details

LVDT #	Measurement Position:
1	Northern Wall Cladding: Centred between the Eastern and middle portal frames, 450 mm above wall cladding to girt fasteners above window, (i.e. centre of the 900 mm cladding to girt fastener spacing), positioned at the centre of cladding pan (rib and pan profile).
2	Northern Wall Cladding: Centred between the Eastern and middle portal frames, 100 mm above wall cladding and girt fasteners above Window, positioned at the centre of cladding pan profile, (below LVDT #1).
3	Northern Wall Girt: Centred between the Eastern and middle portal frames, positioned on girt above window, 2080 mm from floor slab.
4	Northern Wall Cladding: Cladding beside centre portal frame, 2555 mm from floor slab, centred between 950 mm girt spacing (i.e. girts 1130 mm and 2080 mm from floor slab, below and above window frames), positioned at the centre of cladding pan profile.
5	Northern Wall Column: Centre portal frame column, 1500 mm from the floor slab (i.e. centre of 3 m tall column).
6	Roof Purlin: Centred between the Eastern and middle portal frames, second internal purlin in from Northern eave strut. Positioned on the bottom flange perpendicular to the roof slope.
7	Roof Cladding: Centred between the Eastern and middle portal frames, Centred between second and third internal purlin in from Northern eave strut. Positioned on the centre of the cladding pan, perpendicular to the roof slope.
8	Central portal frame ridge gusset plate: Central portal frame, positioned vertically under the ridge gusset plate flange.
9	Western Roller Door: 120 mm from edge of roller door track, positioned 1.2 m vertically from floor slab.
10	Western Roller Door: Centre of 2760 mm span, positioned 1.2 m vertically from the floor slab.

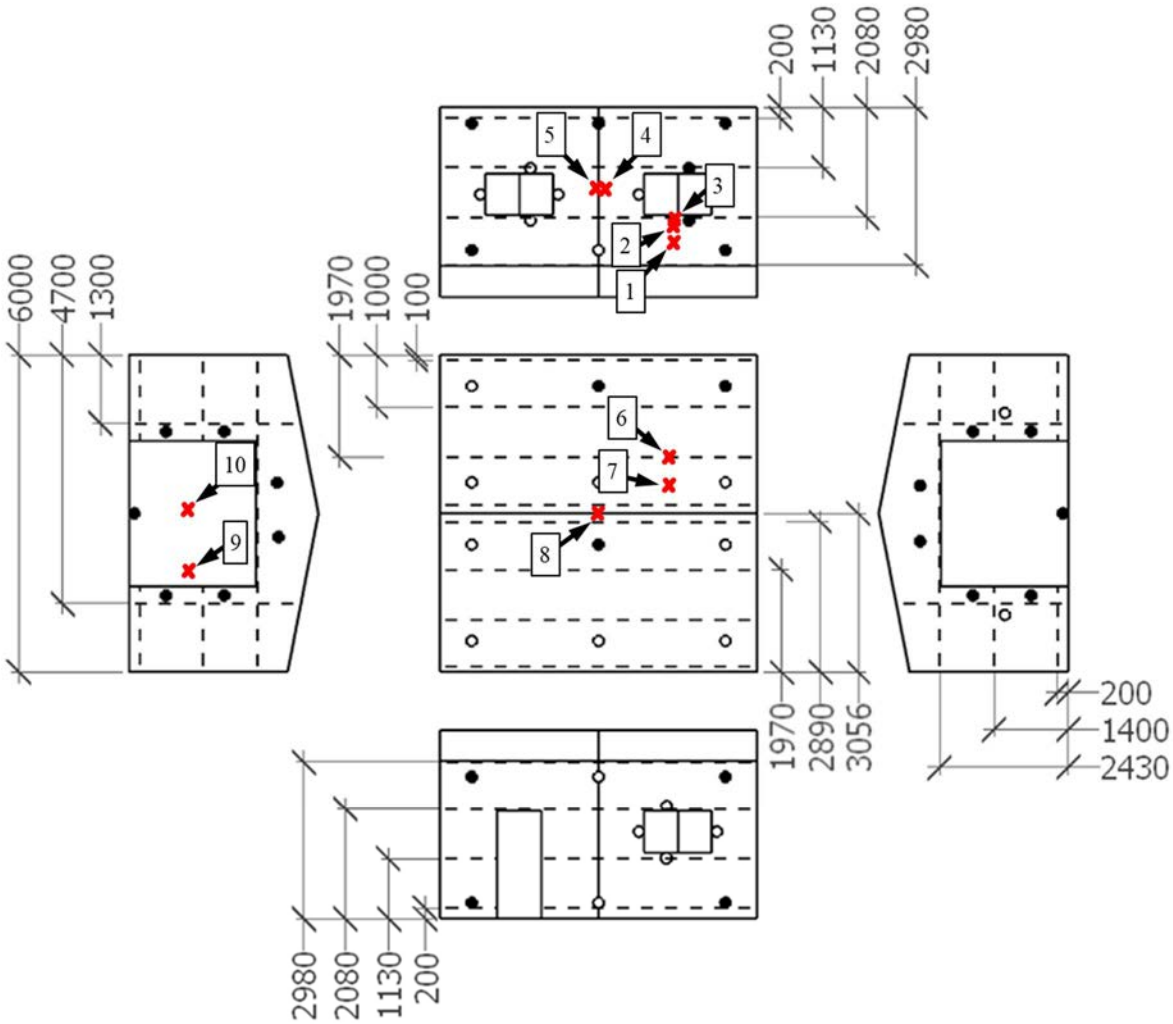

Figure B.9. Schematic of LVDT locations – Dashed lines are purlins, girts, and mullions (all dimensions in mm)

APPENDIX C: JCU-ASIS – CONSTRUCTION DETAILS

The JCU-AIS Shed is a cold-form, steel-clad, industrial building with three portal-fames, spaced 3 m apart, roof and wall cladding is fixed to roof purlins and wall girts, the purlins and girts span across rafters and columns, which form portal frames. A schematic of the structural members is shown in Figure C.1, and listed in Table C.1.

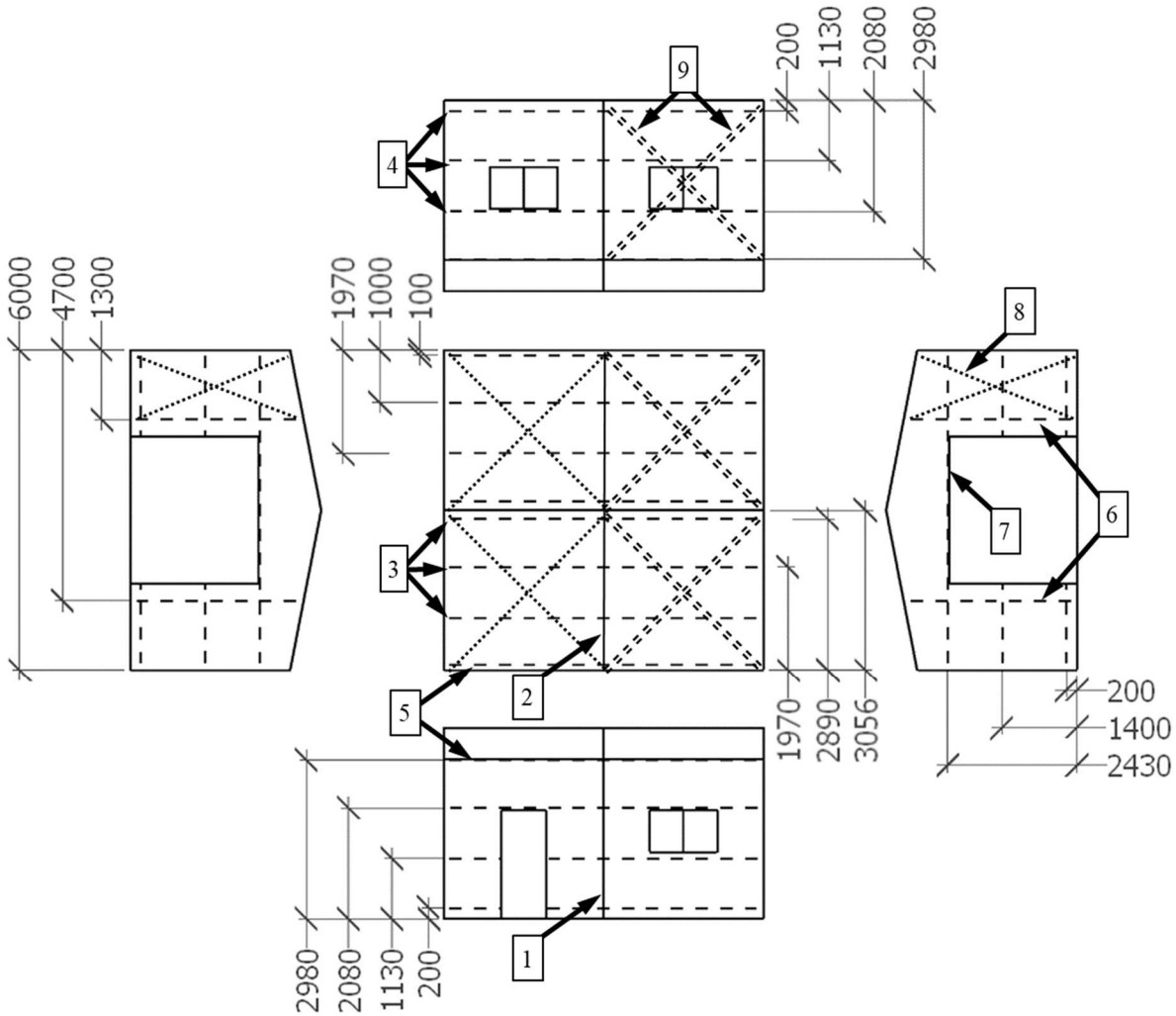

Figure C.1. Schematic of JCU-ASIS structural members

Table C.1 JCU-ASIS Member Details

No.	Structural Member	Section
1	Columns	C15019 (152 mm deep × 1.9 BMT)
2	Rafters	C15019 (152 mm deep × 1.9 BMT)
3	Purlins	Z10015 (102 mm deep × 1.5 BMT)
4	Girts	Z10015 (102 mm deep × 1.5 BMT)
5	Eave Struts	C15015 (152 mm deep × 1.9 BMT)
6	Mullions	C20015 (203 mm deep × 1.9 BMT)
7	Roller Door Header Beam	C15015 (152 mm deep × 1.9 BMT)
8	Bracing	Structural bracing strap
9	Bracing	12 mm threaded rod
10	Cladding	0.42 BMT Trimdek® Cyclone assembly on roof, non-Cyclone assembly on walls

The JCU-ASIS consists of a 150 mm thick slab with edge thickening. The columns are fastened to cast in steel cleats in the edge of the slab, shown in Figure C.2. The mullions are fastened to brackets mechanically fixed into the slab. Figures C.2 and C.3 show the 90 mm deep by 35 mm wide rebate set into the perimeter of the slab to cap the ends of the wall sheeting to prevent vermin entering beneath the walls.

The column-to-rafter (knee) connections and rafter-to-rafter (ridge) connection are bolted gusset plates shown in Figures C.4 and C.5 respectively. Further, the unrestrained flanges of the first

internal columns are braced to the 2.08 m high wall girts and the first internal rafters are braced on the first and second internal roof purlins.

Figure C.2. Edge of concrete slab prior to framing erection

Figure C.3. JCU-ASIS wall cladding adjacent to slab rebate

Figure C.4. Bolted gusset plate – Knee connection

Figure C.5. Bolted gusset plate – Ridge connection

The windows and Personnel Access (PA) door require trimmer members on either side of the wall fitments spanning between wall girts (and floor). The header beam above the roller door spans between C15015 Cee sections either side of the roller door that span from the floor to rafters. These vertical members are supported by the wall girts which are further supported by the mullions adjacent to the roller doors.

Rain dividers are above each wall fitment (i.e. PA door, windows, and roller doors). The PA door rain divider is shown in Figure C.6. At the base of the windows, skirting over hangs the wall cladding ribs and pans to divert water away from the building. Figures C.7 and C.8 show the skirting from the outside and from the inside of the building.

Figure C.6 Rain divider above PA door

Figure C.7 Rubber skirt at the bottom of window

Figure C.8. Construction gap under windows covered by external rubber skirting

APPENDIX D: DERIVATION OF FLOW EXPONENTS AND FLOW COEFFICIENTS

The relationship between flow rate into a building and the induced pressure can be described by the power law, $\bar{Q} = C(\Delta\bar{p})^n$, detailed in Section 2.3.1 and 4.3. The recommended procedure to estimate the flow-exponent n and flow coefficient C from the measured $\bar{Q}$ and $\Delta\bar{p}$ readings is detailed in the British Standard for the testing of the air permeability of buildings (BN/EN 13829:2001) from an unweighted log-linearized linear regression technique, detailed below.

A logarithmic transformation of the pressure and flow rate measurements is required. Where the flow-rate and pressure readings, $\bar{Q}_i$ and $\Delta\bar{p}_i$ respectively, are transformed into x_i and y_i below and the power law ($\bar{Q} = C(\Delta\bar{p})^n$) is transformed into Equation D.1. Here i is the reading number and N is the total number of readings, for i = 1 to N.

$$x_i = \ln(\Delta\bar{p}_i)$$

$$y_i = \ln(\bar{Q}_i)$$

$$y = \ln(C) + nx \qquad \text{D.1}$$

Compute the following quantities:

$$\bar{x} = \frac{1}{N}\sum_{i=1}^{N} x_i \qquad \text{D.2}$$

$$\bar{y} = \frac{1}{N}\sum_{i=1}^{N} y_i \qquad \text{D.3}$$

$$s_x^2 = \frac{1}{N-1}\sum_{i=1}^{N} (x_i - \bar{x})^2 \qquad \text{D.4}$$

$$s_{xy} = \frac{1}{N-1}\sum_{i=1}^{N}(x_i - \bar{x})(y_i - \bar{y}) \quad \text{D.5}$$

The best estimate of *n*, *ln(C)* and *C* are given in Equations D.6 to D.8.

$$n = \frac{s_{xy}}{s_x^2} \quad \text{D.6}$$

$$ln(C) = \bar{y} - n\bar{x} \quad \text{D.7}$$

$$C = exp^{(\bar{y} - n\bar{x})} \quad \text{D.8}$$

APPENDIX E: JCU-ASIS EXTERNAL PRESSURE VARIATION ADJACENT TO WALL FITMENTS

Appendix E details an assessment of the external pressures around the Eastern roller door to assess the influence of the open wall fitments on the external pressures around the perimeter of the opening.

Figures E.1 to E.3 show the mean pressure ($\bar{p}$), standard deviation pressure (σ_p), and Coefficient of Variance $(\sigma_p/\bar{p})$ from the pressure taps around the perimeter of the Eastern Roller Door for Cases NS2, #2, #3, #4, and #5 for $\theta \cong 0°$. Pressure tap T1 is attached to the base of the roller door, thus the height of the tap location is relative to the roller door position, for Case #5 (i.e. roller door fully open), pressure tap T1 is behind the wall cladding, and measures internal pressures. Also, pressure tap T2 was blocked and failed to collect data for Case #5.

Figures E.1 and E.2 shows that there are variations in the mean pressure and magnitude of pressure fluctuations at the tap locations between the large opening positions (i.e. Case NS2: Closed roller-door to Case #5: 100% open roller-door). These variations are due to a combination of the different approach wind speeds, wind angles ($\bar{\theta} \pm 30°$) and the variation of the percentage of open roller door influencing the flow in and around the openings.

Figure E.3 shows the relative variance of the pressure fluctuations $(\sigma_p/\bar{p})$ at Tap T2 increases relative to the Nominally Sealed building (Case NS2) as the large opening area increases. In addition, the relative variance of pressure fluctuations at tap T3 (1.8 m from concrete slab) for Cases #2 to #4 (roller door open from 0.3 m to 1.2 m (12.5% to 50%)), is constant at 70%. However, once the roller-door is open 2.4 m (Case #5), the tap is adjacent to the opening and variance increases to 80%, suggests that the flow in and out of the openings is influencing the external pressures at tap T3. It is also proposed this is more evident on the Southern side of the Eastern roller-door due to greater population of the data is for mean wind angles $\theta < 90°$, and has marginally greater wind speeds from $\theta < 90°$, where taps on the Southern side of the Eastern wall would be slightly downstream of the roller door for $\theta < 90°$.

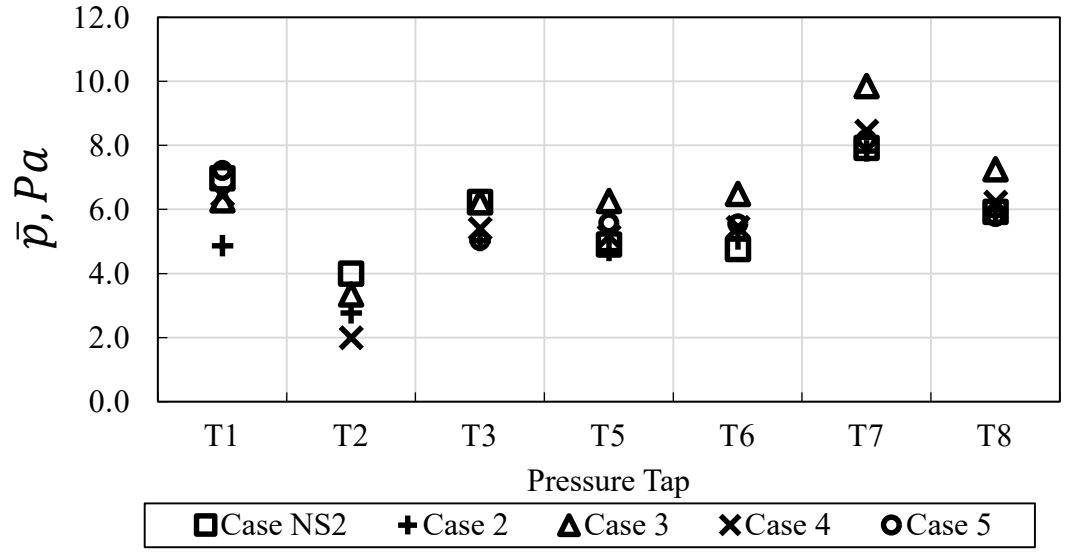

Figure E.1. Mean pressures at pressure taps on the Eastern wall for large opening Cases for θ ≅ 90°

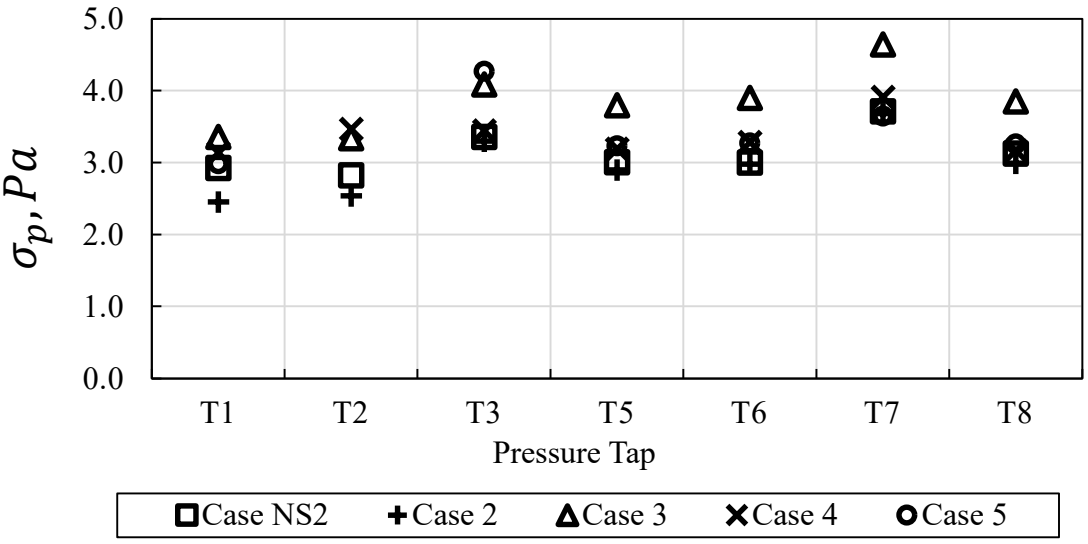

Figure E.2. Standard deviation pressures at pressure taps on the Eastern wall for large opening Cases for θ ≅ 90°

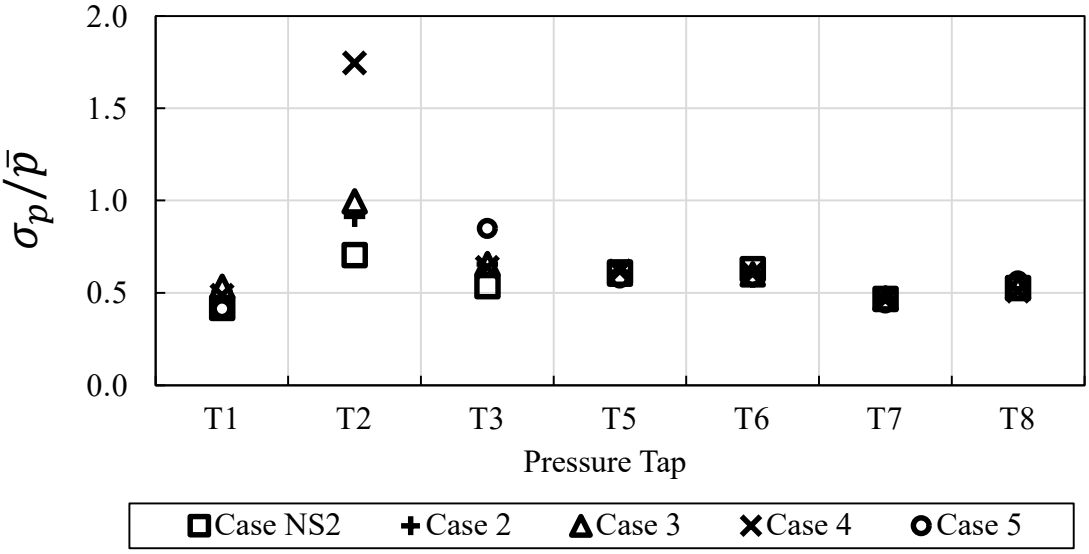

Figure E.3. Coefficient of Variance at pressure taps on the Eastern wall for large opening Cases for θ ≅ 90°